ISSN 1997-308X
eISSN 2412-8767

ИЗВЕСТИЯ ВУЗОВ
ПОРОШКОВАЯ МЕТАЛЛУРГИЯ И ФУНКЦИОНАЛЬНЫЕ ПОКРЫТИЯ

POWDER METALLURGY AND FUNCTIONAL COATINGS

2025
Том 19 № 1
Vol. 19 No. 1
powder.misis.ru

ISSN 1997-308X
eISSN 2412-8767

POWDER METALLURGY AND FUNCTIONAL COATINGS

Scientific and Technical Journal
Founded in 2007
Six issues per year

2025
Том Vol. 19 № No. 1

ИЗВЕСТИЯ ВУЗОВ ПОРОШКОВАЯ МЕТАЛЛУРГИЯ И ФУНКЦИОНАЛЬНЫЕ ПОКРЫТИЯ

Научно-технический журнал
Основан в 2007 г.
Выходит 6 раз в год

POWDER METALLURGY AND FUNCTIONAL COATINGS

ISSN 1997-308X
eISSN 2412-8767

Scientific and Technical Journal
Founded in 2007
Six issues per year

http://powder.misis.ru

Founder: MISIS University of Science and Technology

National University of Science and Technology "MISIS"
Address: 1 Bld, 4 Leninskiy Prosp., Moscow 119049, Russian Federation
http://www.misis.ru

Journal is included into the List of peer-reviewed scientific publications recommended by the Highest Attestation Commission of the Ministry of Education and Science of the Russian Federation for publishing the results of doctoral and candidate dissertations.
Abstracting/Indexing: Scopus, Russian Science Citation Index (RSCI), Ulrich's Periodicals Directory, VINITI Database (Abstract Journal).

Certificate of registration **No. FS77-27955** (12.04.2007)
Re-registration **PI No. FS77-79230** (25.09.2020)

Signed print 21.02.2025. Format 60×90 1/8
Offset paper No. 1. Digital printing. Quires 9.25
Order 21563. Free price
Printed in the printing house of the MISIS Publish House
1 Bld, 4 Leninskiy Prosp., Moscow 119049, Russian Federation
Phone/fax: +7 (499) 236-76-17

ИЗВЕСТИЯ ВУЗОВ
ПОРОШКОВАЯ МЕТАЛЛУРГИЯ
И ФУНКЦИОНАЛЬНЫЕ ПОКРЫТИЯ

НАУЧНО-ТЕХНИЧЕСКИЙ ЖУРНАЛ
ОСНОВАН В 2007 Г.
ВЫХОДИТ 6 РАЗ В ГОД

http://powder.misis.ru

ISSN 1997-308X
eISSN 2412-8767

Учредитель:

ФГАОУ ВО Национальный исследовательский технологический университет «МИСИС»
Адрес: 119049, Москва, Ленинский пр-т, 4, стр. 1
https://www.misis.ru

Журнал включен в Перечень рецензируемых научных изданий, рекомендованных ВАК Минобрнауки РФ для публикации результатов диссертаций на соискание ученых степеней.
Журнал включен в базы данных: Scopus, Russian Science Citation Index (RSCI), Ulrich's Periodicals Directory, РИНЦ, БД/РЖ ВИНИТИ.

Редакция журнала

Адрес: 119049, Москва,
Ленинский пр-т, 4, стр. 1. НИТУ МИСИС

Тел.: +7 (495) 638-45-35. ***Эл. почта:*** izv.vuz@misis.ru

Свидетельство о регистрации № **ФС77-27955** от 12.04.2007 г.
Перерегистрация 25.09.2020 г. **ПИ № ФС77-79230**

Ведущий редактор: А.А. Кудинова
Выпускающий редактор: О.В. Соснина
Дизайн и верстка: В.В. Расенець

Подписано в печать 21.02.2025. Формат 60×90 1/8
Бум. офсетная № 1. Печать цифровая. Усл. печ. л. 9,25
Заказ 21563. Цена свободная
Отпечатано в типографии Издательского Дома МИСИС
119049, г. Москва, Ленинский пр-т, 4, стр. 1
Тел./факс: +7 (499) 236-76-17

Contents

Содержание

Production Processes and Properties of Powders
Процессы получения и свойства порошков

UDC 004.942
https://doi.org/10.17073/1997-308X-2025-1-5-14

Research article
Научная статья

Influence of gear ratio on the energy-force conditions of grinding body collisions in a planetary mill

A. V. Aborkin[1], A. I. Elkin[1], V. V. Ryabkova[1],

A. P. Bugayov[1], A. R. Bobozhanov[2], M. I. Alymov[2]

[1] Vladimir State University named after Alexander and Nikolay Stoletovs
87 Gorky Str., Vladimir 600000, Russia
[2] Merzhanov Institute of Structural Macrokinetics and Materials Science of the Russian Academy of Sciences
8 Akademika Osip'yan Str., Chernogolovka, Moscow Region 142432, Russia

aborkin@vlsu.ru

Abstract. High-energy milling in planetary mills has found widespread application for tasks such as mechanical alloying/activation, synthesis of composite powder mixtures, and recycling of chip waste. The transfer of mechanical energy to the processed material depends, among other factors, on the technological parameters of mechanical processing, which determine the motion of the grinding bodies and, consequently, the energy-force characteristics of the process. To study the effect of the gear ratio on the energy-force conditions of mechanical processing, a discrete element model of grinding body motion in a planetary mill was developed, numerically implemented, and validated. Model parameters were determined to ensure reasonable agreement between the experimental and calculated structures of instantaneous images of grinding body motion in the steady-state operation of the mill. Using the model, a series of numerical experiments were conducted, varying the gear ratio K from 1 to 2. It was shown that increasing K within this range changes the motion pattern of the grinding bodies from a rolling mode to a combination of rolling and free flight. This transition reduces the number of collisions while simultaneously increasing their force characteristics. An analysis of the changes in total energy loss during "body–body" and "body–chamber" collisions was performed. It was established that as K increases from 1 to 2, the total energy loss during collisions primarily increases due to greater energy loss in "body–body" collision pairs. The developed models and the obtained numerical estimates of the effect of the gear ratio on the energy-force characteristics of collisions can be utilized to design optimized mechanical processing technology in planetary mills.

Keywords: high-energy milling, discrete element method, energy-force characteristics, collisions, motion pattern of grinding bodies

Acknowledgements: The authors express their gratitude to Prof. A.S. Rogachev for his assistance in organizing and conducting the experimental study. This research was supported by the Russian Science Foundation (grant no. 23-29-00889, https://rscf.ru/project/23-29-00889/).

For citation: Aborkin A.V., Elkin A.I., Ryabkova V.V., Bugayov A.P., Bobozhanov A.R., Alymov M.I. Influence of gear ratio on the energy-force conditions of grinding body collisions in a planetary mill. *Powder Metallurgy and Functional Coatings*. 2025;19(1): 5–14. https://doi.org/10.17073/1997-308X-2025-1-5-14

Влияние передаточного отношения на энергосиловые условия столкновения размольных тел в планетарной мельнице

А. В. Аборкин[1], А. И. Елкин[1], В. В. Рябкова[1], А. П. Бугаёв[1], А. Р. Бобожанов[2], М. И. Алымов[2]

[1] **Владимирский государственный университет им. А.Г. и Н.Г. Столетовых**
Россия, 600000, г. Владимир, ул. Горького, 87
[2] **Институт структурной макрокинетики и проблем материаловедения им. А.Г. Мержанова РАН**
Россия, 142432, Московская обл., г. Черноголовка, ул. Академика Осипьяна, 8

aborkin@vlsu.ru

Аннотация. Высокоэнергетическая обработка в планетарных мельницах нашла широкое применение для решения задач механического легирования/активации, синтеза композиционных порошковых смесей и переработки стружечных отходов. При этом передача механической энергии в обрабатываемое вещество зависит, в том числе, и от технологических параметров механической обработки, определяющих механику движения размольных тел, а следовательно, и энергосиловые характеристики процесса. Для изучения влияния передаточного отношения на энергосиловые условия механической обработки разработана, численно реализована и валидирована дискретно-элементная модель движения размольных тел в планетарной мельнице. Определены параметры модели, обеспечивающие разумное согласование экспериментальной и расчетной структур мгновенных изображений размольных тел на установившемся режиме работы мельницы. С помощью модели проведены серии численных экспериментов с варьированием передаточного отношения K от 1 до 2. Показано, что увеличение K в указанном диапазоне ведет к изменению характера движения размольных тел с режима перекатывания на перекатывание и свободный полет. Это снижает число столкновений и одновременно обеспечивает рост их силовых характеристик. Проведен анализ изменения суммарной потери энергии при столкновениях «частица–частица» и «частица–камера». Установлено, что при изменении K от 1 до 2 повышение суммарной потери энергии при столкновениях в основном происходит за счет увеличения потери энергии при столкновениях пар «частица–частица». Разработанные модели и полученные расчетные оценки влияния передаточного отношения на энергосиловые характеристики столкновений могут быть использованы при разработке рациональной технологии механической обработки в планетарной мельнице.

Ключевые слова: высокоэнергетический размол, метод дискретных элементов, энергосиловые характеристики, столкновения, характер движения размольных тел

Благодарности: Авторы выражают благодарность проф. А.С. Рогачеву за помощь в организации и проведении экспериментального исследования. Исследование выполнено за счет гранта Российского научного фонда № 23-29-00889, https://rscf.ru/project/23-29-00889/.

Для цитирования: Аборкин А.В., Елкин А.И., Рябкова В.В., Бугаёв А.П., Бобожанов А.Р., Алымов М.И. Влияние передаточного отношения на энергосиловые условия столкновения размольных тел в планетарной мельнице. *Известия вузов. Порошковая металлургия и функциональные покрытия*. 2025;19(1):5–14. https://doi.org/10.17073/1997-308X-2025-1-5-14

Introduction

Mechanical processing (MP) of solid materials is widely used to initiate changes in the rates of chemical and physicochemical processes required for mechanochemical synthesis, mechanical alloying, mechanical activation, and other applications [1]. Typically, MP is performed in attritors, planetary mills, vibratory mills, and ball mills. The operating principle of these devices is based on repeated impulsive mechanical impacts of grinding bodies on the material, enabling the transfer of mechanical energy into it [2]. Despite the variety of mechanical impact types, the primary modes include impact, shear, and their combinations in various proportions, depending on the type of equipment and its operating conditions [3]. Notably, the type of mechanical impact promoting mechanochemical transformations significantly influences their nature [4].

Processing in planetary mills has found widespread application in solving various technological challenges, such as mechanical alloying/activation, synthesis of composite powder mixtures, and recycling of chip waste, among others [5–7]. Considering the diversity of these technological tasks, their efficient execution, while possible with the same equipment (in this case, a planetary mill), evidently requires the use of different MP parameters. These parameters include the shape and size of the grinding media, the filling ratio of the working chamber, the mass ratio of the processed material to the grinding bodies, the gear ratio, and the rotation frequency of the sun wheel. In most cases, the selection

of these parameters is performed empirically through trial and error, which can be a labor-intensive and sometimes infeasible process. Scientifically grounded parameter selection requires establishing relationships between these parameters, the amount of mechanical energy transferred, and the characteristics of the processed material. Depending on the task, these characteristics may include the granulometric and phase composition, the size of structural components, and others. Numerical determination of the transferred mechanical energy, considering the aforementioned factors influencing the process mechanics, can be achieved through mathematical modeling of grinding body motion, for example, using the discrete element method (DEM) [8–11].

Another significant research direction involves experimental studies of the kinematics of grinding body motion in a planetary mill as a function of MP parameters, conducted, for instance, using high-speed videography [10; 12]. Comprehensive computational and experimental studies allow the kinematic data to be supplemented with energy-force characteristics of collisions between grinding bodies and the walls of the working chamber. This provides a more complete understanding of the processes occurring during MP, enabling predictions of material properties based on processing conditions and facilitating the development of rational technologies that ensure reproducibility of material properties across various equipment types and scalability.

The aim of this study is to develop, numerically implement, and validate a model of grinding body motion in a planetary mill, as well as to investigate the effect of the gear ratio on the motion pattern and energy-force characteristics of grinding body collisions.

Experimental and theoretical research methods

In the experimental part of this study, a laboratory planetary mill “Activator-2S” (Activator Mechanical Engineering Plant, Novosibirsk, Russia) and a high-speed video camera “Phantom Miro M310” (Vision Research Inc., USA) were used. The planetary mill is equipped with two cylindrical working chambers positioned vertically on the sun wheel. One of the chambers was loaded with 12 steel grinding bodies in the form of 9 mm-diameter spheres. To limit vertical displacement of the grinding bodies within the working chamber, the chamber height was set at 1.2 times the sphere diameter. A notable design feature of this mill is the presence of two independent electric motors driving the sun wheel and the working chamber at speeds W and w, respectively. The counter-rotational speeds are controlled via frequency converters. The video camera was positioned above the mill, coaxial to the vertical axis of the sun wheel (see Fig. 1).

For the videography, the steel lids of the working chambers were replaced with transparent ones. The recording speed for all experiments was set to 2000 frames per second. High-speed video recording was conducted for four values of the speed ratio of the working chamber to the sun wheel ($K = w/W$), specifically $K = 1.0$; 1.2; 1.5; 2.0. In these experiments, only the rotation speed of the working chamber was varied, while the rotation speed of the sun wheel remained constant at 694 rpm.

In addition to the experimental studies of grinding body motion, the process was modeled using the discrete element method (DEM). This method describes the translational and rotational dynamics of grinding bodies in the working chamber of a planetary mill using a stepwise algorithm with constant updates of the positions of the bodies and the chamber walls. For each i-th grinding body, a system of two equations of translational and rotational motion is solved, expressed as follows:

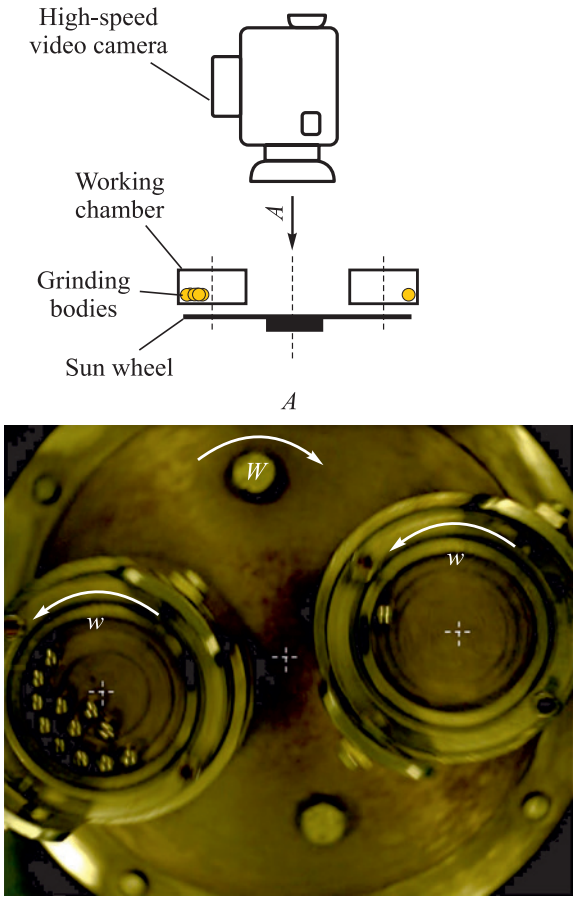

Fig. 1. Schematic of high-speed videography setup

Рис. 1. Схема проведения высокоскоростной видеосъемки

$$m_i \frac{dv_i}{dt} = m_i g + \sum_{j \neq i}^{N} \mathbf{F}_{ij} + \mathbf{F}_i^b,$$
$$I_i \frac{d\boldsymbol{\omega}_i}{dt} = \sum_{j \neq i}^{N} \mathbf{T}_{ij} + \mathbf{T}_i^b + \mathbf{M}_i. \quad (1)$$

The first equation describes the translational motion of the center of mass of the grinding body. The variables m_i and v_i denote the mass and velocity of the i-th body, t is time, and g is the acceleration due to gravity. The first term on the right-hand side accounts for gravitational forces acting on the grinding body, the second term represents interactions between bodies, and the last term accounts for interactions between the grinding body and the chamber walls. The initial velocities of translational and rotational motion are predefined. Since the mass of the working chamber significantly exceeds the total mass of the grinding bodies, the influence of body-wall interactions on the chamber's motion can be neglected, and the motion of the chamber walls is assumed to be known.

The rotational motion of the grinding bodies in the planetary mill is described by the second equation in system (1). The scalar variable I_i denotes the moment of inertia, while the vector variables $\boldsymbol{\omega}_i$, $\mathbf{T}_{ij}$ and $\mathbf{T}_i^b$ represent the angular velocity and torques arising from the interactions of the grinding body with other bodies (indexed j) or with the chamber walls. The term $\mathbf{M}_i$ accounts for rolling friction forces acting on the grinding bodies.

The interactions between the i-th and j-th bodies are represented by forces $\mathbf{F}_{ij}$ and torques $\mathbf{T}_{ij}$, included in equation (1) under the summation sign. Summation over all possible values of $j \neq i$ eliminates self-interaction, considering only contacting grinding bodies. For bodies separated by greater distances, the interaction force is assumed to be zero.

In this study, the calculation of interaction forces and torques between grinding bodies employed Hertz's theory, supplemented by Mindlin's shear theory (the Hertz–Mindlin model) [13]. Since the interactions are not perfectly elastic, an additional dissipative force is introduced alongside the contact force to account for energy losses during collisions. Collisions between grinding bodies and the chamber walls are modeled similarly, but the curvature of the chamber wall surface is neglected, as the chamber radius is significantly larger than the radius of each body.

The model parameters include the physical and mechanical properties of the grinding body material and the chamber, as well as coefficients characterizing their contact interactions. These coefficients include the restitution coefficient (e_R), the static friction coefficient (μ_S), and the rolling friction coefficient (μ_R). While the physical and mechanical properties of most structural materials are available as reference data, determining the coefficients for contact interactions is an independent experimental task, as addressed in studies [14–16]. It should be noted that these coefficients may depend on factors such as the size and shape regularity (deviation from spherical shape) of the grinding bodies, as well as the surface roughness of the grinding bodies and the chamber. Thus, their values require refinement, which in this study was performed by fitting the model to experimental data.

As an initial approximation, based on recommendations in [17; 18], the following values were used: $e_R = 0.85$, $\mu_S = 0.45$ and $\mu_R = 0.02$. A series of numerical simulations replicating the experimental conditions was conducted, varying the contact interaction coefficients. The agreement between experimental and simulated results was evaluated based on the alignment of grinding body position patterns (instantaneous image structures) in the working chamber. Model validation was performed by comparing the areas of experimental and simulated structures of grinding bodies for eight positions of the working chamber under steady-state operation of the planetary mill. The fitting results were deemed satisfactory if the discrepancy (Δ) between experimental and simulated data did not exceed 15 % for the same values of the contact interaction coefficients.

Results and discussion

Table 1 presents typical instantaneous images of grinding bodies obtained experimentally (column "Experiment") and from the simulated results (column "Simulation") for various speed ratios of the working chamber to the sun wheel. Additionally, Table 1 shows images of the areas of experimental and simulated structures of the multiparticle system (column "Comparison"). Finally, Table 1 includes numerical data averaged over 8 positions of the working chamber, showing discrepancies in these areas (Δ), which represent the error of the developed model and characterize its adequacy.

Analysis of the results presented in Table 1 indicates reasonable agreement between the experimental and simulated data, with discrepancies not exceeding 13 %. The fitting parameters were consistent across different speed ratios of the working chamber to the sun wheel. The values of the coefficients (fitting parameters) characterizing contact interactions were as follows: $e_R = 0.75$, $\mu_S = 0.21$ and $\mu_R = 0.023$. It is noteworthy that while the values of e_R and μ_R were closely aligned with or matched those used in modeling in

Table 1. **Comparison of experimental and simulated results**

Таблица 1. **Сопоставление результатов эксперимента и расчетных данных**

$K = w/W$	Experiment	Simulation	Comparison	Δ, %
1.0	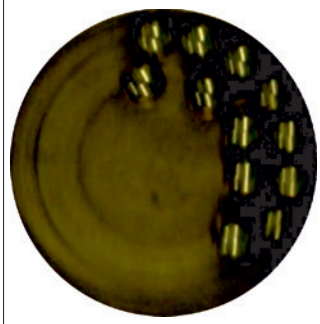	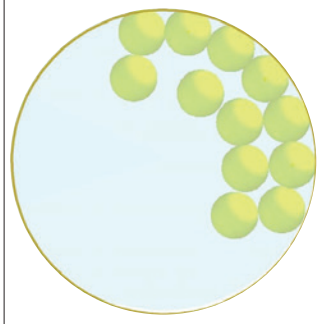	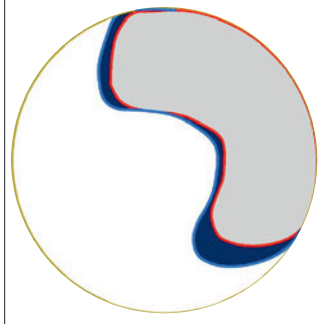	12.4
1.2	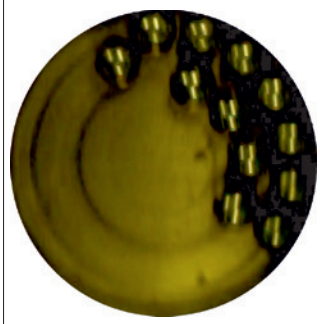	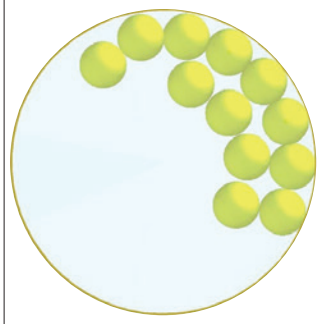	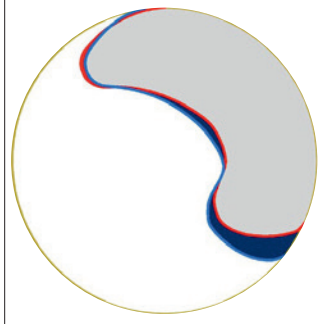	11.9
1.5		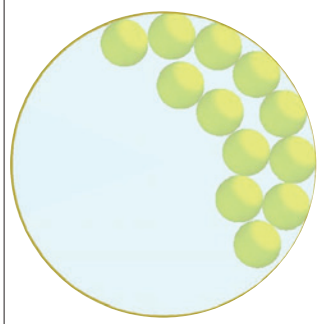	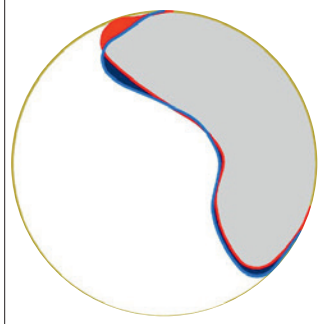	9.1
2.0	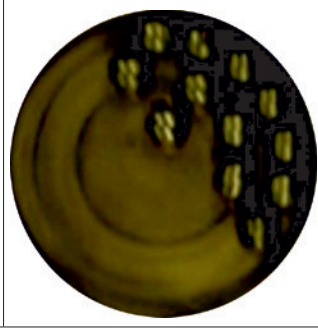	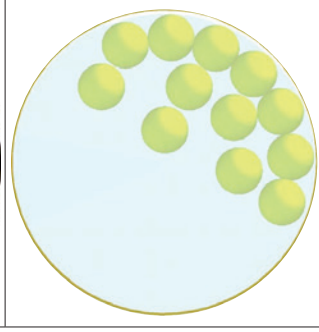	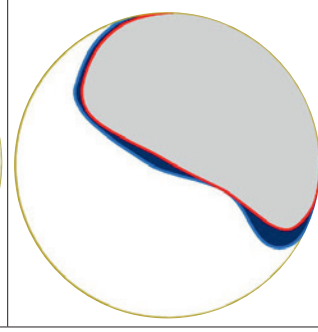	12.2

studies [19; 20], the value of μ_S deviated significantly, exceeding a threefold difference. Nevertheless, μ_S has a substantial impact not only on the motion pattern of the grinding bodies [10] but also on the quantitative energy-force characteristics of collisions, which largely determine their accuracy. Thus, the developed model is adequate and can be used to study the effect of the gear ratio on the motion pattern of grinding bodies during high-energy ball milling and the energy-force parameters of the processing.

Using the developed model, the effect of the gear ratio on the motion pattern of grinding bodies in the working chamber was studied. The analysis of the modeling results shows that changing K from 1.0 to 1.5 has almost no effect on the kinematics of grinding body motion. In contrast, a significant change in the motion pattern is observed when K increases to 2.0. In the first case ($K = 1.0 \div 1.5$), the motion pattern is characterized by the cyclic rolling of the grinding bodies from the first row to the second row. Material

processing in this mode occurs either by abrasion between the chamber wall and the grinding bodies or by collisions between grinding bodies during rolling. In the second case ($K = 2.0$), some grinding bodies move freely relative to the center of the working chamber. This results in three-row rolling, where two or more grinding bodies simultaneously jump to the second row, forming a third row (see Table 1). In this case, in addition to rolling, a partial mode of free flight is realized, where some grinding bodies detach from the chamber wall and are ejected into the free space of the working chamber, flying freely until colliding with another grinding body or the chamber wall. This mode is characterized by the most intense collisions. However, the number of collisions appears to decrease compared to the rolling mode.

Estimates of the effect of the gear ratio on the force characteristics of contact interactions between grinding bodies and between grinding bodies and the chamber walls were also obtained. Fig. 2 presents normalized calculated data on the distribution of collision counts by compression force and shear force for different gear ratios.

It can be observed that an increase in the gear ratio contributes to the growth of the normal collision force (see Fig. 2, *a*). Specifically, changing K from 1 to 2 results in a ~5-fold increase in the maximum normal collision force. A significant differentiation in collision forces is also evident. For instance, if the total number of collisions is conditionally divided based on force into low-intensity ($F < 0.01$), medium-intensity ($0.01 < F < 0.1$), and high-intensity ($F > 0.1$), and their distribution is compared for different gear ratios (see Table 2), it becomes clear that at $K = 1.0 \div 1.5$, the majority of collisions are medium-intensity. In this range of K, the share of medium-intensity collisions increases by no more than 6 %.

Simultaneously, a redistribution of collision intensity occurs. For example, at $K = 1.0$, 32.5 % of collisions are low-intensity, and only 5.6 % are high-intensity. At $K = 1.5$, the proportion of low-intensity collisions

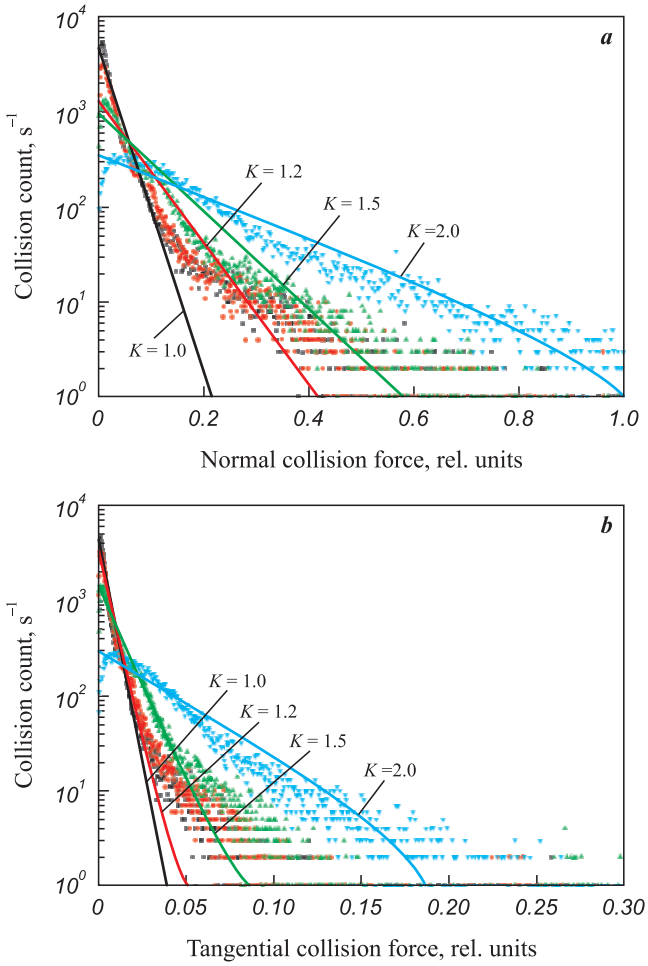

Fig. 2. Changes in normal (***a***) and tangential (***b***) collision forces of grinding bodies at different gear ratios

Рис. 2. Изменение нормальной (***a***) и тангенциальной (***b***) силы столкновений размольных тел при моделировании с различными передаточными отношениями

Table 2. **Distribution of collisions (%) by collision force**

Таблица 2. **Распределение столкновений (%) по силе столкновений**

K	Normal collision force			Tangential collision force		
	$F_n < 0.01$	$0.01 < F_n < 0.1$	$F_n > 0.1$	$F_t < 0.01$	$0.01 < F_t < 0.1$	$F_t > 0.1$
1.0	32.5	61.9	5.6	31.4	63.2	5.4
1.2	24.5	63.6	11.9	24.5	66.3	9.2
1.5	12.1	67.8	20.1	13.0	67.1	19.9
2.0	2.4	42.3	55.3	1.9	38.7	59.4

decreases to 12.1 %, while high-intensity collisions increase to 20.1 %. However, as K increases to 2.0, with the corresponding change in the motion pattern of grinding bodies, the proportion of medium-intensity collisions decreases to 42.3 %. Conversely, the share of high-intensity collisions increases to 55.3 %, although their absolute number significantly declines. A qualitatively similar pattern was observed for tangential forces (see Fig. 2, *b*). It is important to note that at $K = 1.0 \div 1.5$, most collisions are medium-intensity. Assuming that these forces are sufficient to create the required field of mechanical stresses, the activation processing of material particles may be equally effective at $K = 1.0$ and 1.5. In contrast, processing at $K = 2.0$, despite the predominance of high-intensity collisions, might be less effective due to the reduced number of such collisions. This suggests that the $K = 2.0$ regime is more suitable for processing large particles that require greater forces for deformation and fragmentation.

Fig. 3 presents normalized data characterizing the total energy loss during "body–body" and "body–chamber" collisions at different gear ratios, along with the changes in the number of collisions.

Analysis of the graphical dependencies presented shows that as the gear ratio K increases from 1.0 to 2.0, the total energy loss during "body–body" collisions increases by approximately 30 % (see Fig. 3, *a*). However, the energy loss during "body–chamber" collisions remains nearly unchanged for gear ratios K from 1.0 to 1.5, and increases by only ~13 % for $K = 2.0$. This indicates that the increase in total energy loss during collisions is primarily due to changes (increases) in energy loss during "body–body" collision pairs.

The number of collisions decreases predictably with an increase in the gear ratio (see Fig. 3, *b*). While the collision count decreases slightly for $K = 1.0$ and 1.2, it drops significantly at $K = 1.5$ (by ~1.5 times) and even further at $K = 2.0$ (by ~3.1 times). This reduction in collision count can decrease the likelihood of grinding bodies contacting the processed material, thereby reducing the processing efficiency. Thus, an increase in the gear ratio leads to a substantial reduction in the number of collisions while simultaneously increasing the specific energy loss per collision. This compensates for the reduction in collision count and results in a net increase in total energy loss. Interestingly, for process-

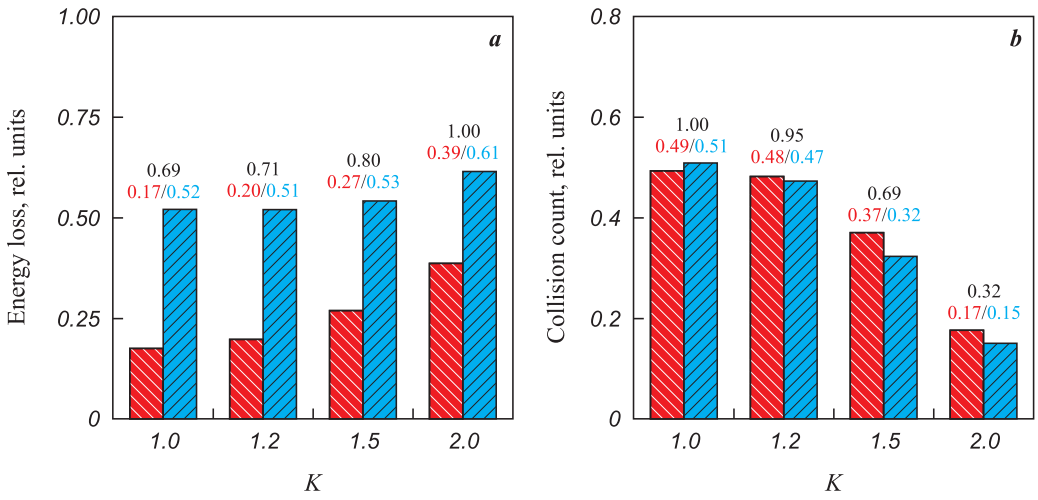

Fig. 3. Total energy loss during "body–body" (■) and "body–chamber" (■) collisions (***a***) and changes in collision count (***b***) for different gear ratios

Рис. 3. Суммарная потеря энергии при столкновениях «тело–тело» (■) и «тело–камера» (■) (***a***) и изменение количества столкновений (***b***) для разных передаточных отношений

ing mixtures of micrometer-sized particles with a high ratio of grinding body mass to material mass, the particles tend to accumulate near the chamber wall due to their ability to pass through voids between grinding bodies [19]. Consequently, despite the increase in total energy loss caused by higher K, the use of $K = 2.0$ may be less effective than lower K values, as "body–body" collisions do not contribute to material processing, and the number of "body–chamber" collisions, despite their increased intensity, decreases significantly. The efficiency of powder mixture processing at higher K values could potentially be improved by using a lower grinding body-to-material mass ratio, where material particles would be distributed not only near the chamber walls but also around its center. This would make better use of "body–body" collisions. Another rational application of the $K = 2.0$ processing regime is for large particles of millimeter-scale size, where higher forces are required for particle deformation, such as in the processing of granular or chip materials.

Conclusion

A model of grinding body motion in the "Activator-2S" planetary mill has been developed, numerically implemented, and validated. The model parameters ensuring its adequacy were determined by comparing experimental and calculated data. Analysis of the model revealed that increasing the gear ratio K from 1.0 to 2.0 decreases the proportion of grinding bodies with limited mobility and transitions their motion from rolling to a combination of rolling and free flight. This leads to an increase in the force characteristics of grinding body collisions while simultaneously reducing their count. Despite significant differentiation in collision forces, the share of medium-intensity collisions remains nearly unchanged for $K = 1.0 \div 1.5$ but decreases with a further increase in K to 2.0, resulting in a higher proportion of high-intensity collisions. Total energy loss during collisions increases by ~30 % as K changes from 1.0 to 2.0. However, energy loss during "body–chamber" collisions remains unchanged for $K = 1.0 \div 1.5$, and the increase in total energy loss is primarily due to higher energy losses during "body–body" collisions. Based on the observed effects of the gear ratio on collision patterns and energy-force characteristics of mechanical processing, the $K = 1.0 \div 1.5$ regime can be recommended for the mechanical processing of micron-sized particles with a high grinding body-to-material mass ratio. The $K = 2.0$ regime appears more suitable for the mechanical processing of larger particles when fragmentation of mixture components is required. The developed model can be applied to evaluate the energy-force characteristics of processing in planetary mills during the technology development stage.

References / Список литературы

1. Zyryanov V.V. Mechanochemical synthesis of complex oxides. *Russian Chemical Reviews*. 2008;77(2):105–135. https://doi.org/10.1070/RC2008v077n02ABEH003709

   Зырянов В.В. Механохимический синтез сложных оксидов. *Успехи химии*. 2008;77(2):107–137. https://doi.org/10.1070/RC2008v077n02ABEH003709
2. Michalchuk A.A.L., Boldyreva E.V., Belenguer A.M., Emmerling F., Boldyrev V.V. Tribochemistry, mechanical alloying, mechanochemistry: What is in a name? *Frontiers in Chemistry*. 2021;9:685789. https://doi.org/10.3389/fchem.2021.685789
3. Lapshin O.V., Boldyreva E.V., Boldyrev V.V. Role of mixing and milling in mechanochemical synthesis (review). *Inorganic Materials and Nanomaterials*. 2021;66(3):433–453. https://doi.org/10.1134/S0036023621030116

   Лапшин О.В., Болдырева Е.В., Болдырев В.В. Роль смешения и диспергирования в механохимическом синтезе (обзор). *Журнал неорганической химии*. 2021;66(3):402–424. https://doi.org/10.31857/S0044457X21030119
4. Tumanov I.A., Achkasov A.F., Мызь Myz S.A., Boldyreva E.V., Boldyrev V.V. Different effect of impact and shear mechanical treatment on mechanochemical cocrystallization of piroxicam and succinic acid. *Doklady Chemistry*. 2014;457(2):154–159. https://doi.org/10.1134/S0012500814080059

   Туманов И.А., Ачкасов А.Ф, Мызь С.А, Болдырева Е.В., Болдырев В.В. Качественно различное влияние сдвиговой и ударной механической нагрузки на механохимическую сокристаллизацию пироксикама и янтарной кислоты. *Доклады Академии наук*. 2014;457(6):670–675. https://doi.org/10.7868/S0869565214240141
5. Suryanarayana C. Mechanical alloying: A critical review. *Materials Research Letters*. 2022;10(10):619–647. https://doi.org/10.1080/21663831.2022.2075243
6. Rogachev A.S., Mukasyan A.S Combustion of heterogeneous nanostructural systems (review). *Combustion, Explosion, and Shock Waves*. 2010;46(3):243–266. https://doi.org/10.1007/s10573-010-0036-2

   Рогачёв А.С., Мукасьян А.С. Горение гетерогенных наноструктурных систем (обзор). *Физика горения и взрыва*. 2010;(3):3–30.
7. Wei L.K., Bin Abd. Rahim S.Z., Al Bakri Abdullah M.M., Yin A.T.M., Ghazali M.F., Omar M.F., Nemes O., Sandu A.V., Vizureanu P., Abdellah A.E.-h. Producing metal powder from machining chips using ball milling process: A Review. *Materials*. 2023;16(13):4635. https://doi.org/10.3390/ma16134635
8. Burmeister C., Titscher L., Breitung-Faes S., Kwade A. Dry grinding in planetary ball mills: Evaluation of a stressing model. *Advanced Powder Technology*. 2018;29(1):191–201. https://doi.org/10.1016/j.apt.2017.11.001
9. Santhanam P.R., Dreizin E.L. Predicting conditions for scaled-up manufacturing of materials prepared by ball milling. *Powder Technology*. 2012;221:403–411. https://doi.org/10.1016/j.powtec.2012.01.037

10. Rosenkranz S., Breitung-Faes S., Kwade A. Experimental investigations and modelling of the ball motion in planetary ball mills. *Powder Technology*. 2011;212:224–230. https://doi.org/10.1016/j.powtec.2011.05.021

11. Kozawa T., Fukuyama K., Kushimoto K., Ishihara S., Kano J., Kondo A., Naito M. Effect of ball collision direction on a wet mechanochemical reaction. *Scientific Reports*. 2021;11(1):210. https://doi.org/10.1038/s41598-020-80342-w

12. Rogachev A.S., Moskovskikh D.O., Nepapushev A.A., Sviridova T.A., Vadchenko S.G., Rogachev S.A., Mukasyan A.S. Experimental investigation of milling regimes in planetary ball mill and their influence on structure and reactivity of gasless powder exothermic mixtures. *Powder Technology*. 2015;274(2):44–52. https://doi.org/10.1016/j.powtec.2015.01.009

13. Mindlin R.D., Deresiewicz H. Elastic spheres in contact under varying oblique force. *Journal of Applied Mechanics*. 1953;20(3):327–344. https://doi.org/10.1115/1.4010702

14. Aryaei A., Hashemnia K., Jafarpur K. Experimental and numerical study of ball size effect on restitution coefficient in low velocity impacts. *International Journal of Impact Engineering*. 2010;37(10):1037–1044. https://doi.org/10.1016/j.ijimpeng.2010.04.005

15. Hlosta J., Žurovec D., Rozbroj J., Ramírez-Gómez Á., Nečas J., Zegzulka J. Experimental determination of particle–particle restitution coefficient via double pendulum method. *Chemical Engineering Research and Design*. 2018;135:222–233. https://doi.org/10.1016/j.cherd.2018.05.016

16. Hlosta J., Jezerská L., Rozbroj J., Žurovec D., Nečas J., Zegzulka J. DEM investigation of the influence of particulate properties and operating conditions on the mixing process in rotary drums: Part 1 – Determination of the DEM parameters and calibration process. *Processes*. 2020;8(2):222. https://doi.org/10.3390/pr8020222

17. Gusev V.G., Sobolkov A.V., Aborkin A.V. Determination of the coefficient of restitution upon contact of a steel ball with aluminum and steel surfaces. *Journal of Physics: Conference Series*. 2021;2131(3):032087. https://doi.org/10.1088/1742-6596/2131/3/032087

18. Gusev V.G., Sobol'kov A.V., Aborkin A.V., Alymov M.I. Simulation of the energy–force parameters of planetary ball mill processing and estimation of their influence on the particle size in an AMg2 alloy/graphite composite powder. *Russian Metallurgy (Metally)*. 2019;(1):24–30. https://doi.org/10.1134/S0036029519010063

Гусев В.Г., Соболькоов А.В., Аборкин А.В., Алымов М.И. Моделирование энергосиловых параметров обработки в планетарной мельнице и оценка их влияния на размер частиц композиционного порошка сплав АМг2/графит. *Металлы*. 2019;(1):27–34.

19. Hirosawa F., Iwasaki T. Dependence of the dissipated energy of particles on the sizes and numbers of particles and balls in a planetary ball mill. *Chemical Engineering Research and Design*. 2021;167:84–95. https://doi.org/10.1016/j.cherd.2020.12.024

20. Capece M., Davé R.N., Bilgili E. On the origin of nonlinear breakage kinetics in dry milling. *Powder Technology*. 2015;272:189–203. https://doi.org/10.1016/j.powtec.2014.11.040

Information about the Authors

Artemiy V. Aborkin – Cand. Sci. (Eng.), Associate Professor of the Department of mechanical engineering technology of Vladimir State University named after Alexander and Nikolay Stoletovs (VlSU)
ORCID: 0000-0003-4979-7164
E-mail: aborkin@vlsu.ru

Aleksey I. Elkin – Cand. Sci. (Eng.), Director of the Institute of Mechanical Engineering and Automobile Transport of VlSU
ORCID: 0000-0001-5842-9625
E-mail: elkin@vlsu.ru

Varvara V. Ryabkova – Junior Researcher at the VlSU
ORCID: 0009-0000-5757-6922
E-mail: VVRyabkova@mail.ru

Aleksandr P. Bugayov – Postgraduate Student of VlSU
ORCID: 0009-0006-0441-5264
E-mail: bugaev689@gmail.com

Anis R. Bobozhanov – Junior Researcher, Graduate Student at the A.G. Merzhanov Institute of Structural Macrokinetics and Problems of Materials Science of the Russian Academy of Sciences (ISMAN)
ORCID: 0009-0008-7021-7156
E-mail: bobozhanov.anis@mail.ru

Mikhail I. Alymov – Dr. Sci. (Eng.), Corresponding Member of the Russian Academy of Sciences, Director of the ISMAN
ORCID: 0000-0001-6147-5753
E-mail: alymov@ism.ac.ru

Сведения об авторах

Артемий Витальевич Аборкин – к.т.н., доцент кафедры «Технология машиностроения» Владимирского государственного университета им. А.Г. и Н.Г. Столетовых (ВлГУ)
ORCID: 0000-0003-4979-7164
E-mail: aborkin@vlsu.ru

Алексей Иванович Елкин – к.т.н., директор Института машиностроения и автомобильного транспорта ВлГУ
ORCID: 0000-0001-5842-9625
E-mail: elkin@vlsu.ru

Варвара Викторовна Рябкова – мл. науч. сотрудник ВлГУ
ORCID: 0009-0000-5757-6922
E-mail: VVRyabkova@mail.ru

Александр Павлович Бугаёв – магистрант ВлГУ
ORCID: 0009-0006-0441-5264
E-mail: bugaev689@gmail.com

Анис Рахмонович Бобожанов – мл. науч. сотрудник, аспирант Института структурной макрокинетики и проблем материаловедения им. А.Г. Мержанова Российской академии наук (ИСМАН)
ORCID: 0009-0008-7021-7156
E-mail: bobozhanov.anis@mail.ru

Михаил Иванович Алымов – д.т.н., член-корр. РАН, директор ИСМАН
ORCID: 0000-0001-6147-5753
E-mail: alymov@ism.ac.ru

Contribution of the Authors

A. V. Aborkin – defined the research objectives, developed the research methodology, participated in result discussions, and reviewed and edited the manuscript
A. I. Elkin – defined the research objectives, developed and validated the discrete element model, drafted the manuscript, and participated in result discussions.
V. V. Ryabkova – developed the discrete element model, conducted numerical experiments, participated in result discussions.

A. P. Bugayov – conducting numerical experiments.
A. R. Bobozhanov – performed the experimental study.

M. I. Alymov – participated in result discussions and reviewed and edited the manuscript.

Вклад авторов

А. В. Аборкин – определение цели работы, разработка методологии исследования, участие в обсуждении результатов, рецензирование и редактирование.
А. И. Елкин – определение цели работы, разработка и валидация дискретно-элементной модели, написание текста статьи, участие в обсуждении результатов.
В. В. Рябкова – участие в разработке дискретно-элементной модели, обработка данных численного эксперимента, участие в обсуждении результатов.
А. П. Бугаёв – проведение численных экспериментов.
А. Р. Бобожанов – проведение экспериментального исследования.
М. И. Алымов – участие в обсуждении результатов, рецензирование и редактирование.

Received 15.10.2024
Revised 26.11.2024
Accepted 29.11.2024

Статья поступила 15.10.2024 г.
Доработана 26.11.2024 г.
Принята к публикации 29.11.2024 г.

Theory and Processes of Formation and Sintering of Powder Materials
Теория и процессы формования и спекания порошковых материалов

UDC 621.762.1
https://doi.org/10.17073/1997-308X-2025-1-15-22

Research article
Научная статья

Effect of quenching and tempering on the structure and properties of hot-deformed powder steels with ultrafine particles

M. S. Egorov, **R. V. Egorova**, **A. V. Mozgovoy**,
K. V. Gantimurov, **M. V. Kovtun**

Don State Technical University
1 Gagarina Sq., Rostov-on-Don, 344003 Russia

aquavdonsk@mail.ru

Abstract. This study examines the effect of quenching and tempering on the structure and mechanical properties of hot-deformed powder steels containing ultrafine particles. The research analyzes the structural transformations and mechanical responses during quenching and tempering, focusing on the relationship between heat treatment conditions and the resulting material properties. The experiments involved variations in quenching temperature and tempering time, allowing the identification of optimal conditions for achieving a favorable combination of strength and ductility. The findings highlight the potential to achieve a homogeneous microstructure and high mechanical performance, making these materials suitable for high-load applications. This study underscores the significance of tailoring heat treatment parameters to control both microstructural and mechanical characteristics, thereby broadening the industrial applicability of powder steels.

Keywords: heat treatment, powder steels, ultrafine particles, mechanical properties

For citation: Egorov M.S., Egorova R.V., Mozgovoy A.V., Gantimurov K.V., Kovtun M.V. Effect of quenching and tempering on the structure and properties of hot-deformed powder steels with ultrafine particles. *Powder Metallurgy and Functional Coatings*. 2025;19(1):15–22. https://doi.org/10.17073/1997-308X-2025-1-15-22

Влияние режимов закалки и отпуска на структуру и свойства горячедеформированных порошковых сталей с ультрадисперсными частицами

М. С. Егоров, **Р. В. Егорова**, **А. В. Мозговой**,
К. В. Гантимуров, **М. В. Ковтун**

Донской государственный технический университет
Россия, 344003 г. Ростов-на-Дону, пл. Гагарина, 1

aquavdonsk@mail.ru

Аннотация. Рассматривается влияние режимов закалки и отпуска на структуру и механические свойства горячедеформированных порошковых сталей, содержащих ультрадисперсные частицы. Исследование основано на анализе термических и механических процессов, протекающих при закалке и отпуске, а также их связи с характером структурных изменений, происходящих в материале. Эксперименты включали вариации температуры закалки и времени отпуска, что позволило выявить оптимальные режимы для достижения наилучших механических характеристик – таких, как прочность и пластичность. Полученные результаты указывают на возможность достижения высокой прочности, что делает эти материалы

перспективными для применения в условиях высокой нагрузки. Подчеркивается значимость выбора режимов термообработки для управления микро- и макроструктурой порошковых сталей, что открывает новые возможности для их использования в различных отраслях промышленности.

Ключевые слова: термическая обработка, порошковые стали, ультрадисперсные частицы, механические свойства

Для цитирования: Егоров М.С., Егорова Р.В., Мозговой А.В., Гантимуров К.В., Ковтун М.В. Влияние режимов закалки и отпуска на структуру и свойства горячедеформированных порошковых сталей с ультрадисперсными частицами. *Известия вузов. Порошковая металлургия и функциональные покрытия*. 2025;19(1):15–22.
https://doi.org/10.17073/1997-308X-2025-1-15-22

Introduction

The properties of powder steels can be improved by complicating their composition and by applying thermal and thermochemical treatments. However, these methods of enhancing the properties of powder steels are characterized by certain challenges, primarily due to residual porosity and chemical and structural heterogeneity [1].

The influence of the structure of powder steels on the thermodynamics of new phase nucleation and transformation kinetics can be controlled through manufacturing technology. The formation of hot-deformed powder steels (HDPS) with minimal residual porosity aligns their critical points more closely with those of compact materials. The quenching temperature for powder steels is primarily determined by the critical points A_{c1} (the temperature at which austenite begins to transform into pearlite or another phase during cooling and where ferrite starts transforming into austenite during heating) and A_{c3} (the temperature at which ferrite begins to transform into austenite during heating – a key process for achieving the required steel properties), as well as the carbon content. HDPS are inherently fine-grained. Alloying with non-carbide-forming elements does not affect the tendency of austenite grains to grow at heating temperatures up to 1100 °C. This feature expands the temperature range for quenching; for HDPS with 0.5 % carbon content, this range is 825–845 °C [2–5].

The aim of this study is to investigate the quenching and tempering regimes to determine the optimal mechanical properties of hot-deformed powder steels containing ultrafine particles.

Materials and methods

The study utilized domestic powders of grades PZhRV 2.200.26 (TU 14-1-5365-98, water-atomized and reduced iron powder) and N4D2M (TU 14-5402-2002, alloyed powder) produced by Severstal PJSC (Cherepovets, Russia) [4; 5]. Ultrafine additives of silicon nitride (Si_3N_4) and nickel oxide (NiO) produced by Plazmoterm (Moscow, Russia) [6] were added to the charge.

Before use, the powders were analyzed using the Analysette 22 MicroTecplus universal laser particle size analyzer (Fritsch, Germany) and the Beckman Coulter AU480 submicron particle analyzer (USA). The charge was prepared using an RT-NM05S twin-cone mixer (Taiwan) and an Assonic SPC ultrasonic station (China) for sieving and mixing powders with ultrafine particles. Static cold pressing was performed on a TS0500-6 hydraulic press (China) with a maximum load capacity of 50 tons using laboratory dies. Homogenizing sintering was carried out in the heat treatment laboratory of the "Materials Science and Metal Technology" department of DSTU in an SNOL 6.7/1300 muffle electric furnace (AB UMEGA, Lithuania) at temperatures ranging from 900 °C to 1150 °C in a protective gas atmosphere of dissociated ammonia. The sintering time ranged from 15 to 180 min. Subsequent heat treatment of the hot-deformed powder steels was conducted in the same furnaces.

Dynamic hot pressing (DHP) of the billets was performed on a K2232 crank press (Russia) with single-action operation. Before the DHP operation, powder billets were heated in a muffle electric resistance furnace (950–1150 °C) in a dissociated ammonia atmosphere. The furnace temperature was monitored using a platinum-palladium thermocouple [7].

Tensile tests were conducted in accordance with GOST 18227-85 using an MGS-V15 servo-hydraulic floor testing machine in automatic mode with a personal computer. Fig. 1 shows the diagram of the sample subjected to testing.

The hardness of the samples was measured using a Rockwell hardness tester (TK-2M, Tochmashpribor, Ivanovo, Russia) with diamond cone indentation under a total load of 1471 N.

The samples of PZhRV 2.200.26 + 0.5 % C and N4D2M + 0.5 % C were subjected to quenching followed by tempering after hot re-pressing at t = 1150 °C, with the addition of ultrafine particles (2 % NiO, 0.1 % Si_3N_4) to each material. Cooling was performed

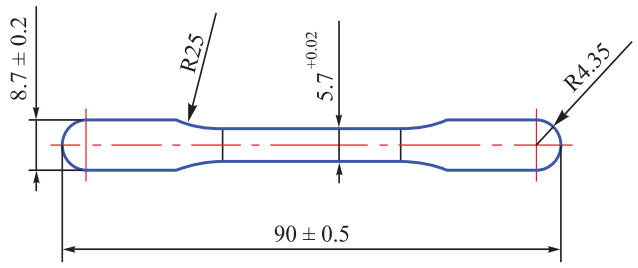

Fig. 1. Technical drawing of the sample for tensile testing

Рис. 1. Чертеж образца для испытания на растяжение

in water and oil, with cooling rates at the temperature of minimum austenite stability being 600–500 °C/s (in water) and 150–100 °C/s (in oil), respectively. The chemical composition of the studied powders, the characteristics of the ultrafine particles, and the technology for producing sintered samples are described in detail in [2].

Results and discussion

Quenching of hot-deformed powder steels (HDPS) makes it possible to obtain a homogeneous martensitic structure with high hardness (*HV* = 7.5 GPa). This is due to the low porosity and favorable structure formed during hot pressing.

Fig. 2 shows the microstructure of HDPS based on PZhRV 2.200.26 powder containing 0.5 % C + + 2 % NiO. The martensitic structure is clearly defined, with a small number of pores up to 3 μm in size. This quenched steel structure does not contain ferrite or retained austenite, confirming that the quenching process was conducted correctly [8; 9]. The hardness of the quenched HDPS at a quenching temperature of 835 °C is presented in Table 1.

Modification of steels with silicon nitride increases hardness after quenching. The final formation of the structure and properties of HDPS occurs during tempering. The effect of tempering temperature on the mechanical properties of HDPS is presented in Table 2.

For all the studied materials, a similar trend in property changes is observed: as the tempering temperature increases, the ultimate strength (σ_v) and hardness (*HRC*) of the steels decrease, while the ductility parameter (ψ) increases, reaching its maximum t = 550 °C. At this temperature, the overall set of mechanical properties is superior to those of the initial and annealed steels [7–9].

The microstructures of quenched and tempered HDPS N4D2M + 0.5 % C + 2 % NiO are shown in Fig. 3.

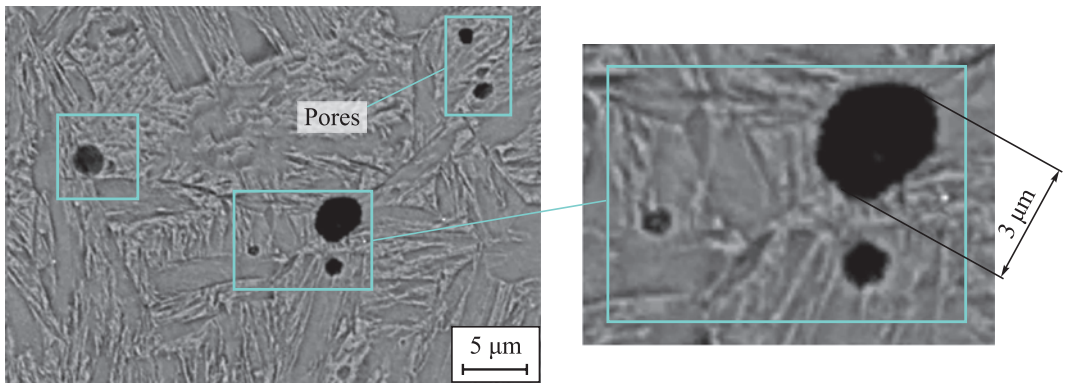

Fig. 2. Martensite of hot-deformed powder steel of PZhRV grade 2.200.26 + 0.5 % C + 2 % NiO
Pore size: 1–3 μm

Рис. 2. Мартенсит горячедеформированной порошковой стали марки ПЖРВ 2.200.26 + 0,5 % C + 2 % NiO
Размер пор: 1–3 мкм

Table 1. **Hardness (*HRC*) of quenched HDPS**

Таблица 1. **Твердость (*HRC*) закаленных ГДПС**

Powder steel					
PZhRV 2.200.26 + 0.5 % C	PZhRV 2.200.26 + 0.5 % C + 2 % NiO	PZhRV 2.200.26 + 0.5 % C + 0.1 % Si_3N_4	N4D2M + 0.5 % C	N4D2M + 0.5 % C + 2 % NiO	N4D2M + 0.5 % C + 0.1 % Si_3N_4
Cooling medium					
Water			Oil		
50–52	50–52	54	49–51	49–51	55

Table 2. **Dependence of mechanical properties of HDPS on tempering temperature**

Таблица 2. **Зависимость механических свойств ГДПС от температуры отпуска**

HDPS composition	Tempering temperature, °C	σ_v, MPa	ψ, %	*HRC*
PZhRV 2.200.26 + 0.5 % C	250	1180	18	45
	350	920	22	42
	450	825	30	38
	550	760	35	33
PZhRV 2.200.26 + 0.5 % C + 0.1 % Si_3N_4	250	1230	18	47
	350	950	22	45
	450	860	30	40
	550	780	35	35
PZhRV 2.200.26 + 0.5 % C + 2 % NiO	250	1190	19	45
	350	935	23	42
	450	840	29	38
	550	765	35	33
N4D2M + 0.5 % C	250	1420	16	46
	350	1260	20	43
	450	1090	28	39
	550	1070	32	34
N4D2M + 0.5 % C + 0.1 % Si_3N_4	250	1450	17	48
	350	1290	24	46
	450	1130	30	41
	550	1090	34	35
N4D2M + 0.5 % C + 2 % NiO	250	1430	16	46
	350	1270	20	43
	450	1100	28	39
	550	1080	32	32

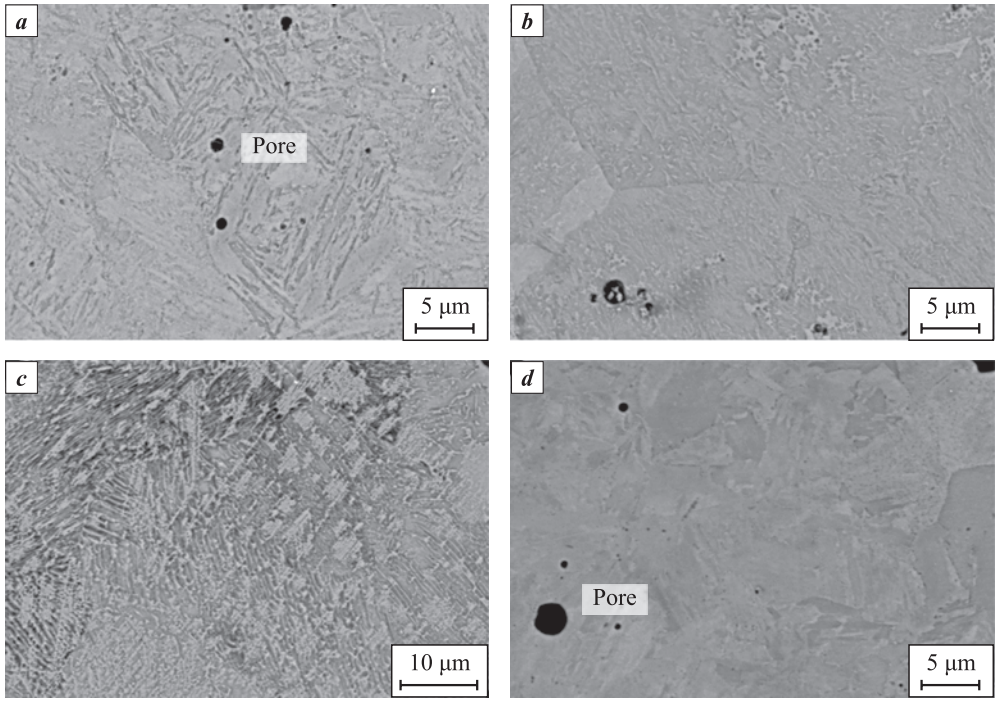

Fig. 3. Microstructure of H4D2M + 0.5 % C + 2 % NiO after quenching and tempering at different temperatures
t, °C: 250 (***a***); 350 (***b***); 450 (***c***); 550 (***d***)

Рис. 3. Микроструктура Н4Д2М + 0,5 % С + 2 % NiO после закалки и отпуска при различной температуре
t, °C: 250 (***a***); 350 (***b***); 450 (***c***); 550 (***d***)

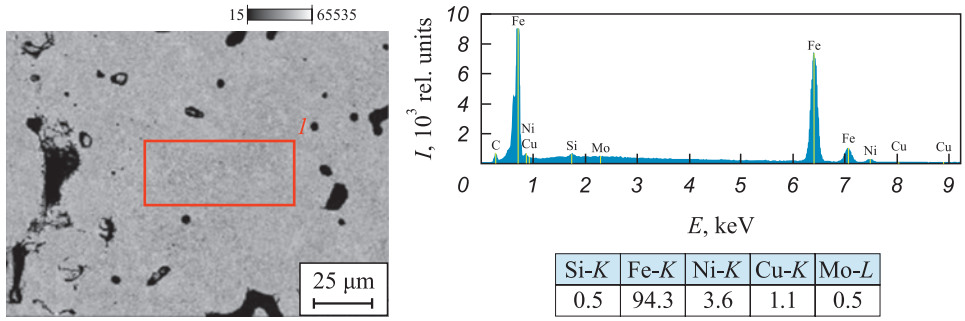

Si-*K*	Fe-*K*	Ni-*K*	Cu-*K*	Mo-*L*
0.5	94.3	3.6	1.1	0.5

Fig. 4. Results of micro-*X*-ray spectral analysis of powder steel H4D2M + 0.5 % C + 2 % NiO after heat treatment (quenching and tempering)

Рис. 4. Результаты микрорентгеноспектрального анализа порошковой стали Н4Д2М + 0,5 % С + 2 % NiO после проведения термической обработки (закалка и отпуск)

Thus, quenching and tempering allow for achieving the desired structure of HDPS [9–11]. The level of mechanical properties of HDPS depends on the quality of interparticle bonding formed during the sintering and hot re-pressing stages. If this bonding is incomplete, it is not possible to improve mechanical properties through strengthening heat treatment [11; 12].

To monitor the chemical composition of the powder steels obtained after heat treatment (quenching and tempering), a micro *X*-ray spectral analysis was performed using a scanning electron microscope (S-3400N, Hitachi, Japan) [12; 13]. The results are presented in Fig. 4.

The presence of all alloying elements in the powder steel after heat treatment was verified through micro-*X*-ray spectral analysis [7; 10; 12].

Fractographic analysis using the S-3400N scanning electron microscope highlighted the characteristic features of HDPS fractures following heat treatment (quenching and tempering). The fracture surfaces of the quenched and tempered HDPS samples are presented in Fig. 5.

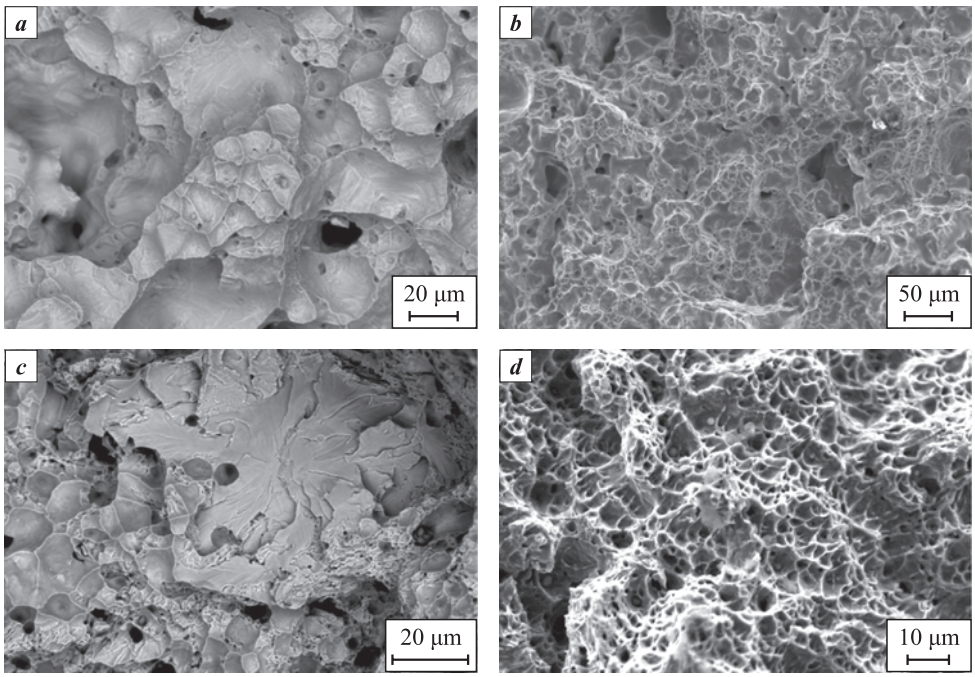

Fig. 5. Fractographs of powder steels with ultrafine particles after tempering
t, °C: 250 (***a***, ***c***); 550 (***b***, ***d***)
a, ***b*** – H4D2M + 0.5 % C + 2 % NiO; ***c***, ***d*** – PZHRV 2.200.26 + 0.5 % C + 2 % NiO

Рис. 5. Фрактограммы изломов порошковых сталей с ультрадисперсными частицами после отпуска
t, °C: 250 (***а***, ***в***); 550 (***б***, ***г***)
а, ***b*** – Н4Д2М + 0,5 % С + 2 % NiO; ***c***, ***d*** – ПЖРВ 2.200.26 + 0,5 % С + 2 % NiO

An analysis of the fractographs revealed that the dominant features on the fracture surfaces of HDPS tempered at $t = 250$ °C are intergranular and transgranular cleavages, appearing at different levels and distinguished by varying sizes of the crack propagation zones [14–16]. In Fig. 5, *a* and *c* steps on large cleavage elements are clearly visible, giving the structure a river-like pattern – a characteristic feature of intergranular fracture. On smaller facets, smooth surfaces formed by crack propagation along crystallographic planes are observed, which are typical of transgranular cleavage [17–20]. Discontinuities in both intergranular and transgranular cleavage zones make it difficult to identify the preferred site of crack initiation. This observation indirectly suggests a balance of interatomic bonding forces within grains and along grain boundaries, indicating the successful formation of intragranular bonding during HDPS production [2; 12].

Conclusion

The study examined the effects of quenching and tempering on the structure and properties of HDPS with ultrafine particles. Maximum hardness at a quenching temperature of 835 °C was observed in steels with compositions PZhRV 2.200.26 + 0.5 % C + 0.1 % Si_3N_4 (*HRC* = 54) and N4D2M + 0.5 % C + 0.1 % Si_3N_4 (*HRC* = 55). Modifying steels with silicon nitride improved hardness after quenching. For these steels, maximum ultimate strength values were recorded at a tempering temperature of 250 °C: σ_v = 1230 MPa (PZhRV 2.200.26 + 0.5 % C + 0.1 % Si_3N_4) and σ_v = 1450 MPa (N4D2M + 0.5 % C + 0.1 % Si_3N_4). At 550 °C, these steels exhibited maximum ductility indicators: ψ = 35 % (PZhRV 2.200.26 + 0.5 % C + + 0.1 % Si_3N_4) and ψ = 34 % (N4D2M + 0.5 % C + + 0.1 % Si_3N_4). The addition of 0.1 % Si_3N_4 increased ultimate strength at 250 °C by 50 MPa for PZhRV 2.200.26 + 0.5 % C and by 30 MPa for N4D2M + 0.5 % C. Adding 2 % NiO to both materials slightly improved strength properties (by 10–15 MPa).

For HDPS tempered at 550 °C, the fracture surfaces predominantly displayed a dimpled morphology, with individual dimples ranging in diameter from 8 to 20 μm. The clear resolution of dimple depths and ridge heights indicates the material's high capacity for microplastic deformation at the crack propagation site [19; 20].

This study demonstrates that strengthening heat treatment is a key tool for enhancing the mechanical properties of hot-deformed powder steels. By carefully adjusting quenching and tempering conditions, it is possible to improve the material's strength, ductility, and hardness. Managing mechanical properties depends on the effective formation of intragranular bonding during production, which optimizes the microstructure and significantly enhances the performance of the final product. The combination of heat treatment and bonding control offers a promising pathway for advancing the quality and functionality of powder steels. These findings open new opportunities for developing materials with tailored properties, which are essential for modern mechanical engineering and other high-tech industries [10; 12].

References / Список литературы

1. Kuhn H.A., Ferguson B.L. Powder forging. Princeton, New Jersey: MPIF, 1990. 270 p.
2. Egorov M.S., Egorova R.V., Lopatin V.Yu. Phase transformations in powder sintered steels during cooling. *Safety of Technogenic and Natural Systems*. 2024;8(3):67–77. (In Russ.). https://doi.org/10.23947/2541-9129-2024-8-3-67-77

   Егоров М.С., Егорова Р.В., Лопатин В.Ю. Фазовые превращения в порошковых спеченных сталях при охлаждении. *Безопасность техногенных и природных систем*. 2024;8(3):67–77. https://doi.org/10.23947/2541-9129-2024-8-3-67-77
3. Bernshtein M.L., Kaputkina L.M., Konyukova E.V., Nikishov N.A., Shakhkerimov R.N. Changes in the structure of thermomechanically hardened austenite under the effect of temperature and deformation. *Russ. Metallurgy. Metally*. 1985;(1):80–88.
4. Chen N., Luo R., Xiong H., Li Z. Dense M2 high speed steel containing core-shell MC carbonitrides using high-energy ball milled M2/VN composite powders. *Materials Science and Engineering: A*. 2020;771:138628. https://doi.org/10.1016/j.msea.2019.138628
5. Chaus A.S. Structural and phase changes in carbides of the high-speed steel upon heat treatment. *The Physics of Metals and Metallography*. 2016;117(7):684–692. https://doi.org/10.1134/S0031918X16070048

   Чаус А.С. Структурные и фазовые изменения в карбидах при термической обработке быстрорежущей стали. *Физика металлов и металловедение*. 2016;117(7):706–714.
6. Plasmotherm LLC. Metal Nanopowders. URL: http://plasmotherm.ru/catalog/metal/item_4.html (accessed: 18.05.2024). (In Russ.).

   Компания ООО «Плазмотерм». Нанопорошки металлов. URL: http://plasmotherm.ru/catalog/metal/item_4.html (дата обращения: 18.05.2024).
7. Dorofeev Yu.G., Dorofeev V.Yu., Kochkarova H.S. Features of the distribution of microalloying elements in hotly deformed iron-based powder materials and their effect on the quality of interparticle splicing. *Metal Science and Heat Treatment*. 2013;(8):35–39. (In Russ.). https://doi.org/10.1007/s11041-013-9650-4

   Дорофеев Ю.Г., Дорофеев В.Ю., Кочкарова Х.С. Особенности распределения микролегирующих элементов в горячедеформированных порошковых материа-

лах на основе железа и их влияния на качество межчастичного сращивания. *Металловедение и термическая обработка металлов*. 2013;(8):35–39. https://doi.org/10.1007/s11041-013-9650-4

8. Pelletiers T.W., Daye W.K. Copper-infiltrated steels. *Powder Metallurgy*. 1998;(7):326–330. https://doi.org/10.31399/asm.hb.v07.a0006076
9. Hendrickson A.A., Machmeier P.M., Smith D.W. Impact forging of sintered steel performs. *Powder Metallurgy.* 2000; 43(4):327–344.
10. Panov V.S., Skorikov R.A. The influence of nanosized dopants on the structure and properties of powder carbon steels. *Nanotekhnologii: nauka i proizvodstvo*. 2015; 35(3):40–45. (In Russ.).

    Панов В.С., Скориков Р.А. Влияние наноразмерных легирующих добавок на структуру и свойства порошковых углеродистых сталей. *Нанотехнологии: наука и производство*. 2015;35(3):40–45.
11. Egorov M.S., Egorova R.V., Kovtun M.V. Influence of carbon content on the formation of a contact interparticle surface during hot post-pressing. *Safety of Technogenic and Natural Systems*. 2023;7(2):90–101. (In Russ.). https://doi.org/10.23947/2541-9129-2023-7-2-90-101

    Егоров М.С., Егорова Р.В., Ковтун М.В. Влияние содержания углерода на формирование контактной межчастичной поверхности при горячей допрессовке. *Безопасность техногенных и природных систем*. 2023;7(2):90–101. https://doi.org/10.23947/2541-9129-2023-7-2-90-101
12. Egorov M.S. Scientific and technological principles of interparticle splicing of sintered and hot-deformed powder steels modified with ultrafine particles. In: *Proceedings of the 16th International Scientific and Technical Conference "New materials and technologies: powder metallurgy, composite materials, protective coatings, welding"* (Minsk, 22–24 May 2024). Minsk: Publ. house "Belarusskaya nauka", 2024. P. 63–67. (In Russ.).

    Егоров М.С. Научно-технологические принципы межчастичного сращивания спеченных и горячедеформированных порошковых сталей, модифицированных ультрадисперсными частицами. В сб.: *Материалы 16-й Междунар. науч.-техн. конференции «Новые материалы и технологии: порошковая металлургия, композиционные материалы, защитные покрытия, сварка»* (Минск, 22–24 мая 2024 г.). Минск: Изд. дом «Белорусская наука», 2024. С. 63–67.
13. Dyachkova L.N., Dechko M.M. The effect of nanodisperse additives on the structure and properties of powdered carbon and high-chromium steel. *Nanotekhnologii: nauka i proizvodstvo*. 2015;35(3):5–14. (In Russ.).

    Дьячкова Л.Н., Дечко М.М. Влияние нанодисперсных добавок на структуру и свойства порошковой углеродистой и высокохромистой стали. *Нанотехнологии: наука и производство*. 2015;3(35):5–14.
14. Dorofeyev V.Y., Sviridova A.N., Samoilov V.A. Formation of structure and properties of hot-deformed powder steels microalloyed with sodium and calcium in the process of thermal and thermomechanical treatment. *Russian Journal of Non-Ferrous Metals*. 2021;62(6):723–731. https://doi.org/10.3103/S1067821221060080

    Дорофеев В.Ю., Свиридова А.Н., Самойлов В.А. Формирование структуры и свойств горячедеформированных порошковых сталей, микролегированных натрием и кальцием, при термической и термомеханической обработках. *Известия вузов. Порошковая металлургия и функциональные покрытия*. 2021;15(3):22–33. https://doi.org/10.17073/1997-308X-2021-3-22-33
15. Nasibulin A.G., Queipo P., Shandakov S.D., Brown D.P., Jiang H., Pikhista P.V., Kauppinen E.I. Studies of mechanism of single-walled carbon nanotube formation. *Journal of Nanoscience and Nanotechnology*. 2006;6(5): 1233–1246. https://doi.org/10.1166/jnn.2006.340
16. Dorofeyev V.Y., Sviridova A.N., Berezhnoy Y.M., Bessarabov E.N., Kochkarova K.S., Pustovoit V.N., Sviridova S.V. Structure and properties of hot-deformed powder steels microalloyed by aluminium. *IOP Conference Series: Materials Science and Engineering*. 2020; 862(2):022045. http://doi.org/10.1088/1757-899X/862/2/022045
17. Gilardi R., Alzati L., Oro R., Hryha E., Nyborg L., Berg S. Reactivity of carbon based materials for powder metallurgy parts and hard metal powders manufacturing. *Journal of the Japan Society of Powder and Powder Metallurgy*. 2016;63(7):548–554. https://doi.org/10.2497/jjspm.63.548
18. Rojek J., Nosewicz S., Mazdziarz M., Kowalczyk P., Wawrzyk K., Lumelskyj D. Modeling of a sintering process at various scales. *Procedia Engineering*. 2017;177:263–270. https://doi.org/10.1016/j.proeng.2017.02.210
19. Gostev A.S., Gosteva E.G., Gulevsky V.A. The role of nanopowders in alloy modification. *Young Scientist*. 2010;22(11):53–55. (In Russ.).

    Гостев А.С., Гостева Е.Г., Гулевский В.А. Роль нанопорошков в модифицировании сплавов. *Молодой ученый*. 2010;22(11):53–55.
20. Eremeeva Zh.V., Nitkin N.M., Sharipzyanova G.H. Features of the application of nanoscale carbon and chromium powders to the processes of charge preparation and pressing of powder steels. *Izvestiya MGTU "MAMI"*. 2011;12(2):123–127. (In Russ.).

    Еремеева Ж.В., Ниткин Н.М., Шарипзянова Г.Х. Особенности применения наноразмерных порошков углерода и хрома на процессы подготовки шихты и прессования порошковых сталей. *Известия МГТУ «МАМИ»*. 2011;12(2):123–127.

Information about the Authors

Maxim S. Egorov – Cand. Sci. (Eng.), Associate Professor, Head of the Department of Materials Science and Metal Technology, Don State Technical University (DSTU)
ORCID: 0000-0002-4289-1601
E-mail: aquavdonsk@mail.ru

Rimma V. Egorova – Cand. Sci. (Eng.), Associate Professor, Department of Cybersecurity of Information Systems of DSTU
ORCID: 0000-0002-1082-3970
E-mail: rimmaruminskaya@gmail.com

Andrey V. Mozgovoy – Cand. Sci. (Eng.), Associate Professor, Vice-Rector of Strategic and Digital Development of DSTU
E-mail: amozgovoy@donstu.ru

Kirill V. Gantimurov – Graduate Student of DSTU
ORCID: 0009-0000-6913-6510
E-mail: gantimkir@ya.ru

Mark V. Kovtun – Head of the Department of Road Troops of the Military Training Center of DSTU
ORCID: 0000-0002-1082-2730
E-mail: Mk222200@yandex.ru

Сведения об авторах

Максим Сергеевич Егоров – к.т.н., доцент, заведующий кафедрой «Материаловедение и технологии металлов» Донского государственного технического университета (ДГТУ)
ORCID: 0000-0002-4289-1601
E-mail: aquavdonsk@mail.ru

Римма Викторовна Егорова – к.т.н., доцент кафедры «Кибербезопасность информационных систем» ДГТУ
ORCID: 0000-0002-1082-3970
E-mail: rimmaruminskaya@gmail.com

Андрей Владимирович Мозговой – к.т.н., доцент, проректор по стратегическому и цифровому развитию ДГТУ
E-mail: amozgovoy@donstu.ru

Кирилл Викторович Гантимуров – аспирант ДГТУ
ORCID: 0009-0000-6913-6510
E-mail: gantimkir@ya.ru

Марк Валерьевич Ковтун – начальник кафедры «Дорожные войска» Военного учебного центра ДГТУ
ORCID: 0000-0002-1082-2730
E-mail: Mk222200@yandex.ru

Contribution of the Authors

M. S. Egorov – defined the research objectives, participated in the discussion of results, and wrote the article.
R. V. Egorova – conducted the experiments and participated in the discussion of results.
A. V. Mozgovoy – participated in the discussion of results and contributed to writing the article.
K. V. Gantimurov – prepared the initial samples and conducted the experiments.
M. V. Kovtun – prepared the initial samples and conducted the experiments.

Вклад авторов

М. С. Егоров – определение цели работы, участие в обсуждении результатов, написание статьи.
Р. В. Егорова – проведение экспериментов, участие в обсуждении результатов.
А. В. Мозговой – участие в обсуждении результатов, написание статьи.
К. В. Гантимуров – приготовление исходных образцов, проведение экспериментов.
М. В. Ковтун – приготовление исходных образцов, проведение экспериментов.

Received 13.11.2024
Revised 03.12.2024
Accepted 05.12.2024

Статья поступила 13.11.2024 г.
Доработана 03.12.2024 г.
Принята к публикации 05.12.2024 г.

Theory and Processes of Formation and Sintering of Powder Materials
Теория и процессы формования и спекания порошковых материалов

UDC 621.762 : 669.701
https://doi.org/10.17073/1997-308X-2025-1-23-29

Research article
Научная статья

Evaluation of the stress state in a cold-pressed seal briquette for a gas compressor unit

A. A. Jafarova

Azerbaijan Technical University
25 H. Javid Prosp., Baku, AZ 1073, Azerbaijan

afetceferova8@gmail.com

Abstract. The finite element method is employed to analyze the distribution of residual stresses in axisymmetric preforms of a gas compressor seal at the final stage of compaction. A computational scheme is presented, based on the obtained data on equivalent stress isolines. The dependence of the stress-strain state on the contact conditions between the compact and the die during pressing is examined. The obtained data illustrate equivalent stress isolines (MPa) according to the Mirolyubov criterion. It was established that in various sections, the stress state approaches the critical limit, which may lead to visible fracture of the briquette and delamination of its lateral surface. This finding confirms the results of previous studies on obtaining high-density powder compacts via single-step cold pressing. When solving the problem of producing a high-density powder component, the initial input data included a previously known stress distribution in the compacted briquette. Such data can be obtained from widely established methodologies, particularly for cold pressing in rigid dies for components with complex geometries. The stress-strain state of the powder briquette was computed at the contact surface between the compact and the rigid die under high and infinite friction conditions. In certain regions, significant stress levels can provoke hidden or visible failure, such as rupture of the "terminal layer" or delamination of the lateral surface. The results of numerical investigations are also applicable to low-modulus powder materials compacted in massive dies. The described method for calculating residual stresses was developed using a specialized IBM software program and was utilized for stress state analysis of compacted preforms under elastic unloading conditions.

Keywords: cold pressing, residual stress, stress-strain state, finite element method, computational scheme, seal, die, powder material

Acknowledgements: This work was supported by the Azerbaijan Science Foundation-Grant № AEF-MCG-2024-2(50)-16/01-M-01.

For citation: Jafarova A.A. Evaluation of the stress state in a cold-pressed seal briquette for a gas compressor unit. *Powder Metallurgy and Functional Coatings*. 2025;19(1):23–29. https://doi.org/10.17073/1997-308X-2025-1-23-29

Оценка напряженного состояния холоднопрессованного брикета уплотнителя для газокомпрессорной установки

А. А. Джафарова

Азербайджанский технический университет
Азербайджан, AZ 1073, г. Баку, пр. Г. Джавида, 25

afetceferova8@gmail.com

Аннотация. Методом конечных элементов анализируется распределение остаточных напряжений в осесимметричных заготовках уплотнителя газокомпрессорной установки к концу прессования. Представлена схема расчета, основанная на полученной информации по изолиниям эквивалентных напряжений. Дается зависимость напряженно-деформированного состояния от контактных условий прессовки с матрицей. На основании полученной информации показаны изолинии экви-

валентных напряжений (МПа) по критерию Миролюбова. Установлено, что на разных участках напряженное состояние близко к предельному и может привести к видимому разрушению брикета и расслоению его боковой поверхности. Это подтверждает результаты работ по получению высокоплотных порошковых прессовок путем однократного холодного прессования. При решении задачи получения высокоплотной порошковой детали вводной информацией являлось известное распределение напряжений в уплотненном брикете. Такие данные возможно получить из некоторых широко представленных методик, особенно для состояния холодного прессования в твердых матрицах деталей сложной конфигурации. Произведен расчет напряженно-деформированного состояния порошкового брикета на контактной поверхности прессовки с твердой матрицей для высокого и безграничного трений. На некоторых участках значительное напряженное состояние способно спровоцировать скрытое или видимое разрушение, например разрыв «конечного слоя» или же расслоение боковой поверхности. Результаты численных исследований приемлемы и для низкомодульных порошковых материалов, спрессованных в массивных матрицах. Описанная методика расчета остаточных напряжений была разработана специальной программой в IBM и была использована при проведении исследований напряженного состояния прессуемых заготовок в условиях упругой разгрузки.

Ключевые слова: холодное прессование, остаточное напряжение, напряженно-деформированное состояние, метод конечных элементов, схема расчета, уплотнитель, матрица, порошковый материал

Благодарности: Работа выполнена при финансовой поддержке Фонда науки Азербайджана – грант № AEF-MGC-2024-2(50)-16/01/1-M -01.

Для цитирования: Джафарова А.А. Оценка напряженного состояния холоднопрессованного брикета уплотнителя для газокомпрессорной установки. *Известия вузов. Порошковая металлургия и функциональные покрытия*. 2025;19(1):23–29. https://doi.org/10.17073/1997-308X-2025-1-23-29

Introduction

The production of parts and semi-finished products from metal and other powders in a closed mold through cold pressing of unsintered briquettes is accompanied by the formation of significant technological stresses. After the upper pressing punch is removed, the briquette in the die undergoes elastic “expansion” , which primarily occurs due to a sudden change in the stress-strain state of the “green” compact. As is well known, such tensile stresses can lead to the failure of an entire region or the upper layer of the compact [1; 2]. Based on literature data, it can be noted that the elastic spring-back behavior in pressed parts remains insufficiently studied [1–3]. In this regard, considering the aforementioned phenomenon, the development of a methodology for calculating the stress-strain state of compacted products is a relevant problem for predicting their strength. The quality of sintering is determined at the stage of the “green” compact, depending on various temperature regimes of cold pressing and heating conditions. Studies [4–6] have shown that during high-pressure compaction of iron-based mixtures, gas (air) evacuation from the compacted briquette becomes difficult.

The main objective of this study was to analyze the distribution of residual stresses at the final stage of cold pressing in axisymmetric powder preforms of a gas compressor seal.

Residual stress evaluation

The distribution of residual stresses in axisymmetric compacts of the seal was analyzed using the finite element method after punch removal. The analytical approach is significantly complicated by the physical nonlinearity of this problem. The proposed algorithm considers the stress state of the compact at the final stage of densification, along with the elastic relaxation of contact (including force and kinematic factors) and other conditions in the compacted briquettes. High tensile pressures arise, which, upon release of the compact from the die, lead to significant loosening and even fracture of the briquette. Therefore, in [7], a device and method were proposed to enhance air drainage from the pressing zone during high-pressure compaction of a powder mixture. Accordingly, obtaining high-density powder products requires knowledge of residual stress levels in different regions of the compact. This information serves as the basis for constructing a further technological chain for manufacturing high-density powder products of complex geometry.

During the elastic relaxation process, the stress state of the compact was determined by formulating a finite element problem using the finite element method, which includes:

– the variational Lagrange equation [8–10]:

$$\int_V \delta\{\varepsilon\}^T\{\sigma\}dv - \int_{S_f}\delta\{u\}^T_{S_f}\{F\}_f dS_f = 0; \qquad (1)$$

– the material equation accounting for initial stresses:

$$\{\sigma\} = \begin{vmatrix}\sigma_\varphi\\ \sigma_T\\ \sigma_z\\ \tau_{rz}\end{vmatrix} = [B]\{\varepsilon\} + \{\sigma^0\}, \qquad (2)$$

$$\{\varepsilon\} = \begin{vmatrix} \varepsilon_\varphi \\ \varepsilon_r \\ \varepsilon_z \\ \gamma_{rz} \end{vmatrix} = [L]\{u\}, \qquad (3)$$

where $[L] = \begin{vmatrix} \frac{1}{r} & 0 \\ \frac{\partial}{\partial r} & 0 \\ 0 & \frac{\partial}{\partial z} \\ \frac{\partial}{\partial z} & \frac{\partial}{\partial r} \end{vmatrix}$ is the differential operator;

– the displacement approximation equation within the element nodes is given by:

$$\{u\} = \begin{Bmatrix} u_r \\ u_z \end{Bmatrix} = [N]\{x\} = [N]\begin{Bmatrix} x_i \\ x_j \\ x_R \end{Bmatrix}; \qquad (4)$$

– the contact conditions in the "compact–die" system, considering frictional forces at the contact surface:

$$\{F\}_f = f\{\sigma_n\}S_f. \qquad (5)$$

The kinematic problem (contact condition), which refers to the necessary unilateral boundary conditions, is taken into account in the analysis and model construction [11]. For a rigid die, these conditions can be formulated as "impermeability conditions":

$$\begin{aligned} \{u_r\}_{r=R} &= 0 \ldots \{\sigma_r\}_{r=R} < 0, \\ \{u_z\}_{z=0} &= 0 \ldots \{\sigma_z\}_{z=0} < 0; \end{aligned} \qquad (6)$$

$$\begin{aligned} \{u_r\}_{r=R} &< 0 \ldots \{\sigma_r\}_{r=R} > 0, \\ \{u_z\}_{z=0} &> 0 \ldots \{\sigma_z\}_{z=0} > 0. \end{aligned} \qquad (7)$$

In equations (1)–(7), the parameters are defined as follows: $\{\sigma\}$, $\{\varepsilon\}$ – tensors of residual stresses and strains, respectively; $\{\sigma^0\}$ – stress tensor in the compact at the final moment of densification; $\{u\}_{S_f}$ – displacement vector of the element nodes on the friction surface (between the compact and the die at initial and final moments); $[B]$, $[N]$ – the elastic constant matrix of the compact material and the shape function of the finite element, determined based on [12]; $\{F\}_f$ – friction force acting on the uniform contact surface; $\{x\}$ – displacement vector of the finite element nodes; f – friction coefficient; $\{\sigma_n\}S_f$ – normal stresses at the "compact–die" contact surface; x, T, δ – operators of multiplication, transposition, and variation, respectively.

Considering equations (2)–(4), equation (1) can be rewritten in the standard form for the finite element method:

$$[K]\{x\} = \{R\}_{\sigma^0} + \{R\}_f, \qquad (8)$$

where $[K]$ is the global stiffness matrix [11]; $\{R\}_{\sigma^0} = \int [B]^T \{\sigma^0\} dv$ is the nodal force vector arising from the presence of stresses $\{\sigma^0\}$ in the compact; $[B] = [L][N]$; $\{R\}_f = \int_{S_f} [N]^T \{F\}_f dS_f$ is the nodal forces dependent on frictional forces.

Thus, the problem formulated in equations (1)–(7) is reduced to solving the system of linear algebraic equations (8), considering the displacement of finite element nodes [13].

However, due to the uncertainty of vector $\{R\}_f$, the problem is generally nonlinear. Therefore, an iterative method is proposed, based on sequential solutions of classical elasticity theory with friction force corrections and validation of constraints (6) and (7) at a specific stage.

At the first step, the nodal force vector $\{R\}_{\sigma^0}$ and the friction force $\{R\}_f$ are applied to the element nodes, using the normal stress distribution in the zone $\{\sigma^0\}$. Solving equation (8) yields the components $\{x\}$, $\{\sigma\}$, $\{g\}$ of the stress-strain state of the compact, corresponding to the removal of the upper punch under the influence of frictional forces initially acting on the briquette surface [14]. By adjusting the friction force vector $\{\sigma\}_1$ to match the updated normal stresses, the procedure is repeated until the desired accuracy is achieved. Furthermore, as numerical experiment indicates, it is advisable to verify connectivity conditions, while the "impermeability" conditions (6) and (7) remain satisfied throughout the solution process. Ultimately, after removing the externally applied pressing forces from the initial stress state $\{\sigma^0\}$, the residual stress distribution and strain state of the compact are obtained [15].

In solving the stated problem, the input data consisted of a previously known stress distribution in the compacted briquette. Such data can be obtained from several widely established methodologies, particularly for cold pressing in rigid dies [16; 17]. A similar approach was applied in our study.

For example, for $H_0/D = 1.5$, where H_0 is the height of the compressed cylinder and D is its diameter (Fig. 1), the stress-strain state of a proportionally cylindrical seal for a gas compressor unit was investigated [18]. The semi-finished product was obtained

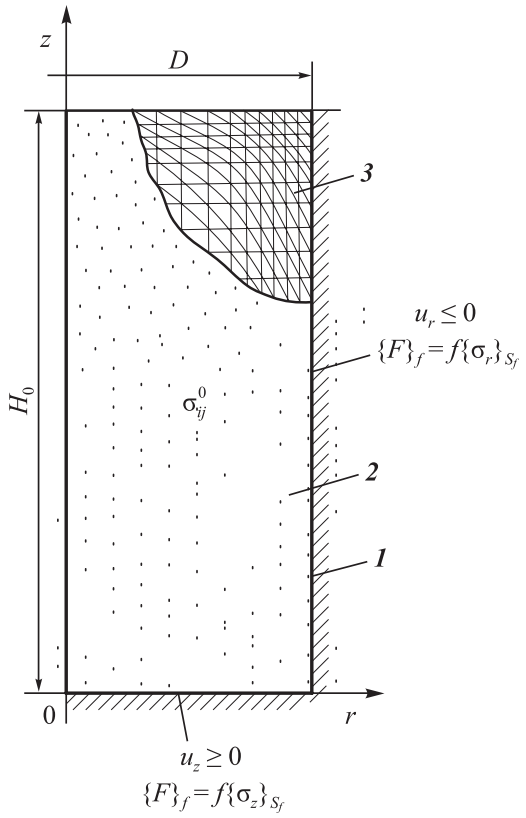

Fig. 1. Calculation scheme
1 – rigid die, ***2*** – compact, ***3*** – mesh

Рис. 1. Схема расчета
1 – жесткая матрица, ***2*** – прессовка, ***3*** – сетка

by pressing an iron-based composite powder containing 2 wt. % graphite powder under a maximum pressure of $P = 1000$ using a punch.

The friction coefficient was determined from the following relationship

$$f = A + B\sigma_0^c, \qquad (9)$$

where A and B are material constants, and σ_0^c is the mean pressure in the elements of the contact layer.

In the calculations, the average values of the material's elastic constants were used for the entire volume of the compact: Young's modulus $E = 4$ GPa and Poisson's ratio $\nu = 0{,}4$.

The discretization of the axisymmetric preform was performed using circular elements of triangular cross-section. The finite element mesh was refined in regions with the highest stress concentrations, specifically on the lateral surface and the free end of the compact [19].

A stress-strain state analysis was conducted for different force conditions at the "compact–rigid die" contact interface (Fig. 2, *a*, *b*): for high-friction conditions, where the axial displacement of points on the compact's contact surface was restricted, i.e. $\{u_x\}_{S_f} = 0$ and for friction defined by equation (5), where $\{u_x\}_{S_f}$ is infinite.

Fig. 2 illustrates the "natural" shape of the preform after unloading. The dashed lines represent certain sections of the compact before unloading, while the dotted lines indicate the positions of the finite element nodes of the same sections after punch removal.

The calculations show that stress redistribution is often accompanied by the development of internal tensile stresses [20]. For example, in the zone *I* elements, we have $\sigma_1 > 0$, while in the shaded zone *II* – $\sigma_1 > 0$, $\sigma_0 > 0$, (see Fig. 2, *a*), where σ_1 is the highest stress in the *rz*-plane, and σ_0 is the mean normal stress (*I* – compression zone).

In the elements of the surface layer, both radial stress (σ_T) and circumferential stress (σ_φ) were positive. Curves *1*, *2* in Fig. 2 represent variations in these stresses along the free end surface of the seal. The stress state of the briquette is characterized by a well-developed $\sigma_1 > 0$ zone under unloading conditions close to real scenarios, by stress concentration $\sigma_1 > 0$, $\sigma_0 > 0$, in the closed "corners" of the compact, and by the occurrence of tensile stresses σ_φ in the lateral layer of the open end (Fig. 2, *c*).

To assess the strength of the compact after elastic unloading, the Mirolyubov criterion is used in the following form [21]:

$$\sigma_e = \frac{3(1-\lambda)}{2}\sigma_0 + \frac{1+\lambda}{2}\sigma_i, \qquad (10)$$

where σ_i is the stress intensity, and $\lambda = \sigma_d^p / \sigma_d^s$, σ_d^s are the boundary stresses under simple tension and compression conditions.

Fig. 3 shows the distribution of residual equivalent stresses σ_e under unloading conditions at $\lambda = 0.15$ [22]. The highest stress concentration in the compact occurs in the bottom volume after punch removal: tensile stresses develop in the wall layers, while compressive stresses dominate in the central region.

In these regions, the stress state is close to the critical limit and may lead to either hidden or visible failure, such as rupture of the "terminal layer" or delamination of the lateral surface [23].

It should be noted that the results of the numerical investigations are also applicable to low-modulus powder materials compacted in massive dies.

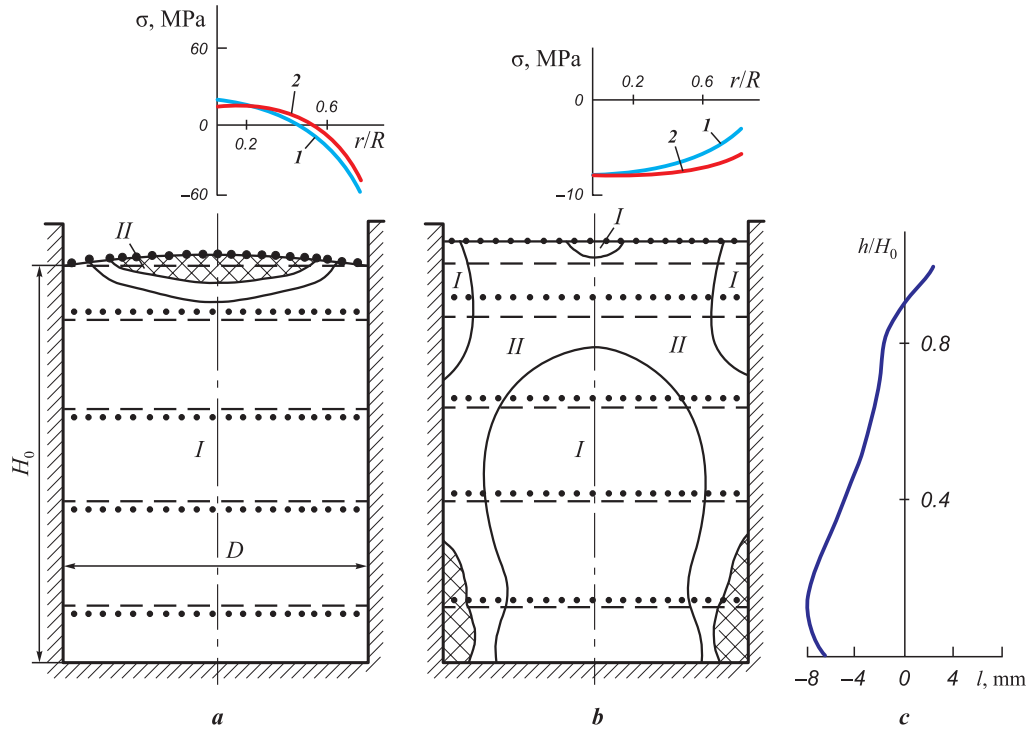

Fig. 2. Dependence of the stress-strain state of the compact on contact conditions with the die

a – natural shape of the preform after unloading; ***b*** – stress variation on the surface of the free end of the preform;
c – tensile stresses in the lateral layer of the free end
I – compression zone, ***II*** – stress-free zone
1, ***2*** – variation of radial and circumferential stresses
h/H_0 – ratio of the final briquette height to its initial height

Рис. 2. Зависимость напряженно-деформированного состояния прессовки с матрицей от контактных условий

a – натуральная форма заготовки после разгрузки; ***b*** – изменение напряжений на поверхности свободного торца заготовки;
c – растягивающие напряжения в боковом слое свободного торца
I – зона сжатия, ***II*** – зона, свободная от напряжений
1, ***2*** – изменение радиального и окружного напряжений
h/H_0 – отношение конечной высоты брикета к первоначальной

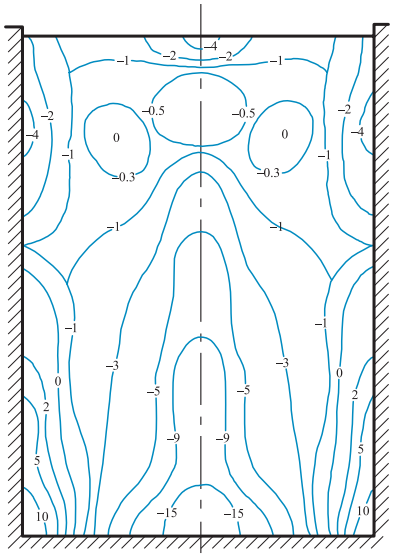

Fig. 3. Isolines of equivalent stresses according to the Mirolyubov criterion

Рис. 3. Изолинии эквивалентных напряжений по критерию Миролюбова

Conclusion

The finite element analysis established the stress-strain state of the compact at the final stage of cold pressing. This problem was reduced to solving a system of linear algebraic equations while accounting for the displacement of finite element nodes. It was revealed that the highest stress concentration in the compact occurs in the bottom volume after punch removal, with tensile stresses in the wall layers and compressive stresses in the central part of the compact.

References / Список литературы

1. Griqoriev S.N., Dmitriev A.M., Korobova N.V., Fedorov S.V. A cold-pressing method combining axial and shear flow of powder compaction to produce high-density iron parts. *Technologies*. 2019;7(4):70. https://doi.org/10.3390/technologies7040070
2. Dmitriev A.M., Korobova N.V., Badalyan A.Z. Development and research of formation technologies on specialized presses with subsequent sintering of high-den-

sity details from iron-based powders. *Journal of Mining Institute*. 2019;236:216–228. https://doi.org/10.31897/PMI.2019.2.216

Дмитриев А.М., Коробова Н.В., Бадалян А.Ж. Разработка и исследование технологии формования на специализированных прессах с последующим спеканием высокоплотных деталей из порошков на железной основе. *Записки Горного института*. 2019;236:216–228. https://doi.org/10.31897/PMI.2019.2.216

3. Ferreira S.C., Conde A., Arenas M.A., Rocha L.A., Velhinho A. Anodization mechanism on SiC nanoparticle reinforced al matrix composites produced by power metallurgy. *Materials*. 2014;7(12):8151–8167. https://doi.org/10.3390/ma7128151
4. Chauhan S., Verma V., Prakash U., Tewari P.C., Khanduja D. Studies on induction hardening of powder-metallurgy-processed Fe–Cr/Mo alloys. *International Journal of Minerals Metallurgy and Materials*. 2017; 24(8):918–925. https://doi.org/10.1007/s12613-017-1478-2
5. Mamedov A.T., Mamedov V.A. Phenomenological approach to the plastic deformation of metallic powders in confined cavity. *News of ANAS: Science and Innovation Series*. 2012;1(9):67–72.
6. Dmitriev A.M., Korobova N.V. A study of advanced processes for large-scale production of parts from powder steels. *Metal Science and Heat Treatment*. 2018; 60(7):457–463. https://doi.org/10.1007/s11041-018-0301-7

Дмитриев А.М., Коробова Н.В. Исследование перспективных технологий для крупносерийного производства деталей из порошковых сталей. *Металловедение и термическая обработка металлов*. 2018; (7(757)):46–53.

7. Jafarova A.A. Compaction of elastoplastic iron batch in pressing. *Russian Engineering Research*. 2023;43(9): 1095–1100. https://doi.org/10.3103/S1068798X23090101
8. Montes J.M., Cuevas F.G., Cintas J., Torres Y. Powder compaction law for cold die pressing. *Journal Granular Matter*. 2010;12(6):617–627. https://doi.org/10.1007/s10035-010-0203-x
9. Xu C., Liu F., Huang L., Jiang L. Dependence of creep performance and microstructure evolution on solution cooling rate in a polycrystalline superalloy. *Metals*. 2018;8(1):4. https://doi.org/10.3390/met8010004
10. Mammadov A., Mammadov V. Comparative analysis of diffusion metallization coatings applied on steel parts. *Metallurgical and Materials Engineering*. 2023; 29(4):43–54. https://doi.org/10.56801/MME1020
11. Justino J.G., Alves M.K., Klein A.N., Al-Qureshi H.A. Constutive model for the elastic-plastic analysis of porous sintered materials. *International Journal of Machine Tools Manufacture*. 2004;44(14):1471–1479. https://doi.org/10.1016/j.ijmachtools.2004.05.006
12. Al-Qureshi H.A., Galiotto A., Klein A.N. On the mechanics of cold die compaction for powder metallurgy. *Journal of Materials Processing Technology*. 2005;166(1):135–143. https://doi.org/10.1016/j.jmatprotec.2004.08.009
13. Mamedov A.T., Rustamova S.M. Influence of intermediate sintering temperature on the properties of powder materials. *Vestnik mashinostroeniya*. 2018;(2):48–51. (In Russ.).

Мамедов А.Т., Рустамова С.М. Влияние температуры промежуточного спекания на свойства порошковых материалов. *Вестник машиностроения*. 2018;(2):48–51.

14. Bogatov A.A. Residual stresses and metal facture. In: *Innovative technologies in metallurgy and mechanical engineering: Proceedings of the 6th Intern. youth scientific and practical conferences* (Ekaterinburg, 29 October – 1 November, 2012). Ekaterinburg: Publ. Ural. University, 2013. P. 95–101. (In Russ.). https://elar.urfu.ru/handle/10995/33248

Богатов А.А. Остаточные напряжения и разрушение металла. В сб.: *Инновационные технологии в металлургии и машиностроении: Материалы 6-й Междунар. молодежной науч.-практ. конференции* (г. Екатеринбург, 29 октября – 1 ноября 2012 г.). Екатеринбург: Изд-во Урал. ун-та, 2013. С. 95–101. https://elar.urfu.ru/handle/10995/33248

15. Gnuchii Yu.B. To the solution of contact problems of the theory of elasticity and plasticity. *Problemy prochnosti*. 2012;(12):99–104. (In Russ.).

Гнучий Ю.Б. К решению контактных задач теории упругости и пластичности. *Проблемы прочности*. 2012;(12):99–104.

16. Generalov M.B., Stepanova A.R. Study of the compaction process of powder materials in a blind matrix. BMSTU *Journal of Mechanical Engineering*. 1988;(11):110–114. (In Russ.).

Генералов М.Б., Степанова А.Р. Исследование процесса уплотнения порошковых материалов в глухой матрице. *Известия вузов. Машиностроение*. 1988; (11):110–114.

17. Radomyselsky I.D., Pechentkovsky E.L. Influence of the pressing tool on the density distribution in metal-ceramic materials such as bushings. *Powder Metallurgy*. 1970;(4):13–19. (In Russ.).

Радомысельский И.Д., Печентковский Е.Л. Влияние прессующего инструмента на распределение плотности в металлокерамических материалах типа втулок. *Порошковая металлургия*. 1970;(4):13–19.

18. Dvilis E.S., Chartpuk P., Khasanov O.L., Sokolov V.M., Eshetov B.A. Analytical and model optimization of kinematic schemes of uniformly dense pressing of powder materials. *Bulletin of the Tomsk Polytechnic University*. 2013;323(2):49–55. (In Russ.).

Двилис Э.С., Чартпук П., Хасанов О.Л., Соколов В.М., Ешетов Б.А. Аналитическая и модельная оптимизация кинематических схем равномерноплотного прессования порошковых материалов. *Известия Томского политехнического университета*. 2013;323(2):49–55.

19. Koshlyakov N.S., Gliner E.B., Smirnov M.M. Partial differential equations of mathematical physics. Moscow: Vysshaya Shkola, 1970, 710 p. (In Russ.).

Кошляков Н.С., Глинер Э.Б., Смирнов М.М. Уравнения в частных производных математической физики. М.: Высшая школа, 1970, 710 с.

20. Zenkevich O.K. Finite element method in technology. Moscow: Mir, 1975. P. 426–428. (In Russ.).

Зенкевич О.К. Метод конечных элементов в технике. М.: Мир, 1975. С. 426–428.

21. Pozdnev A.A., Nyashin Yu.I., Trusov V.P. Residual stresses: theory and applications. Moscow: Nauka, 1982. P. 94–97. (In Russ.).

Позднев А.А., Няшин Ю.И., Трусов В.П. Остаточные напряжения: теория и приложения. М.: Наука, 1982. С. 94–97.

22. Moskvitin V.V. Resistance of viscoelastic materials. Moscow: Nauka, 2002. P. 76–79. (In Russ.).

Москвитин В.В. Сопротивление вязкоупругих материалов. М.: Наука, 2002. С. 76–79.

23. Kalinnikov A.E., Vakhrushev A.V., Kurguzkin M.G. Durability and creep of a multi-resistance composite under plane stress conditions. In: *Abstracts of the 5th All-Union Conference on mechanics of polymer and composite materials*. Riga: Zinatne, 2003. P. 77–80. (In Russ.).

Калинников А.Е., Вахрушев А.В., Кургузкин М.Г. Долговечность и ползучесть разносопротивляющегося композита в условиях плоского напряженного состояния. В сб.: *Тезисы докладов V Всесоюз. конференции по механике полимерных и композитных материалов*. Рига: Зинатне, 2003. С. 77–80.

Information about the Author

Afet Arif Jafarova – Cand. Sci. (Eng.), Associate Professor of the Department "Chemical technology, processing and ecology" of the Azerbaijan Technical University
ORCID: 0000-0003-4842-8906
E-mail: afetceferova8@gmail.com

Сведения об авторе

Афет Ариф кызы Джафарова – к.т.н., доцент кафедры «Химическая технология, переработка и экология» Азербайджанского технического университета
ORCID: 0000-0003-4842-8906
E-mail: afetceferova8@gmail.com

Received 15.08.2024
Revised 06.01.2025
Accepted 09.01.2025

Статья поступила 15.08.2024 г.
Доработана 06.01.2025 г.
Принята к публикации 09.01.2025 г.

Refractory, Ceramic, and Composite Materials
Тугоплавкие, керамические и композиционные материалы

UDC 661.66
https://doi.org/10.17073/1997-308X-2025-1-30-39

Research article
Научная статья

Crystalline structure of polyacrylonitrile- and viscose-based carbon fibers following high-temperature treatment in the range of 1500–2800 °C

B. S. Kleusov[1], V. M. Samoilov[1], V. A. Elchaninova[1], D. A. Budushin[1], E. M. Litovchenko[2], A. S. Poplavskaya[1], V. A. Vorontsov[1]

[1] **JSC "Scientific Research Institute of Structural Materials based on graphite named after S.E. Vyatkin"**
1 Bld, 2 Electrodnaya Str., Moscow 111524, Russia
[2] **D.I. Mendeleev Russian University of Chemical Technology**
1 Bld, 20 Geroev Panfilovtsev Str., Moscow 125480, Russia

BSKleusov@rosatom.ru

Abstract. The crystalline structure of carbon fibers (CF) based on polyacrylonitrile (PAN) and viscose precursors, treated in the temperature range of 1500 to 2800 °C, was studied using *X*-ray diffraction analysis and Raman spectroscopy. The objective of the study was to obtain data on the structure of low-modulus viscose-based fibers, which are widely used as fillers in composite materials, and to compare the characteristics of CF derived from different precursors. An empirical dependence of the intensity ratio of the *D* and *G* lines (I_D/I_G) of the Raman spectra on the treatment temperature was established for carbon fibers based on viscose and PAN. The crystallite sizes L_a and L_c of both types of CF obtained at different treatment temperatures were evaluated. It was revealed that as the treatment temperature increases, the crystallite sizes L_a and L_c grow, while the interlayer spacing d_{002} decreases, indicating an increase in the degree of graphitization. It was found that viscose-based carbon fibers exhibit a less ordered crystalline structure compared to PAN fibers processed under the same conditions. Additionally, the true density and elastic modulus of viscose-based CF were investigated, showing lower values than those of PAN fibers treated at the same temperature. These differences in the properties and structure of CF are attributed to the microtextured nature of viscose fibers. However, during treatment at 2800 °C, CF undergo partial graphitization, which significantly reduces structural differences between fibers of both types. Nevertheless, despite the similarity in crystalline structure, viscose-based CF, even after high-temperature treatment, does not become analogous to PAN-based fibers.

Keywords: carbon fibers, *X*-ray phase analysis, Raman spectroscopy

For citation: Kleusov B.S., Samoilov V.M., Elchaninova V.A., Budushin D.A., Litovchenko E.M., Poplavskaya A.S., Vorontsov V.A. Crystalline structure of polyacrylonitrile- and viscose-based carbon fibers following high-temperature treatment in the range of 1500–2800 °C. *Powder Metallurgy and Functional Coatings*. 2025;19(1):30–39.
https://doi.org/10.17073/1997-308X-2025-1-30-39

Кристаллическая структура углеродных волокон на основе полиакрилонитрила и вискозы после высокотемпературной обработки в интервале температур 1500–2800 °C

Б. С. Клеусов[1], В. М. Самойлов[1], В. А. Ельчанинова[1], Д. А. Будушин[1], Е. М. Литовченко[2], А. С. Поплавская[1], В. А. Воронцов[1]

[1] **АО «Научно-исследовательский институт конструкционных материалов на основе графита» им. С.Е. Вяткина**
Россия, 111524, г. Москва, ул. Электродная, 2, стр. 1
[2] **Российский химико-технологический университет им. Д.И. Менделеева**
Россия, 125480, г. Москва, ул. Героев Панфиловцев, 20, корп. 1, стр. 2

BSKleusov@rosatom.ru

Аннотация. Методами рентгеновского дифракционного анализа и спектроскопии комбинационного рассеяния проведено исследование кристаллической структуры углеродных волокон (УВ) на основе полиакрилонитрила (ПАН) и вискозы, обработанных в диапазоне температур от 1500 до 2800 °C. Целью исследования было получение данных о структуре низкомодульных волокон на основе вискозы, имеющих широкое применение в качестве наполнителей композиционных материалов, а также сравнение характеристик УВ на основе разных прекурсоров. Получена эмпирическая зависимость отношения интенсивностей линий D и G (I_D/I_G) спектров комбинационного рассеяния от температуры обработки для углеродных волокон на основе вискозы и ПАН. Проведена оценка размеров кристаллитов (L_a и L_c) обоих типов УВ, полученных при различных температурах обработки. Выявлено, что с ростом температуры обработки волокон происходит увеличение размеров кристаллитов L_a и L_c, а межслоевое расстояние (d_{002}) уменьшается, что указывает на повышение степени графитации. Установлено, что углеродные волокна на основе вискозы имеют менее совершенную кристаллическую структуру по сравнению с ПАН-волокнами, обработанными в тех же условиях. Также были исследованы истинная плотность и модуль упругости УВ на основе вискозы, у которых оказались более низкие значения, чем у ПАН-волокон с той же температурой обработки. Данные различия в свойствах и структуре УВ обусловлены микротекстурированностью вискозного волокна. Однако в процессе обработки при температуре 2800 °C УВ претерпевают частичную графитацию, что в значительной степени нивелирует структурные различия между волокнами обоих видов. Тем не менее, несмотря на сходство кристаллической структуры, УВ на основе вискозы даже после высокотемпературной обработки не становятся аналогом ПАН-волокна.

Ключевые слова: углеродные волокна, рентгенофазовый анализ, рамановская спектроскопия

Для цитирования: Клеусов Б.С., Самойлов В.М., Ельчанинова В.А., Будушин Д.А., Литовченко Е.М., Поплавская А.С., Воронцов В.А. Кристаллическая структура углеродных волокон на основе полиакрилонитрила и вискозы после высокотемпературной обработки в интервале температур 1500–2800 °C. *Известия вузов. Порошковая металлургия и функциональные покрытия*. 2025;19(1):30–39. https://doi.org/10.17073/1997-308X-2025-1-30-39

Introduction

The development of carbon fiber-reinforced plastics has led to the production of a wide range of carbon fibers (CF) [1–6]. The existing classification divides all CF into several types based on their modulus: low-modulus (30–100 GPa), intermediate-modulus and high-strength (200–350 GPa), high-modulus (350–500 GPa), and ultra-high-modulus (500–1000 GPa) [6–11]. Another critical factor in classifying fibers is the precursor type, which determines the crystalline structure of CF and, ultimately, its final properties [6–11]. Currently, nearly all commercially produced CF are derived from three main precursors: polyacrylonitrile (PAN), isotropic and mesophase pitches, and viscose [6–11].

The crystalline structure of PAN- and mesophase pitch-based CF has been extensively studied using *X*-ray diffraction, often in combination with Raman spectroscopy and electron microscopy [12–17]. However, the structure of viscose-based fibers remains underexplored. Existing data in early literature [18; 19] pertain to the technology for producing intermediate- and high-modulus viscose-based CF, developed over 50 years ago in the United States. Studies on the crystalline structure of low-modulus (30–100 GPa) viscose-based CF are extremely limited [20–22], despite their widespread use as fillers in composite materials for various applications.

The aim of this study was to investigate the crystalline structure of viscose-based carbon fibers and its

changes during high-temperature treatment, with a comparative analysis of similar data for PAN-based CF.

Materials and methods

For this study, semi-finished products of TGN-brand viscose-based CFs and UKN-type PAN-based CFs, both manufactured in the Russian Federation, were used. The samples were obtained by additional heat treatment (HT) of CF bundles in a laboratory Tammann furnace under argon atmosphere in a free state (without tension). The heating rate was 300 °C/h, and the dwell time at the target temperature was 20 min. The processing temperature was monitored using a pyrometer.

The true density of the obtained CF samples was measured using the gradient tube method in accordance with GOST R ISO 10119–2012. The average filament diameter, tensile strength, and dynamic elastic modulus of single filaments were measured according to ASTM D4018–11. The physical and mechanical properties of CF were determined as averages from 25 measurements of tensile strength and elastic modulus, following GOST 6943.5–79 and GOST 28008–88.

Raman spectra of CF subjected to various HT temperatures (t_{HT}) were recorded from the lateral surface of filaments in the broad spectral range of 700–3000 cm^{-1} using a confocal Raman microspectrometer Via Reflex (Renishaw, UK) equipped with an optical microscope and a cooled CCD detector. The laser spot size at 100× magnification was 0.5 μm. The excitation source was a diode-pumped solid-state Nd:YAG laser with a wavelength of 532 nm and a power of 1 mW.

In the first-order spectrum (1000–2000 cm^{-1}), carbon materials, including CF, typically exhibit two characteristic bands [30; 31; 34]. One is the band at $\nu = 1580$ cm^{-1}, allowed by Raman scattering and corresponding to the ideal graphitic vibrational mode with E_{2g} symmetry, often referred to as the *G* mode [23–27]. It is associated with in-plane vibrations of carbon atoms in graphene layers and relates to carbon atoms in an sp^2-hybridized state. The other band, at $\nu = 1360$ cm^{-1}, is due to disordered carbon atoms, corresponds to lattice vibrations with A_{1g} symmetry, and is called the *D* mode [23–27]. This mode is linked to carbon atoms in sp^2- and sp^3 hybridization states, typically localized at defects or the edges of graphene layers [23–27]. The *D* band is absent in monocrystalline graphite, and its increasing intensity is considered indicative of a higher content of disordered or peripheral carbon [23–27]. According to numerous studies, for crystallite sizes up to 2 nm, the ratio of the integrated intensities of these bands (I_D/I_G) depends on the defect concentration and follows the Ferrari equation [28; 30–32]. For crystallite sizes larger than 2 nm, the I_D/I_G ratio is determined by the average distance between defects. In graphitizing carbon materials, it can characterize the average crystallite size (L_a) using the Tuinstra-Koenig relation [29–31]. For the studied CF, L_a was calculated using the following equation:

$$\frac{I_D}{I_G} = \frac{C(\lambda)}{L_a}, \quad (1)$$

where $C(\lambda)$ is a constant dependent on the laser wavelength. Thus, $C(\lambda = 532\ nm)$ is approximately equal to 4.4 nm [23; 24; 27].

The interpretation of the secondary 2*D* band ($\nu = 2700$ cm^{-1}) is more complex. This band appears at a sufficiently high degree of crystalline structure perfection and typically consists of several components [24; 27]. However, for the purposes of this study, only the t_{HT} (heat-treatment temperature) at which the 2*D* band appears was recorded.

X-ray phase analysis was conducted using a D8 Advance diffractometer (Bruker, Germany). A copper *X*-ray tube with a maximum power of 2200 *W* and CuK_α radiation ($\lambda = 0.15418$ nm) was used as the *X*-ray source, in Bragg–Brentano geometry (reflection mode). *X*-ray diffraction patterns were recorded over the angular range of $2\theta = 10 \div 90°$, with a scanning speed of 2°/min and a step size of 0.02°. The fibers were placed on a low-background silicon holder, evenly distributed over its surface. Before each measurement, the tube and detector were initialized. The diffraction patterns were processed using the specialized TOPAS software. The absolute error in measuring the angular positions of diffraction peaks did not exceed ±0.026° [33]. The interplanar spacing (d_{002}) was calculated based on the center of gravity of the (002) peak using the Wulff–Bragg equation:

$$d_{002} = \frac{\lambda}{2\sin\theta_{002}}, \quad (2)$$

where λ is the wavelength of the *X*-ray radiation and θ_{002} is the diffraction angle determined from the center of gravity of the (002) reflection.

The crystallite sizes were calculated using the Scherrer formula:

$$L_c = \frac{k\lambda}{\beta\cos\theta_{002}}, \quad (3)$$

where β is the full width at half maximum (FWHM) of the (002) reflection, and $k = 0.89$ [32; 33].

Results and discussion

Fig. 1 presents photographs of PAN- and viscose-based CF filaments treated at processing temperatures t_{HT} = 1200 and 2800 °C. It is evident that the microstructure of the fracture surface and the lateral surface of the filaments of the studied CF at t_{HT} = 1200 °C show minimal differences. However, the fracture surface photographs of the CF after heat treatment at 2800 °C exhibit pronounced differences.

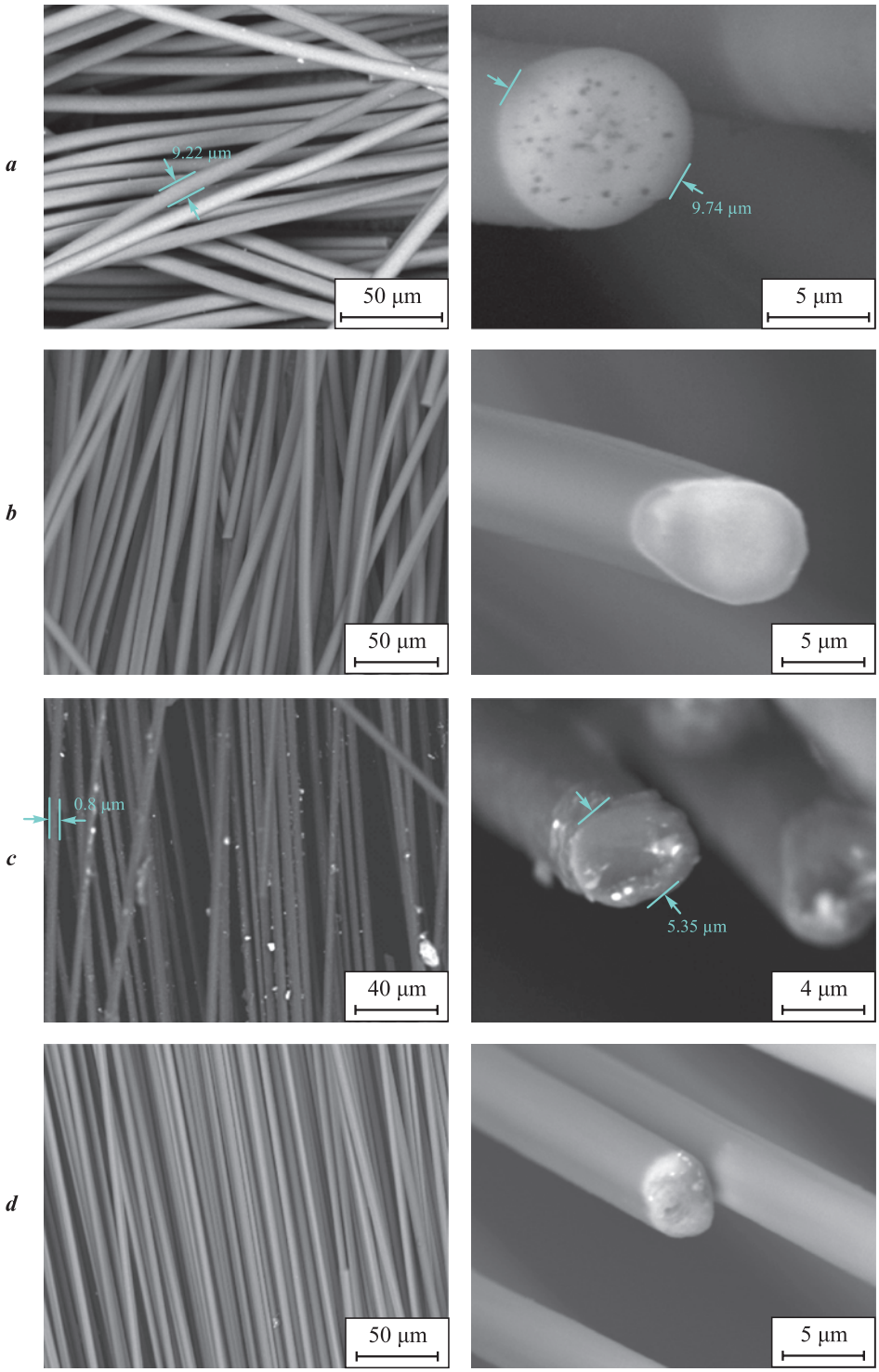

Fig. 1. Photographs of viscose-based CF (***a***, ***b***) and PAN-based CF filaments (***c***, ***d***) at t_{HT} = 1200 °C (***a***, ***c***) and 2800 °C (***b***, ***d***)

Рис. 1. Фотографии филаментов УВ на основе вискозы (***a***, ***b***) и ПАН (***c***, ***d***) $t_{ТО}$ = 1200 °C (***a***, ***c***) и 2800 °C (***b***, ***d***)

The dependencies of the true density of CF filaments (γ, g/cm^3) and the dynamic elastic modulus (E, GPa) on the processing temperature of the studied fibers are shown in Fig. 2. It can be seen that viscose-based fibers exhibit lower values of γ and E compared to PAN-based CF across the entire range of t_{HT}. Notably, the elastic modulus of viscose-based fibers is 4–5 times lower than that of PAN-based fibers throughout the temperature range.

Fig. 3 shows the X-ray diffraction patterns and Raman spectra of the studied CF with varying processing temperatures, while Fig. 4 illustrates the dependence of their crystalline structure parameters on t_{HT}.

It is evident that the increase in intensity and narrowing of the (002) diffraction line indicates an improvement in the crystalline structure with increasing t_{HT} for both viscose- and PAN-based CF (Fig. 3, *a*, *b*). The asymmetry of the diffraction peak can be effectively described by multiple structural components [34–35]; however, this study provides averaged data for one of these components.

In the Raman spectra of the studied CF (Fig. 3, *c*, *d*), the D and G bands become narrower with increasing t_{HT}, and the relative intensity of the D peak decreases. After heat treatment at $t \sim 1800$ °C, the 2D peak appears, and its intensity relative to the G peak increases with rising processing temperature.

However, after heat treatment at 2800 °C, the differences in the crystalline structure parameters of viscose- and PAN-based CF become insignificant or disappear entirely (see Fig. 3), except for the crystallite size L_a (see Fig. 4).

Fig. 5 shows the dependencies of Raman spectroscopy parameters for viscose-based CFs (*1*) and PAN-based CFs (*2*) on the processing temperature.

It is evident that the positions and widths of the D and G bands systematically change with increasing t_{HT}. In accordance with the results of previous studies, the dependence of the I_D/I_G parameter was previously used by us to evaluate the effective processing temperature of PAN-based CFs [36].

Using a similar approach, empirical expressions for determining the effective processing temperature (t_{eff}, °C) of PAN-based (4) and viscose-based (5) CFs were derived based on the obtained dependencies of the I_D/I_G parameter on t_{HT} (see Fig. 5, *a*):

$$t_{eff} = 2089 - \left(901 \ln \frac{I_D}{I_G}\right), \quad (4)$$

$$t_{eff} = 1815 - \left(641 \ln \frac{I_D}{I_G}\right). \quad (5)$$

Conclusion

The results of the study indicate that viscose-based carbon fibers (CFs) exhibit a significantly lower degree of crystalline structure perfection compared to PAN-based CFs across almost the entire range of heat treatment temperatures. However, high-temperature treatment at 2800 °C largely mitigates these differences, suggesting partial graphitization of viscose-based CFs. Nevertheless, as evidenced by the full set of obtained data, despite the similarity in most crystalline structure parameters, viscose-based CFs do not

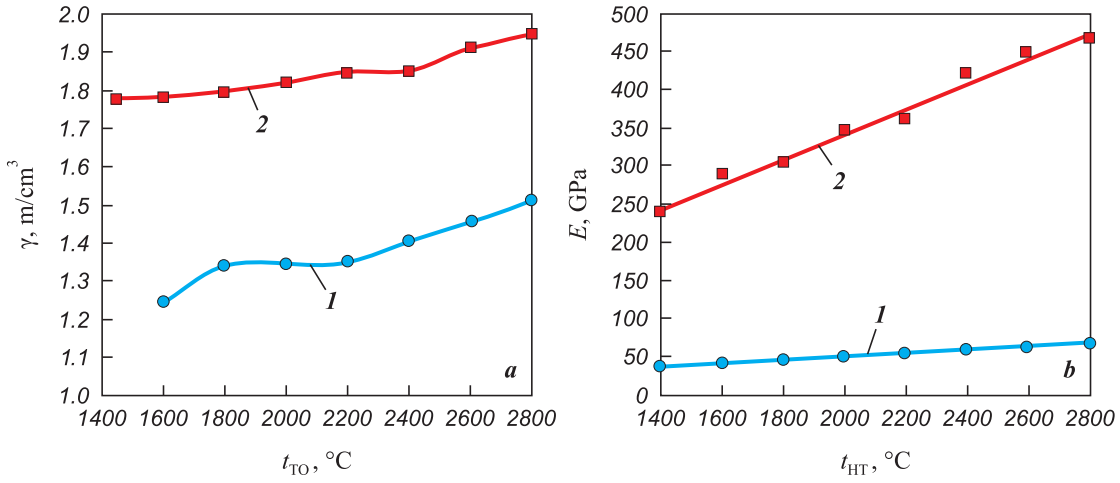

Fig. 2. Dependence of true density (***a***) and dynamic elastic modulus (***b***) on the processing temperature for viscose-based (***1***) and PAN-based (***2***) carbon fibers

Рис. 2. Зависимость истинной плотности (***a***) и динамического модуля упругости (***b***) от температуры обработки УВ на основе вискозы (***1***) и ПАН (***2***)

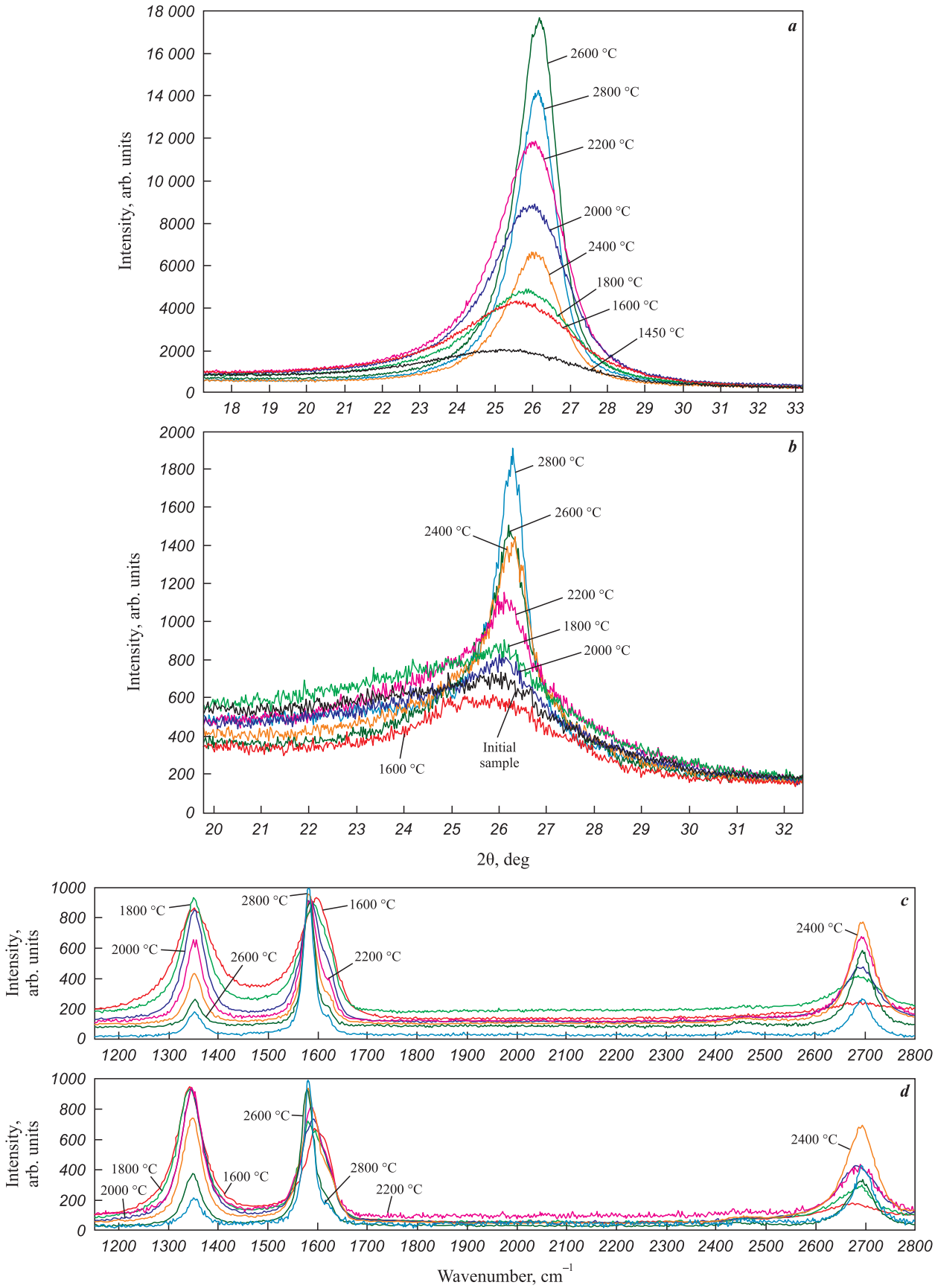

Fig. 3. *X*-ray diffraction patterns of CFs (***a***, ***b***) based on PAN (***a***), and viscose (***b***), and Raman spectra of CFs (***c***, ***d***) based on PAN (***c***), and viscose (***d***)

Рис. 3. Рентгенограммы (***a***, ***b***) и спектры комбинационного рассеяния (***c***, ***d***) УВ на основе ПАН (***a***, ***c***) и вискозы (***b***, ***d***)

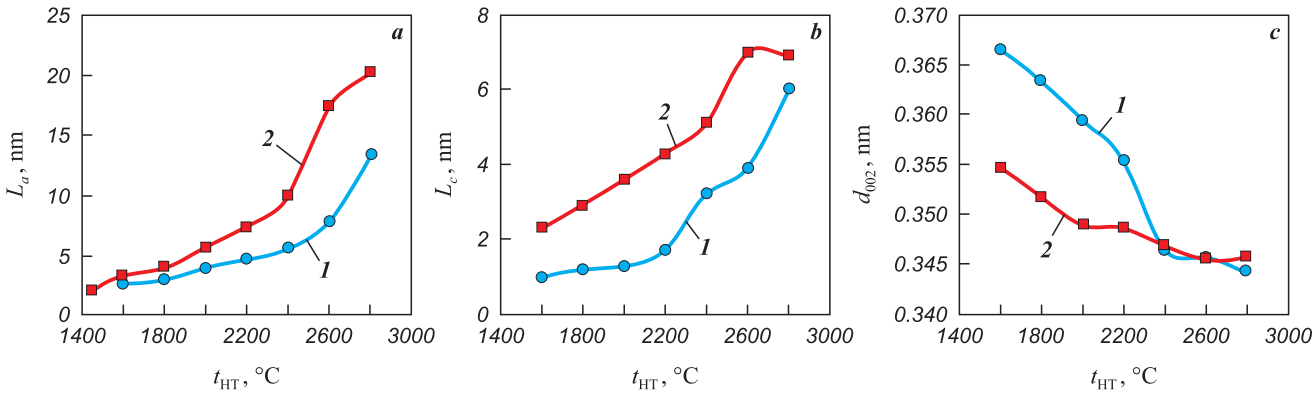

Fig. 4. Dependence of crystalline structure parameters on the processing temperature of fibers based on viscose (***1***) and PAN (***2***)
a – crystallite size L_a; ***b*** – crystallite sizes L_c; ***c*** – interlayer spacing d_{002}

Рис. 4. Температурные зависимости параметров кристаллической структуры волокон на основе вискозы (***1***) и ПАН (***2***)
a – размеры кристаллитов L_a; ***b*** – размеры кристаллитов L_c; ***c*** – межслоевое расстояние d_{002}

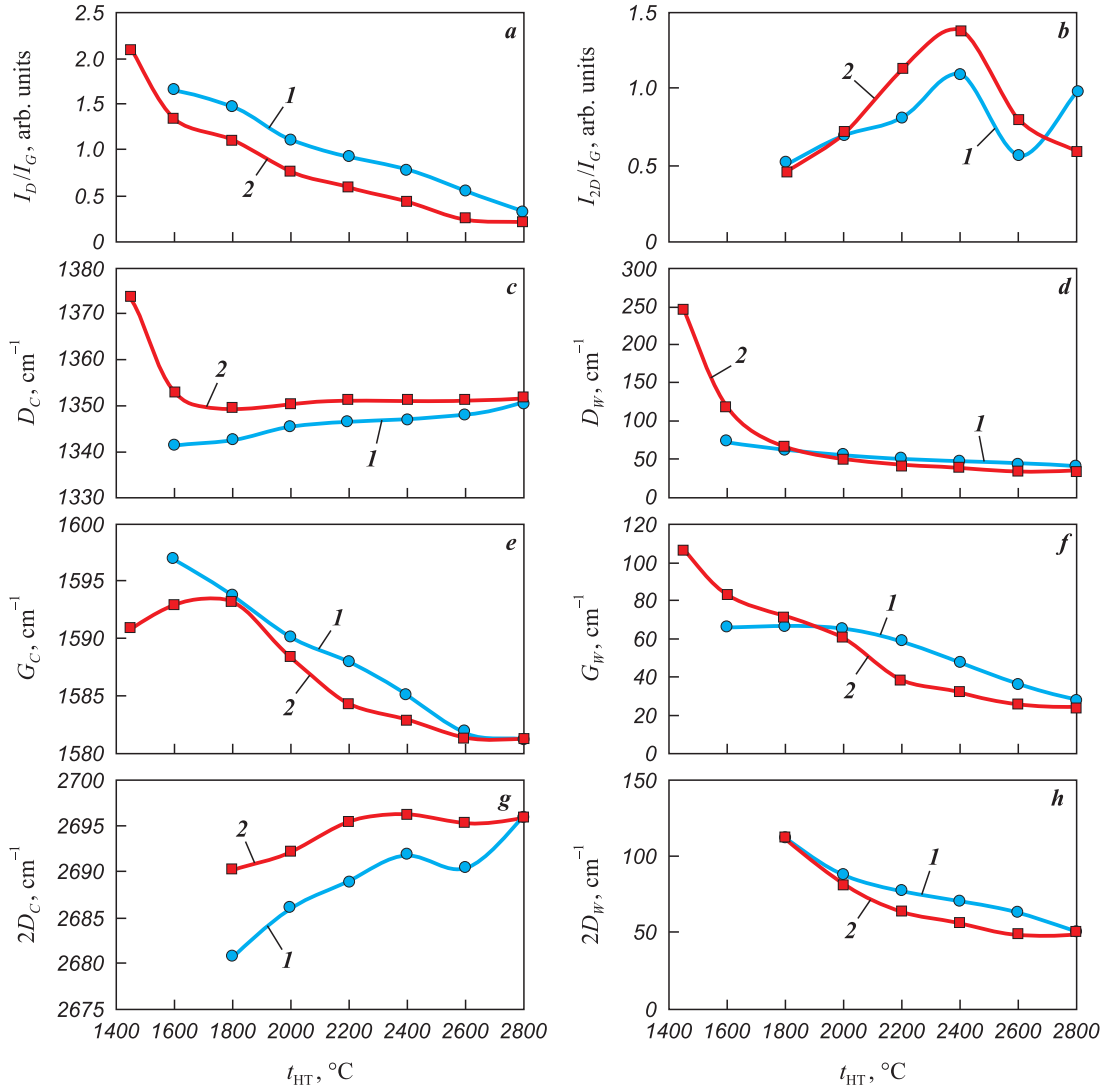

Fig. 5. Dependence of Raman spectroscopy parameters for viscose-based CFs (***1***) and PAN-based CFs (***2***) on the heat treatment temperature

Рис. 5. Зависимости параметров рамановской спектроскопии для УВ на основе вискозы (***1***) и ПАН (***2***) от температуры термообработки

become equivalent to PAN-based CFs even after high-temperature treatment. The elastic modulus of viscose-based CFs does not exceed 100 GPa, which is over four times lower the elastic modulus of PAN-based CFs subjected to identical treatment conditions. The true density of viscose-based CFs remains significantly lower compared to PAN-based CFs (see Fig. 2, *a*), indicating the distinctive nature of their porosity.

These differences, in our view, can be attributed to the inherently low degree of microtexturing in viscose-based CFs compared to PAN-based CFs and, to an even greater extent, to mesophase pitch-based CFs [19; 37]. The closest counterpart to low-modulus viscose-based CFs are fibers produced from isotropic pitches [10], which similarly exhibit reduced true density and microtexturing.

Based on previous studies [7; 22], which found no significant differences in the properties of the raw viscose fibers used for CF production, it can be inferred that the low elastic modulus of the investigated viscose-based CFs is primarily due to the absence of intensive orientational stretching during the graphitization process.

References / Список литературы

1. Gupta M.K., Singhal V., Rajput N.S. Applications and challenges of carbon-fibres reinforced composites: A review. *Evengreen Joint Journal of Novel Carbon Resource Sciences & Green Asia Strategy*. 2022;9(3):682–693. https://doi.org/10.5109/4843099
2. Ince J.C., Peerzada M., Mathews L.D., Pai A.R., Alqatatsheh A., Abbasi S., Yin Y., Hameed N., Duffy A.R., Lau A.K., Salim N.V. Overview of emerging hybrid and composite materials for space applications. *Advanced Composites and Hybrid Materials*. 2023;6(4):130. https://doi.org/10.1007/s42114-023-00678-5
3. Zhao J. Carbon fiber applications in modern rockets. *Preprint*. June 2023. https://doi.org/10.13140/RG.2.2.12957.49126
4. Olofin I., Liu R. The application of carbon fibre reinforced polymer (CFRP) cables in civil engineering structures. *International Journal of Civil Engineering*. 2015;2(7):1–5. https://doi.org/10.14445/23488352/IJCE-V2I7P101
5. Ozkan D., Gok M.S., Karaoglanli A.C. Carbon fiber reinforced polymer (CFRP) composite materials, their characteristic properties, industrial application areas and their machinability. In: *Öchsner A., Altenbach H. (eds). Engineering Design Applications III. Advanced Structured Materials, vol. 124*. Springer, Cham. 2020. P. 235–253. https://doi.org/10.1007/978-3-030-39062-4_20
6. Morgan P. Carbon fibers and their composites. London: Taylor & Francis Group, 2005. 1166 p. https://doi.org/10.1201/9781420028744
7. Park S.-J., Heo G.-Y. Precursors and manufacturing of carbon fibers. In: *Carbon Fibers. Springer Series in Materials Science, vol. 210*. Springer, Dordrecht. 2014. P. 31–66. https://doi.org/10.1007/978-94-017-9478-7_2
8. Emmerich F.G. Young's modulus, thermal conductivity, electrical resistivity and coefficient of thermal expansion of mesophase pitch-basedcarbonfibers. *Carbon*. 2014;79:274–293. https://doi.org/10.1016/j.carbon.2014.07.068
9. Frank E., Steudle L.M., Ingildeev D., Spörl J.M., Buchmeiser M.R. Carbon fibers: Precursor systems, processing, structure, and properties. *Angewandte Chemie International Edition*. 2014;53(21):5262–5298. https://doi.org/10.1002/anie.201306129
10. Newcomb B.A. Processing, structure, and properties of carbon. *Composites Part A: Applied Science and Manufacturing*. 2016;91:262–282. https://doi.org/10.1016/j.compositesa.2016.10.018
11. Mirdehghan S.A. Fibrous polymeric composites. In: *Engineered polymeric fibrous materials. The Textile Institute. Book Series*. Woodhead Publishing, 2021. P. 1–58. https://doi.org/10.1016/B978-0-12-824381-7.00012-3
12. Qiu L., Zheng X.H., Zhu J., Su G.P., Tang D.W. The effect of grain size on the lattice thermal conductivity of an individual polyacrylonitrile-based carbon fiber. *Carbon*. 2013;51:265–273. https://doi.org/10.1016/j.carbon.2012.08.052
13. Sun Z., Lu Y., Wang R., Yang C. Analysis of carbon fiber structure based on dynamic laser Raman spectroscopy. *Journal of Applied Polymer Science*. 2020;138(16):50247. https://doi.org/10.1002/app.50247
14. Li D., Wang H., Wang X. Effect of microstructure on the modulus of PAN-based carbon fibers during high temperature treatment and hot stretching graphitization. *Journal of Materials Science*. 2007;42(12):4642–4649. https://doi.org/10.1007/s10853-006-0519-4
15. Zhou G., Liu Y., He L., Guo Q., Ye H. Microstructure difference between core and skin of T700 carbon fibers in heat-treated carbon/carbon composites. *Carbon*. 2011;49(9):2883–2892. https://doi.org/10.1016/j.carbon.2011.02.025
16. Wu G.-P., Li D.-H., Yang Y., Lu C.-X., Zhang S.-C., Li X.-T., Feng Z.-H., Li Z.-H. Carbon layer structures and thermal conductivity of graphitized carbon fibers. *Journal of Materials Science*. 2011;47(6):2882–2890. https://doi.org/10.1007/s10853-011-6118-z
17. Qin X., Lu Y., Xiao H., Wen Y., Yu T. A comparison of the effect of graphitization on microstructures and properties of polyacrylonitrile and mesophase pitch-based carbon fibers. *Carbon*. 2012;50(12):4459–4469. https://doi.org/10.1016/j.carbon.2012.05.024
18. Sarian S., Strong S.L. Mechanical properties of stress-graphitised carbon fibers: Thermally induced relaxation and recovery. *Fibre Science and Technology*. 1971;4(1):67–79. https://doi.org/10.1016/0015-0568(71)90012-1
19. Diefendorf R.J., Tokarsky E. High-performance carbon fibers. *Polymer Engineering and Science*. 1975;15(3): 150–159. https://doi.org/10.1002/pen.760150306
20. Spörl J. M., Ota A., Son S., Massonne K., Hermanutz F., Buchmeiser M.R. Carbon fibers prepared from ionic liquid-derived cellulose precursors. *Materials Today Com-*

munications. 2016;7:1–10.
https://doi.org/10.1016/j.mtcomm.2016.02.002

21. Bengtsson A., Bengtsson J., Sedin M., Sjöholm E. Carbon fibres from lignin-cellulose precursors: Effect of stabilisation conditions. *ACS Sustainable Chemistry & Engineering*. 2019;7(9):8440–8448.
https://doi.org/10.1021/acssuschemeng.9b00108

22. Dumanli A.G., Windle A.H. Carbon fibres from cellulosic precursors: A review. *Journal of Materials Science*. 2012;47(10):4236–4250.
https://doi.org/10.1007/s10853-011-6081-8

23. Tuinstra F., Koenig J.L. Raman spectrum of graphite. *The Journal of Chemical Physics*. 1970;53(3):1126–1130.
https://doi.org/10.1063/1.1674108

24. Cançado L.G., Takai K., Enoki T., Endo M., Kim Y.A., Mizusaki H., Jorio A., Coelho L.N., Magalhães Paniago R., Pimenta M.A. General equation for the determination of the crystallite size L_a of nanographite by Raman spectroscopy. *Applied Physics Letters*. 2006;88(16):3106–3109.
https://doi.org/10.1063/1.2196057

25. Reich S., Thomsen C. Raman spectroscopy of graphite. *Philosophical Transactions of the Royal Society A: Mathematical, Physical and Engineering Sciences*. 2004; 362(1824):2271–2288.
https://doi.org/10.1098/rsta.2004.1454

26. Ferrari A.C., Robertson J. Interpretation of Raman spectra of disordered and amorphous carbon. *Physical Review B*. 2000;61(20):14095–14107.
https://doi.org/10.1103/physrevb.61.14095

27. Cancado L.G., Jorio A., Martins Ferreira E.H., Stavale F., Achete C.A., Capaz R.B., Moutinho M.V.O., Lombardo A., Kulmala T.S., Ferrari A.C. Quantifying defects in graphene via Raman spectroscopy at different excitation energies. *Nano Letters*. 2011;11(8):3190–3196.
https://doi.org/10.1021/nl201432g

28. Ferrari A.C., Basko D.M. Raman spectroscopy as a versatile tool for studying the properties of graphene. *Nature Nanotechnology*. 2013;8(4):235–246.
https://doi.org/10.1038/nnano.2013.46

29. Zickler Gerald A., Smarsly B., Gierlinger N., Peterlik H., Paris O.A reconsideration of the relationship between the crystallite size L_a of carbons determined by *X*-ray diffraction and Raman spectroscopy. *Carbon*. 2006;44(15): 3239−3246.
https://doi.org/10.1016/j.carbon.2006.06.029

30. Okuda H., Young R. J., Wolverson D., Tanaka F., Yamamoto G., Okabe T. Investigating nanostructures in carbon fibres using Raman spectroscopy. *Carbon*. 2018; 130:178–184.
https://doi.org/10.1016/j.carbon.2017.12.108

31. Samoilov V.M., Samsonova V.B., Nakhodnova A.V., Verbets D.B., Gareev A.R., Bubnenkov I.A., Steparyova N.N., Shvetsov A.A., Bardin N.G. Raman spectroscopy and crystalline structure of polyacrylonitrile-based carbon fibres. *Advanced Materials & Technologies*. 2019;3(15):8–15.
https://doi.org/10.17277/amt.2019.03.pp.008-015

32. Pacault A. Chemistry and physics of carbon. Ed. L. Walker. Vol. 7. N.Y.: Marcel Dekker, 1971. 403 p.

33. Cheblakova E.G. , Kleusov B.S., Sapozhnikov V.I. , Gorina V.A., Malinina Yu.A., Gareev A.R. Investigation of the properties of high-strength fibers by methods of physico-chemical analysis. *Powder Metallurgy and Functional Coatings*. 2023;17(4):34–40.
https://doi.org/10.17073/1997-308X-2023-4-34-40

Чеблакова Е.Г., Клеусов Б.С., Сапожников В.И., Горина В.А., Малинина Ю.А., Гареев А.Р. Исследования свойств высокопрочных волокон методами физико-химического анализа. *Известия вузов. Порошковая металлургия и функциональные покрытия*. 2023;17(4):34–40.
https://doi.org/10.17073/1997-308X-2023-4-34-40

34. Tyumentsev V.A., Fazlitdinova A.G., Podkopaev S.A., Churikov V.V. Fine structure of polyacrylonitrile and carbon fibers. *Izvestiya vuzov. Khimiya i khimicheskaya tekhnologiya*. 2013;56(7):83–87. (In Russ.).

Тюменцев В.А., Фазлитдинова А.Г., Подкопаев С.А., Чуриков В.В. Тонкая структура полиакрилонитрильных и углеродных волокон. *Известия вузов. Химия и химическая технология*. 2013;56(7):83–87.

35. Tyumentsev V.A., Fazlitdinova A.G. Study of the structure of fibrous carbon materials by *X*-ray diffractometry. *Zavodskaya laboratoriya. Diagnostika materialov*. 2019; 85(11):31–36. (In Russ.).
https://doi.org/10.26896/1028-6861-2019-85-11-31-36

Тюменцев В.А., Фазлитдинова А.Г. Исследование структуры волокнистых углеродных материалов методом рентгеновской дифрактометрии. *Заводская лаборатория. Диагностика материалов*. 2019; 85(11):31–36.
https://doi.org/10.26896/1028-6861-2019-85-11-31-36

36. Samoilov V.M., Nakhodnova A.V., Osmova M.A., Verbets D.B., Bubnenkov A.N., Steparyova N.N., Gareev A.R., Fateeva M.A., Shilo D.V., Ovsyannikov N.E. Effective heat treatment temperature of carbon materials in high temperature furnaces: determination by the parameters of raman spectroscopy of witness samples. *Inorganic Materials: Applied Research*. 2021;12(5):1416–1427.
https://doi.org/10.1134/S2075113321050348

Самойлов В.М., Находнова А.В., Осмова М.А., Вербец Д.Б., Бубненков А.Н., Степарева Н.Н., Гареев А.Р., Фатеева М.А., Шило Д.В., Овсянников Н.Е. Определение эффективной температуры обработки углеродных материалов в высокотемпературных печах по параметрам спектроскопии комбинационного рассеяния образцов-свидетелей. *Перспективные материалы*. 2021;1:67–84.
https://doi.org/10.30791/1028-978X-2021-1-67-84

37. Northolt M.G., Veldhuizen L.H., Jansen H. Tensile deformation of carbon fibers and the relationship with the modulus for shear between the basal planes. *Carbon*. 1991;29(8):1267–1279.
https://doi.org/10.1016/0008-6223(91)90046-l

Information about the Authors

Boris S. Kleusov – Senior Researcher, Testing Center, Joint Stock Company "Scientific Research Institute of Structural Materials Based on Graphite named after S.E. Vyatkin" (JSC "NIIgrafit")
ORCID: 0000-0003-3924-2616
E-mail: BSKleusov@rosatom.ru

Vladimir M. Samoilov – Chief Researcher, JSC "NIIgrafit"
ORCID: 0000-0002-9861-905X
E-mail: vmsamoylov@rosatom.ru

Victoria A. Elchavinova – Researcher, JSC "NIIgrafit"
ORCID: 0009-0006-3167-8924
E-mail: Viaelchaninova@rosatom.ru

Dmitry A. Budushin – Intern Researcher, JSC "NIIgrafit"
ORCID: 0009-0002-4239-1145
E-mail: DABudushin@rosatom.ru

Egor M. Litovchenko – Student, D.I. Mendeleev Russian University of Chemical Technology
ORCID: 0009-0001-3381-855X
E-mail: litovtch.egor@yandex.ru

Anna S. Poplavskaya – Engineer, JSC "NIIgrafit"
ORCID: 0009-0004-0028-9411
E-mail: ASPoplavskaya@rosatom.ru

Vladimir A. Vorontsov – Department Head, JSC "NIIgrafit"
ORCID: 0009-0004-2684-1665
E-mail: VlAVorontsov@rosatom.ru

Сведения об авторах

Борис Сергеевич Клеусов – ст. науч. сотрудник Испытательного центра АО «Научно-исследовательский институт конструкционных материалов на основе графита им. С.Е. Вяткина» (АО «НИИграфит»)
ORCID: 0000-0003-3924-2616
E-mail: BSKleusov@rosatom.ru

Владимир Маркович Самойлов – гл. науч. сотрудник АО «НИИграфит»
ORCID: 0000-0002-9861-905X
E-mail: vmsamoylov@rosatom.ru

Виктория Андреевна Ельчанинова – науч. сотрудник АО «НИИграфит»
ORCID: 0009-0006-3167-8924
E-mail: Viaelchaninova@rosatom.ru

Дмитрий Алексеевич Будушин – стажер-исследователь АО «НИИграфит»
ORCID: 0009-0002-4239-1145
E-mail: DABudushin@rosatom.ru

Егор Максимович Литовченко – студент Российского химико-технологического университета им. Д.И. Менделеева
ORCID: 0009-0001-3381-855X
E-mail: litovtch.egor@yandex.ru

Анна Сергеевна Поплавская – инженер АО «НИИграфит»
ORCID: 0009-0004-0028-9411
E-mail: ASPoplavskaya@rosatom.ru

Владимир Алексеевич Воронцов – руководитель направления АО «НИИграфит»
ORCID: 0009-0004-2684-1665
E-mail: VlAVorontsov@rosatom.ru

Contribution of the Authors

B. S. Kleusov – performed *X*-ray phase analysis and participated in the discussion of results.
V. M. Samoilov – conducted data analysis and participated in the discussion of results.
V. A. Elchaninova – conducted Raman spectroscopy.
D. A. Budushin – performed data analysis and prepared for the article.
E. M. Litovchenko – prepared figures for the article and participated in the discussion of data.
A. S. Poplavskaya – conducted scanning electron microscopy.
V. A. Vorontsov – measured the dynamic elastic modulus.

Вклад авторов

Б. С. Клеусов – проведение рентгенофазового анализа, участие в обсуждении результатов.
В. М. Самойлов – анализ данных, участие в обсуждении результатов.
В. А. Ельчанинова – проведение рамановской спектроскопии.
Д. А. Будушин – проведение анализа и подготовка данных для статьи.
Е. М. Литовченко – создание иллюстраций, участие в обсуждении данных.
А. С. Поплавская – проведение сканирующей электронной микроскопии.
В. А. Воронцов – измерение динамического модуля упругости.

Received 16.08.2024
Revised 25.10.2024
Accepted 28.10.2024

Статья поступила 16.08.2024 г.
Доработана 25.10.2024 г.
Принята к публикации 28.10.2024 г.

Nanostructured Materials and Functional Coatings
Наноструктурированные материалы и функциональные покрытия

UDC 666.29 + 620.193
https://doi.org/10.17073/1997-308X-2025-1-40-57

Research article
Научная статья

Research of heat-resistant glass-ceramic coating characteristics in high-speed air plasma flow

A. N. Astapov[1], B. E. Zhestkov[2], A. S. Rtishcheva[2]

[1] **Moscow Aviation Institute (National Research University)**
4 Volokolamskoe Shosse, Moscow 125993, Russia
[2] **Central Aerohydrodynamic Institute named after professor N.E. Zhukovsky**
1 Zhukovsky Str., Zhukovsky, Moscow Region 140180, Russia

lexxa1985@inbox.ru

Abstract. The results of studies of thermophysical and operational characteristics of heat-resistant glass-ceramic coating on 12Cr18Ni10Ti steel in high-speed air plasma flow are presented. The coating was obtained using the slurry-firing technology. The heat treatment was carried out in air at 1400 K for 3 min. The structure of the coating is represented by a matrix based on barium silicate glass with Cr_2O_3 particles evenly distributed within it. The outer layer of the coating, ~3÷5 μm thick, contains many highly dispersed crystals of $BaSi_4O_9$ doped with Cr and Mo, indicating the surface glass phase crystallization. The heat capacity, thermal diffusivity and thermal conductivity of the coating in the temperature range of 293–573 K and at a pressure of 10^5 Pa vary in the ranges of 0.68–0.75 J/(g·K), 0.47–0.43 mm^2/s and 1.198–1.222 W/(m·K), respectively. The average values of coating's specific mass loss and entrainment rates during air plasma flow at a velocity of ~3.5 km/s and heating of the surface to 1593 K were 7.2 mg/cm^2 and 25.9 mg/(cm^2·h). The spectral emissivity of the coating at a wavelength of 890 nm and the rate of heterogeneous recombination of flux atoms and ions on its surface were 0.85±0.02 and 14±3 m/s. Glass phase provides effective protection of steel from high-temperature oxidation and self-healing of defects. Refractory Cr_2O_3 particles along with surface's glass phase crystallization increase the resistance of the coating to erosion entrainment in the high-speed air plasma flow, its emissivity and catalyticity. The reduction of the thermal conductivity of the coating to 0.04±0.01 W/(m·K) at a temperature of 1054±10 K and a pressure of ~200 Pa is experimentally established and confirmed by numerical modelling. The explanation of the effect is presented.

Keywords: glass enamel, glass-ceramic coating, heat resistance, oxidation, emissivity, catalyticity, gas dynamic tests, modeling

Acknowledgements: The work was carried out within the framework of a grant from the Russian Science Foundation № 22-19-00352, https://rscf.ru/project/22-19-00352/.

For citation: Astapov A.N., Zhestkov B.E., Rtishcheva A.S. Research of heat-resistant glass-ceramic coating characteristics in high-speed air plasma flow. *Powder Metallurgy and Functional Coatings*. 2025;19(1):40–57. https://doi.org/10.17073/1997-308X-2025-1-40-57

Исследование характеристик жаростойкого стеклокерамического покрытия в скоростном потоке воздушной плазмы

А. Н. Астапов[1], Б. Е. Жестков[2], А. С. Ртищева[2]

[1] **Московский авиационный институт (национальный исследовательский университет)**
Россия, 125993, г. Москва, Волоколамское шоссе, 4
[2] **Центральный аэрогидродинамический институт им. профессора Н.Е. Жуковского**
Россия, 140180, Московская обл., г. Жуковский, ул. Жуковского, 1

lexxa1985@inbox.ru

Аннотация. Представлены результаты исследований теплофизических и эксплуатационных характеристик жаростойкого стеклокерамического покрытия на стали 12Х18Н10Т в скоростном потоке воздушной плазмы. Покрытие получали по шликерно-обжиговой технологии. Термическую обработку проводили на воздухе при температуре 1400 К в течение 3 мин. Структура покрытия представлена матрицей на основе бариевосиликатного стекла с равномерно распределенными в нем частицами Cr_2O_3. Наружный слой покрытия толщиной ~3÷5 мкм содержит множество высокодисперсных кристаллов $BaSi_4O_9$, легированных Cr и Mo, свидетельствующих о поверхностной ситаллизации стеклофазы. Теплоемкость, температуропроводность и теплопроводность покрытия в интервале температур 293–573 К при давлении 10^5 Па изменяются в диапазонах 0,68–0,75 Дж/(г·К), 0,47–0,43 мм^2/с и 1,198–1,222 Вт/(м·К) соответственно. Средние значения удельной потери массы и скорости уноса покрытия при обтекании воздушной плазмой со скоростью ~3,5 км/с и нагреве поверхности до 1593 К составили 7,2 мг/см^2 и 25,9 мг/(см^2·ч). Спектральная излучательная способность покрытия на длине волны 890 нм и скорость гетерогенной рекомбинации атомов и ионов потока на его поверхности составили 0,85±0,02 и 14±3 м/с. Стеклофаза обеспечивает эффективную защиту стали от высокотемпературного окисления и самозалечивание дефектов. Тугоплавкие частицы Cr_2O_3 наряду с поверхностной ситаллизацией стеклофазы повышают сопротивление покрытия эрозионному уносу в скоростном потоке воздушной плазмы, его излучательную способность и каталитичность. Экспериментально установлено и подтверждено численным моделированием снижение теплопроводности покрытия до 0,04±0,01 Вт/(м·К) при температуре 1054±10 К и давлении ~200 Па. Представлено объяснение эффекта.

Ключевые слова: стеклоэмаль, стеклокерамическое покрытие, жаростойкость, окисление, излучательная способность, каталитичность, газодинамические испытания, моделирование

Благодарности: Исследование выполнено за счет гранта Российского научного фонда № 22-19-00352, https://rscf.ru/project/22-19-00352/.

Для цитирования: Астапов А.Н., Жестков Б.Е., Ртищева А.С. Исследование характеристик жаростойкого стеклокерамического покрытия в скоростном потоке воздушной плазмы. *Известия вузов. Порошковая металлургия и функциональные покрытия*. 2025;19(1):40–57. https://doi.org/10.17073/1997-308X-2025-1-40-57

Introduction

High-temperature gas corrosion of alloyed steels and nickel-based alloys is accompanied by the formation of scale on their surface, consisting of phases with variable compositions, as well as internal oxidation zones within the subscale layers. This process leads to the depletion of alloying elements, particularly Nb, Mo, and W in alloys, and decarburization in steels [1; 2]. These changes in chemical composition, in turn, result in the degradation of the mechanical properties and operational performance of the materials. The challenges become significantly more severe when alloys are exposed to high-velocity flows of oxygen-containing gases [3]. Under such conditions, oxidation processes accelerate, leading to the degradation and delamination of the oxide films formed on the surface. Additionally, the development of surface microrelief becomes more pronounced, resulting in increased roughness, corrosion-erosion pitting, and cavity formation. These factors, in turn, contribute to greater gas turbulence in boundary regions and intensify the erosion-induced material degradation. Protecting alloys from high-temperature gas corrosion and erosion using thin-layer heat-resistant coatings is often the only viable method to maintain their high-temperature strength and functional properties. For this purpose, silicate-based glass-ceramic and glass-crystalline coatings are widely employed.

The compositions of frits (granulated glass enamels) for glass-ceramic coatings used to protect steels and nickel alloys from high-temperature gas corrosion generally contain the following main components, wt. %: 25–85 SiO_2, 20–50 BaO, 0–20 B_2O_3, 0–5 Al_2O_3, 0–3 MgO, 0–5 CaO [4]. To improve the adhesion properties of the formed coatings, frits include small amounts of adhesion-promoting oxides such as CoO,

NiO, MnO, and MoO_3. To enhance the functional properties of the coatings (chemical resistance, erosion resistance, blackness degree, heat reflectivity, etc.), fillers such as Cr_2O_3, Al_2O_3, TiO_2, ZrO_2, $ZrSiO_4$, SiB_4, SiC, and others are introduced either through the charge during frit production or as milling additives during slurry preparation.

At present, an extensive range of resource-efficient glass-ceramic coatings has been developed, ensuring the operability of the studied materials at temperatures of 1150–1373 K for prolonged periods and up to 1473 K for short-term exposure, including in high-speed aggressive gas flows [4–6]. Among these developments, the majority are heat-resistant coatings designed for the effective protection of components and assemblies of gas turbine engines and turbopump units [1; 6–11]. However, technical solutions aimed at improving the reliability of structural elements in liquid rocket engines (for manned and cargo spacecraft, space stations, etc.) remain relatively scarce [5; 12]. There are virtually no developments in the field of protecting heat-loaded components of airframes for high-speed maneuvering aircraft and their propulsion systems [13–15]. This is primarily due to temperature-time factors that significantly limit the applicability of traditional structural materials in so-called hot structures. The challenge of ensuring short-term operability of steels and nickel alloys at temperatures of 1523–1573 K under high-speed flows (air, combustion products) remains highly relevant.

A previous invention [15] described a heat-resistant glass-ceramic coating with enhanced resistance to erosion in high-speed gas flows, providing effective protection of steels and nickel alloys during long-term operation at temperatures up to 1273 K (over 1000 h) and short-term exposure up to 1623 K (at least 15 min).

The objective of this study was to investigate the thermophysical and operational characteristics of this coating under high-speed air plasma flow conditions at surface temperatures reaching 1593 K.

1. Materials and methods

The starting components for frit production included silicon oxide (SiO_2) powders (particle size <20 μm, purity 99.9 %), barium oxide (BaO) (<63 μm, 98 %), calcium oxide (CaO) (<63 μm, 98 %), chromium oxide (Cr_2O_3) (<10 μm, 99.9 %), aluminum oxide (Al_2O_3) (<10 μm, 98.5 %), cobalt oxide (CoO) (<45 μm, 98 %), titanium oxide (TiO_2) (<20 μm, 99.8 %), manganese oxide (Mn_2O_3) (<20 μm, 99 %), molybdenum oxide (MoO_3) (<3 μm, 99.9 %), and silicon tetraboride (SiB_4) (<10 μm, 99.9 %). The components were mixed according to [15] and ground in a Pulverisette-5 planetary mill (Fritsch, Germany) using a 500 mL ZrO_2 container for 180 min at a rotational speed of 400 rpm, with a mixture-to-grinding body mass ratio of 1:10. The prepared charge was placed into a 310 mL platinum crucible and melted at 1850 K for 100 min in an SVK-5163 resistance furnace (Russia) equipped with chromite-lanthanum heaters and a 3 L chamber volume. Granulation was performed by pouring the melt from the crucible into cold water.

The frit was dispersed in a high-energy ball mill "SamplePrep 8000 M-230" (Spex, USA) in a WC container with a volume of 55 mL for 60 min at a reciprocating frequency of 1080 cycles/min with short lateral movements, and a frit-to-grinding media mass ratio of 1:5. The slurry composition was prepared by mixing and wet milling the frit with kaolinite clay from the Chasov-Yar deposit, and water in the same mill for 90 min with a slurry-to-grinding media mass ratio of 1:3. The slurry's readiness was monitored by sieving it through a 63 μm mesh sieve with virtually no residue.

Austenitic stainless steel samples of grade 12Cr18Ni10Ti (wt. %: C ~ 0.12; Cr ~ 18; Ni ~ 10; Ti ~ 0.8; Fe – balance) were used as substrates, shaped as *U*-shaped plates with dimensions of 30×30×0.8 mm and side heights of 10 mm, as well as cylindrical samples with a diameter of 50 mm and a height of 30 mm. The sample surfaces were prepared using sandblasting with electrocorundum particles sized 50–63 μm at a pressure of 5 atm, followed by ultrasonic cleaning in isopropyl alcohol. The slurry was applied to the sample surfaces by spray coating using an airbrush with a nozzle and needle diameter of 0.8 mm. The coated layers were dried under ambient conditions with warm air (323 K) from a heater for 30 min. The firing process was conducted in a TK.4.1400.1F furnace (LLC Termokeramika, Russia) at a temperature of 1400 K for 3 min. The samples were then cooled in air at room temperature.

To determine the density and thermal diffusivity of the coating material, a compact sample with a diameter of 12.37 mm and a thickness of 1.5 mm was fabricated from the frit. The frit powder was loaded into a graphite mold and consolidated using the spark plasma sintering method on the Labox-650 system (Sinter Land Inc., Japan). The process was carried out in a vacuum at a residual pressure of 40–50 Pa, a heating rate of 80 K/min, a temperature of 973 K, a pressure of 50 MPa, and an isothermal holding time of 20 min.

The density (ρ) was determined by the hydrostatic weighing method using GR-202 analytical scales (AND, Japan) with an accuracy of 10^{-4} g. The thermal diffusivity (α) was measured using the laser flash method on the LFA447 NanoFlash device (Netzsch, Germany)

in a high-purity argon atmosphere of grade 6.0. The specific heat capacity (C_p) was determined using a differential scanning calorimeter DSC 204 F1 (Netzsch, Germany) at a heating/cooling rate of 5 K/min within the temperature range of 373–593 K under an argon flow of the same grade. The obtained data were processed using the Proteus Analysis 6 software (Netzsch, Germany). Based on the results, the thermal conductivity (λ) was calculated using the formula

$$\lambda = \alpha C_p \rho. \quad (1)$$

Gas-dynamic tests of the samples were conducted on an aerodynamic test stand equipped with an induction plasma torch, following the methodology described in [16]. The samples were positioned coaxially to the flow at a distance of 100 mm from the nozzle exit to the front surface of the coating. To determine the test parameters, a computational experiment was conducted, with the mathematical formulation and results provided in Section 2.3. In this study, the test conditions included a stagnation temperature $T_0 \sim 6000 \div 6500$ K, a Mach number M = 4.7, a speed of 3.54 km/s, and specific heat flux values $q_w \sim 15 \div 30$ W/cm^2. The brightness temperature (T_b) of the sample front surface was measured using the VS-CTT-285/E/P-2001 brightness pyrometer (LLC Videoscan, Russia) at a wavelength of 890 nm. Changes in the spectral emissivity of the samples during testing were assessed by analyzing the ratio of radiation intensities at the brightness and spectral temperatures, measured simultaneously using the USB2000+ spectrometer (Ocean Optics, USA) from the sample's front surface. The thermodynamic (true) temperature (T_w) of the sample's front surface was determined by recalculating the brightness temperature measured by the pyrometer, accounting for the established variation in emissivity at a wavelength of 890 nm. The mass of the samples before and after fire testing was measured using the same analytical scales as in the hydrostatic weighing method.

The heterogeneous recombination rate constant of atoms and ions (K_w) on the active centers of the coating surface was determined based on the difference in the heat flux density between the reference and the investigated compositions, tested under identical conditions. Using parametric numerical modeling of the flow and heat transfer around the samples, the derivative dK_w/dT_b [16] was calculated [16]. The value of K_w for the investigated coating was determined based on the known value of K_{ws} for the reference sample, the magnitude of dK_w/dT_b and the difference in brightness temperatures ΔT_b of the thermally insulated investigated and reference samples, according to the following formula [16]:

$$K_w = K_{ws} + \left(\frac{dK_w}{dT_b}\right)\Delta T_b. \quad (2)$$

The product of K_w and the concentration of atoms and ions n indicates the number of atoms and ions recombining on a unit surface of the coating per second. As reference samples, samples made of fibrous thermal protection material quartz TZMK-25 with a heat-resistant enamel coating EVCH-4M1U [17] were used, for which $K_{ws} = 0.1 \div 0.3$ m/s at temperatures of 400–1550 K.

The chemical composition of the frit powder was determined using *X*-ray fluorescence (XRF) analysis on an ARL OPTIM'X wavelength spectrometer (Thermo Fisher Scientific, Switzerland), which does not allow for the identification of light elements such as boron, carbon, and oxygen.

X-ray diffraction (XRD) patterns were recorded using the Bragg–Brentano geometry on an ARL X'tra diffractometer (Thermo Fisher Scientific, Switzerland) equipped with a Peltier detector and a copper anode CuK_α. The measurements were performed with a step size of 0.02° at a goniometer radius of 520 mm, at a scanning speed of 0.5 °/min, within the angular range of $2\theta = 10 \div 90°$. For qualitative phase analysis, the Crystallographica Search-Match software (Oxford Cryosystems, UK) and the ICDD PDF-2 database (2010) of standard *X*-ray patterns were used.

Microstructural studies were conducted using an EVO-40 scanning electron microscope (SEM) (Carl Zeiss, Germany), equipped with an X-Max 50 energy-dispersive *X*-ray spectrometer (EDS) (Oxford Instruments, UK). Imaging was performed in both secondary and backscattered electron modes. Quantitative information on the local elemental composition of the phases was obtained using EDS at an accelerating voltage of 15 kV and a probe current of 0.5–1.5 nA. For the preparation of metallographic sections, precision equipment from Struers (Denmark) was used.

2. Results and discussion

2.1. Composition, structure, and properties of the glass-ceramic coating

The chemical composition of the melted frit, expressed in terms of oxides (wt. %), is as follows): BaO – 34.4; SiO_2 – 30.9; Cr_2O_3 – 22.3; CaO – 3.5; TiO_2 – 2.1; CoO – 1.9; MnO – 1.9; Al_2O_3 – 1.6; MoO_3 – 1.4. *X*-ray phase analysis revealed that Cr_2O_3 is the only crystalline phase in the frit, exhibiting rhombohedral symmetry with unit cell parameters of a = 0.49553 nm

and c = 1.3581 nm. The absence of other crystalline phases, particularly SiO_2, suggests that the synthesized barium silicate glass is in an *X*-ray amorphous state. The composition of the resulting frit meets the concentration limits specified in the invention [15].

Fig. 1 presents the microstructures of the cross-section and surface of the glass-ceramic coating on 12Cr18Ni10Ti steel, shown in reflected and secondary electron images, characteristic *X*-ray radiation of elements, and a multilayer composite image created by combining electron micrographs and *X*-ray maps. The coating exhibits a heterogeneous structure, consisting of a barium silicate glass matrix with uniformly distributed Cr_2O_3 particles, with a size of no more than 10 μm. The coating thickness is 50±5 μm. The structure of the coating reveals the presence of sporadic pores and gas bubbles (Fig. 1, *a*, *b*) ranging from 4–6 μm in size (occasionally up to 10 μm). Their formation occurs during the firing process and is associated with the encapsulation of gaseous reaction products within the viscous glass phase.

According to SEM and EDS data, the formation of the coating is accompanied by a decrease in Cr content and an increase in Fe, Ni, and Ti concentrations in the surface layers of the substrate to a depth of 3–4 μm (Table 1). The glass phase near the "substrate–coating" interface contains an increased proportion of Cr_2O_3, along with small amounts of iron and nickel oxides. According to [4], the dissolution of Cr_2O_3 in the glass ceases once its content reaches

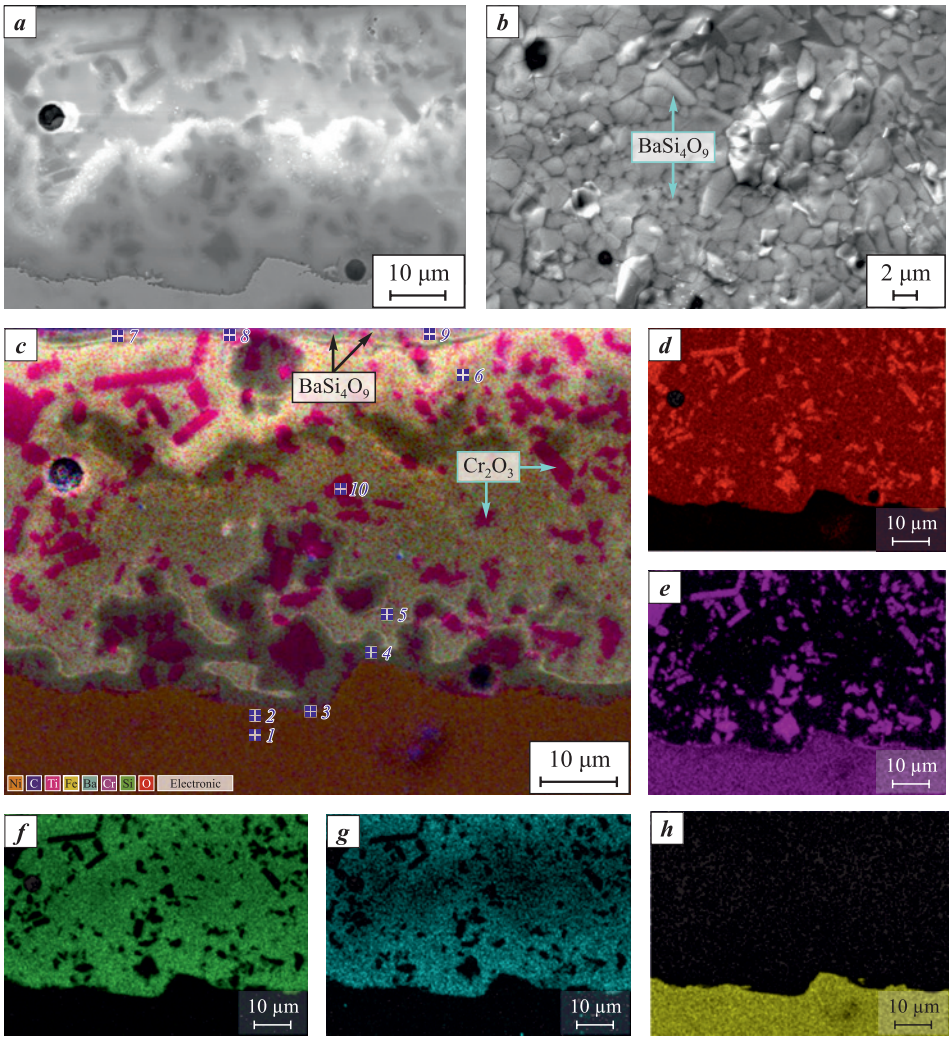

Fig. 1. Microstructure of cross section (***a***, ***c***–***h***) and surface (***b***) of glass-ceramic coating in initial state on steel 12Cr18Ni10Ti: in reflected (***a***) and secondary (***b***) electrons; combined image (***c***); maps of element distribution in characteristic *X*-ray radiation: OK_{α_1} (***d***); CrK_{α_1} (***e***); SiK_{α_1} (***f***); BaL_{α_1} (***g***); FeK_{α_1} (***h***)

Рис. 1. Микроструктура поперечного сечения (***a***, ***c***–***h***) и поверхности (***b***) стеклокерамического покрытия в исходном состоянии на стали 12Х18Н10Т: в отраженных (***a***) и вторичных (***b***) электронах; комбинированное изображение (***c***); карты распределения элементов в характеристическом рентгеновском излучении: OK_{α_1} (***d***); CrK_{α_1} (***e***); SiK_{α_1} (***f***); BaL_{α_1} (***g***); FeK_{α_1} (***h***)

Table 1. **Local chemical composition of areas on the cross section of 12Cr18Ni10Ti specimen with glass-ceramic coating in the initial state**

Таблица 1. **Локальный химический состав областей на поперечном сечении образца из 12Х18Н10Т со стеклокерамическим покрытием в исходном состоянии**

Spectrum No. in Fig. 1, *c*	Analysis location	Element content												
		%	O	Ni	Fe	Cr	Si	Ba	Mo	Ca	Co	Mn	Al	Ti
1	5–7 μm from the coating interface	wt.	–	9.1	72.1	18.3	0.3	–	–	–	–	–	–	0.2
2	2–3 μm from the coating interface	wt.	–	9.8	74.8	15.1	–	–	–	–	–	–	–	0.3
3	At the coating interface	wt.	–	10.0	77.5	10.4	0.2	–	–	–	–	–	1.2	0.6
4	Glass phase 2–3 μm from the substrate	at.	57.5	0.4	3.8	5.0	19.4	9.2	0.2	1.5	0.7	0.8	1.4	–
5	Glass phase 6–8 μm from the substrate	at.	62.0	–	–	4.7	19.4	9.3	0.3	1.6	0.4	0.9	1.4	-
6	Glass phase 6–8 μm from the coating surface	at.	61.2	–	–	5.6	19.1	9.2	0.3	1.7	0.7	0.9	1.2	–
7	Outer coating layer	at.	57.7	–	–	9.1	13.4	14.6	2.6	1.4	–	–	1.2	–
8		at.	58.4	–	–	11.1	13.8	11.2	1.7	1.3	0.6	0.8	1.1	–
9		at.	57.1	–	–	8.3	16.5	12.5	1.2	1.8	0.6	0.8	1.2	–
10	Cr_2O_3 particle in the glass phase	at.	61.9	–	–	37.8	0.3	–	–	–	–	–	–	–

approximately 2.5 wt. %. At a distance of 6–8 μm from the substrate interface, the glass phase acquires the characteristic chemical composition of the coating (Table 1). The presented data indicate that the enamel melt of the coating dissolves the primary scale that forms on 12Cr18Ni10Ti steel during the initial stage of firing. The formation of this scale occurs as oxygen penetrates the substrate surface through throughpores in the yet unmelted slurry layer. The dissolution of scale in the glass enamel during firing, along with the presence of adhesion-promoting oxides (CoO, MnO, and MoO_3), contributes to improved adhesion between the coating and the substrate.

The coating surface is characterized by a glassy luster and a dark green color. The outer coating layer, approximately 3–5 μm thick, contains numerous highly dispersed crystals with a high content of Ba, Cr, and Mo (Table 1), indicating surface crystallization of the glass phase. This corresponds to the upward mass transfer of Ba^{2+}, Cr^{3+}, and Mo^{6+} cations towards the surface, moving opposite to the concentration gradient. The crystal sizes range from 1.5–2.0 to 3–4 μm (Fig. 1, *b*).

According to *X*-ray diffraction analysis, the primary crystalline phase in the coating, as in the frit, is Cr_2O_3 with a rhombohedral crystal system. In addition, the presence of the $BaSi_4O_9$ phase with a trigonal structure and unit cell parameters of a = 1.1338 nm and c = 0.4548 nm was identified. The observed increase in these parameters compared to the reference values (a = 1.12469 nm and c = 0.44851 nm [18]) is likely due to the doping of the lattice with chromium and molybdenum cations, which is consistent with EDS data. Notably, the $BaSi_4O_9$ phase is known only as a high-pressure polymorph [18], and its formation through surface crystallization of the glass phase requires further investigation. The absence of other crystalline phases indirectly suggests that the matrix phase based on barium silicate glass remains in an *X*-ray amorphous structure.

The average density of the coating, determined by the hydrostatic weighing method, was ρ = 3.813 g/cm^3. Fig. 2 presents the thermophysical properties of the coating within the temperature range of 373–593 K. As the temperature increases, the heat capacity increases in a non-linear manner, while the thermal diffusivity decreases linearly. The latter behavior is typical for glass-ceramics and is attributed to increased phonon scattering with rising temperature. The coating exhibits relatively low heat capacity, with C_p = 0.68÷0.75 J/(g·K) within the temperature range of 373÷593 K. The thermal diffusivity of the coating decreases linearly from 0.47 to 0.43 mm^2/s in the range of 293–573 K. Data approximation was performed using regression analysis in Microsoft Excel. The approximation results and their reliability (coefficient of determination R^2) are shown in Fig. 2. The thermal con-

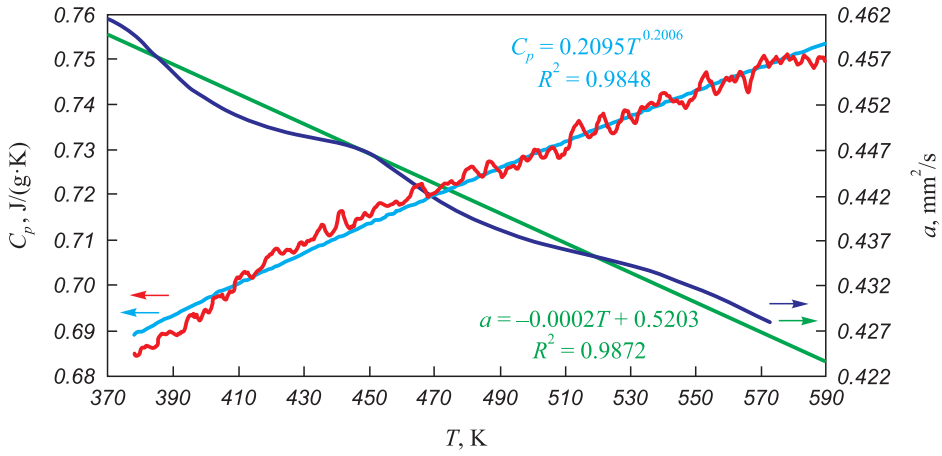

Fig. 2. Temperature dependencies of heat capacity (C_p) and thermal diffusivity (α) of glass-ceramic coating

Рис. 2. Температурные зависимости теплоемкости (C_p) и температуропроводности (α) стеклокерамического покрытия

ductivity of the coating, calculated using equation (1), shows minimal variation within the temperature range of 293–573 K and is λ = 1.21±0.012 W/(m·K).

2.2. Results of gas-dynamic testing of the glass-ceramic coating

Samples made of 12Cr18Ni10Ti steel in the form of *U*-shaped plates with a glass-ceramic coating were sequentially installed into a cylindrical holder with a diameter of 50 mm, made of TZMK-25, flush with its end surface. A non-fired coating of the Si–$TiSi_2$–$MoSi_2$–TiB_2–SiO_2 system [19] was applied to the holder's end surface to enhance its erosive resistance and increase its emissivity. The tests were carried out under stepwise gas-dynamic heating conditions using an air plasma flow, with the front surface temperature ranging from T_w = 1193÷1593 K. Typical fire test results are shown in Fig. 3, *a* as profiles of the brightness temperature (T_b) and thermodynamic temperature (T_w) at the critical point of the front surface (curves *1* and *2*), the preheater chamber pressure (P_0, curve *3*) and the anode power input (W_a, curve *4*). Fig. 3, *b* and *c* display photographs of the sample during testing and the coating's front surface after testing, respectively. The test series included five samples, and each fire test lasted 1000 s. The results exhibited good reproducibility, indicating the consis-

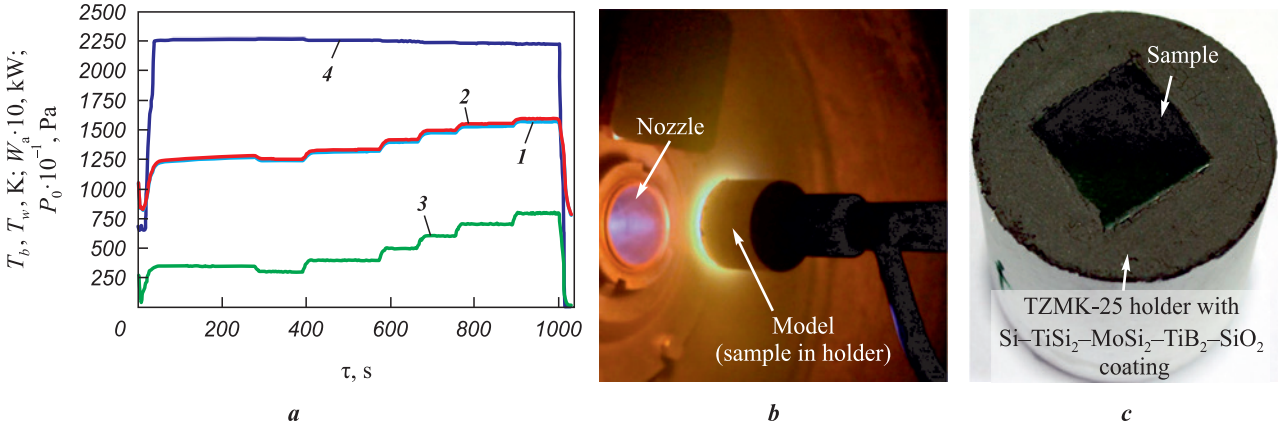

a ***b*** ***c***

Fig. 3. Results of gas-dynamic tests of a specimen made of 12Cr18Ni10Ti steel with glass-ceramic coating (***a***), photo of the model during the test (***b***) and appearance of the specimen face in a holder made of TZMK-25 after its completion (***c***)

1 and ***2*** – brightness (T_b) and thermodynamic (T_w) temperature at the critical point of the coating face;
3 – pressure in the heater prechamber (P_0); ***4*** – anode input power (W_a)

Рис. 3. Результаты газодинамических испытаний образца из стали 12Х18Н10Т со стеклокерамическим покрытием (***a***), фотография модели в процессе испытания (***b***) и внешний вид лицевой стороны образца в державке из ТЗМК-25 после его окончания (***c***)

1 и ***2*** – яркостная (T_b) и термодинамическая (T_w) температуры в критической точке лицевой поверхности покрытия;
3 – давление в форкамере подогревателя (P_0); ***4*** – мощность питания анода (W_a)

tency of the physico-chemical processes occurring in the coating during its interaction with the air plasma, as well as the low magnitude of random errors. The average specific mass loss and erosion rate of the coating during the tests were determined to be 7.2 mg/cm^2 and 25.9 mg/(cm^2·h), respectively. Throughout the fire tests, the spectral emissivity of the coating at a wavelength of 890 nm remained nearly constant at ε = 0.85±0.02. The high degree of blackness of the coating is mainly attributed to the presence of numerous Cr_2O_3 particles within the structure, which exhibit a high emissivity (ε = 0.9). Additionally, surface crystallization contributes to enhanced radiation effects at interfacial irregularities. The stability of the emissivity value throughout the test confirms the high thermochemical stability of the coating.

Fig. 4 presents the microstructures of the cross-section and surface of the glass-ceramic coating on 12Cr18Ni10Ti steel after the fire test, shown as secondary electron images, characteristic *X*-ray radiation element maps, and a multilayer composite image.

The coating surface retained its gloss and dark green color. The structure of the outer layer consists of $BaSi_4O_9$ phase crystals, whose size increased to 10–15 μm (Fig. 4, *b*) compared to the initial state (Fig. 1, *b*). Their growth is likely due to recrystallization via the Ostwald mechanism.

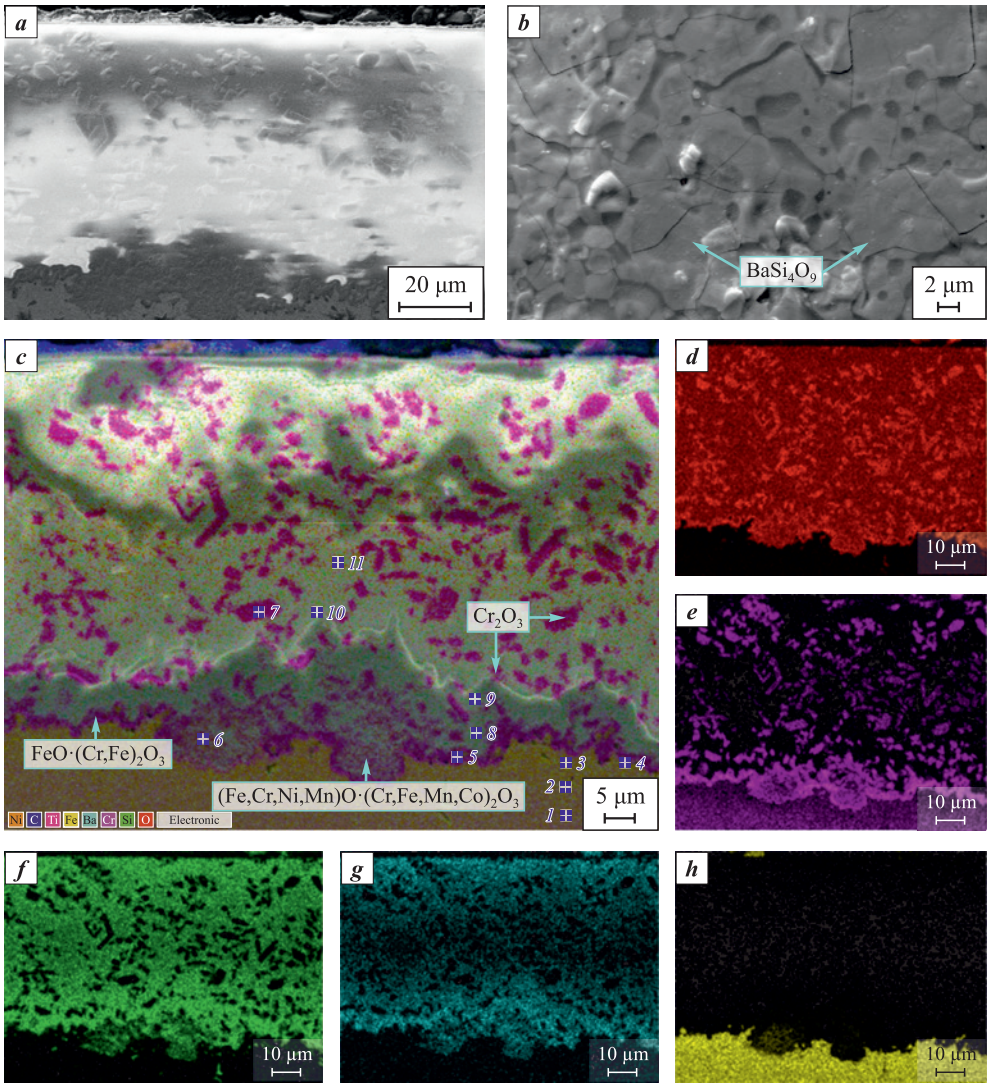

Fig. 4. Microstructure of cross section (***a***, ***c***–***h***) and surface (***b***) of glass-ceramic coating on 12Cr18Ni10Ti steel after fire tests: in secondary electrons (***a***, ***b***); combined image (***c***); maps of element distribution in characteristic *X*-ray radiation: OK_{α_1} (***d***); CrK_{α_1} (***e***); SiK_{α_1} (***f***); BaL_{α_1} (***g***); FeK_{α_1} (***h***)

Рис. 4. Микроструктура поперечного сечения (***a***, ***c***–***h***) и поверхности (***b***) стеклокерамического покрытия на стали 12Х18Н10Т после огневого эксперимента: во вторичных электронах (***a***, ***b***); комбинированное изображение (***c***); карты распределения элементов в характеристическом рентгеновском излучении: OK_{α_1} (***d***); CrK_{α_1} (***e***); SiK_{α_1} (***f***); BaL_{α_1} (***g***); FeK_{α_1} (***h***)

The coating exhibits a heterogeneous, low-porosity structure, comprising a glass phase, Cr_2O_3 and $BaSi_4O_9$ particles, as well as spinel particles of complex composition $(Fe,Co,Ni,Mn)O\cdot(Cr,Fe,Mn,Co)_2O_3$, which are located within a zone extending up to 10–15 μm from the substrate interface (Fig. 4, *c*). The iron oxide content in the glass gradually decreases with distance from the substrate (Table 2). At the substrate-coating interface, an interface layer with a thickness of approximately 1.5–2.5 μm is formed, based on iron chromite $FeO\cdot(Cr,Fe)_2O_3$ (Fig. 4, *c*, Table 2). In the surface layers of the substrate, up to a depth of 5–6 μm, a significant decrease in Cr content is observed, accompanied by an increase in Ni and Fe concentrations. In the $FeO\cdot(Cr,Fe)_2O_3$ phase, iron is present in excess, allowing for its unrestricted diffusion through the sublayer, as evidenced by the presence of iron in the glass phase. Nevertheless, the sublayer acts as a diffusion barrier, reducing the intensity of component mass transfer. The oxidation of the substrate's surface layer and the cations diffusing from the alloy into the coating primarily occurs due to the transport of oxidizing agents through discontinuities and defects in the coating, along the interfaces of the glassy matrix and the mentioned particles. The presence of variable-valence cations (Fe, Co, Mn, Mo) in the coating promotes oxygen absorption from the gas flow.

According to *X*-ray diffraction analysis, the main crystalline phases in the coating after testing, as in the initial state, are Cr_2O_3 with a rhombohedral crystal system and $BaSi_4O_9$ with a trigonal structure. Additionally, a small amount of Fe_3O_4 (magnetite) phase in an orthorhombic modification with unit cell parameters $a = 0.5912$ nm, $b = 0.5945$ nm, and $c = 0.8388$ nm was detected, which correlates well with the SEM and EDS results. The narrowing and increased intensity of diffraction reflections from the $BaSi_4O_9$ phase indicate the gradual progression of crystallization into the coating depth. The absence of other crystalline phases indirectly suggests that the barium silicate glass matrix phase retains its *X*-ray amorphous state.

Based on the results of the conducted tests and the presented research data, it can be concluded that the protective properties of the coating remain intact. The glass phase effectively shields the substrate from

***Table 2.* Local chemical composition of areas on the cross section of 12Cr18Ni10Ti sample with glass-ceramic coating specimen after the fire experiment**

***Таблица 2.* Локальный химический состав областей на поперечном сечении образца из 12Х18Н10Т со стеклокерамическим покрытием после огневого эксперимента**

Spectrum No. in Fig. 4, *c*	Analysis location	Element content												
		%	O	Ni	Fe	Cr	Si	Ba	Mo	Ca	Co	Mn	Al	Ti
1	7–9 μm from the coating interface	wt.	–	9.1	72.7	17.8	0.4	–	–	–	–	–	–	–
2	3–5 μm from the coating interface	wt.	–	11.2	75.6	13.0	0.2	–	–	–	–	–	–	–
3	1–2 μm from the coating interface	wt.	–	19.2	73.1	7.7	–	–	–	–	–	–	–	–
4	At the coating interface	wt.	5.0	18.2	65.4	11.0	–	–	–	–	–	–	–	0.3
5	Intermediate layer based on $FeO\cdot(Cr,Fe)_2O_3$ spinel	at.	56.7	–	14.1	24.3	2.9	1.0	–	0.1	–	–	0.2	0.6
6	Spinel $(Fe,Co,Ni,Mn)O\times$ $\times(Cr,Fe,Mn,Co)_2O_3$ in the glass phase	at.	56.5	1.0	7.6	17.5	6.0	2.6	–	0.4	4.9	3.1	0.5	–
7	Cr_2O_3 particle in the glass phase	at.	59.1	–	–	40.1	0.5	–	–	–	–	–	0.2	–
8	Glass phase at a distance of 3–4 μm from the substrate	at.	60.2	–	6.7	4.4	17.5	7.4	0.2	1.1	0.5	0.4	1.0	0.6
9	Glass phase at a distance of 7–8 μm from the substrate	at.	59.1	0.3	5.2	3.0	19.5	8.3	0.2	1.3	0.7	0.9	1.4	–
10	Glass phase at a distance of 18–20 μm from the substrate	at.	59.9	–	4.5	2.8	20.5	8.6	0.2	1.3	–	0.7	1.5	–
11	Glass phase at a distance of 30–32 μm from the substrate	at.	63.1	–	3.0	0.5	20.6	8.3	0.3	1.3	0.3	0.7	1.9	–

high-temperature oxidation and facilitates self-healing of defects. The presence of refractory Cr_2O_3 particles (melting point T_m = 2708 K), together with the surface crystallization of the glass phase, enhances the coating's resistance to erosion in high-speed gas flows and improves its emissivity.

To evaluate the thermal conductivity and catalytic activity of the coating, an additional gas-dynamic experiment was conducted using a cylindrical sample made of 12Cr18Ni10Ti steel, with a diameter of 50 mm and a height of 30 mm, serving as a calorimeter. A coating with a thickness of 120±5 was applied to the end surface of the sample. Three chromel-alumel (type *K*) thermocouples (TCs) were welded to the side surface of the cylinder at distances of 0.2 mm (TC1), 5.0 mm (TC2), and 14.5 mm (TC3) from the coated end. The sample was placed in a graphite holder with a diameter of 70 mm and a height of 102.5 mm, flush with its end surface, and insulated from it using a spacer made of the thermal protection material quartz TZMK-25, with a diameter of 60 mm and a height of 40 mm. A non-fired coating of the $Si–TiSi_2–MoSi_2–TiB_2–SiO_2$ system [19] was applied to the holder's surface to enhance its oxidation resistance.

The typical fire test conditions for the calorimeter cylinder are presented in Fig. 5 as profiles of brightness temperature (T_b) and thermodynamic temperature (T_w) at the critical point of the front surface (curves *1* and *2*), preheater chamber pressure (P_0, curve *3*), anode power input (W_a, curve 4), and thermocouple readings (TC1, TC2, and TC3; curves *5*–*7*). The figure also includes a photograph of the sample after 7 test cycles conducted under this mode, with a total duration of 25 min. The average values of the specific mass loss and erosion rate of the coating after 7 test cycles were determined to be 2.8 mg/cm^2 and 6.7 mg/(cm^2·h), respectively. The coating retained its performance characteristics.

The thermal conductivity of the coating was determined based on the heat flux through it and the temperature gradient. The thermodynamic surface temperature of the coating was obtained by recalculating the brightness temperature measured by a pyrometer, taking into account the established emissivity of ε = 0.85 at a wavelength of 890 nm. The temperature beneath the coating was determined from the TC1 thermocouple readings, with a correction applied based on its placement. The heat flux through the coating was calculated from the heating rate of the sample. As shown in Fig. 5, the coating demonstrates exceptionally low thermal conductivity under these conditions. The surface temperature of the coating, $T_w \sim 1054\pm10$ K, is reached within the first $\Delta\tau_1 \sim 25$ s from the start of the experiment and remains more than 375 K higher than the substrate temperature even after $\Delta\tau_2 \sim 185$ s of heating. This corresponds to a thermal conductivity value of λ = 0.04±0.01 W/(m·K) at a temperature of $T_w \sim 1054$ K and a pressure of P = 214.8 Pa, which is 30.25 times lower than the value measured at temperatures of 293–573 K and pressure $P = 10^5$ Pa (see Section 2.1). The results demonstrated high reproducibility in subsequent test cycles under identical conditions. To determine the operating parameters and confirm the observed reduction in thermal conducti-

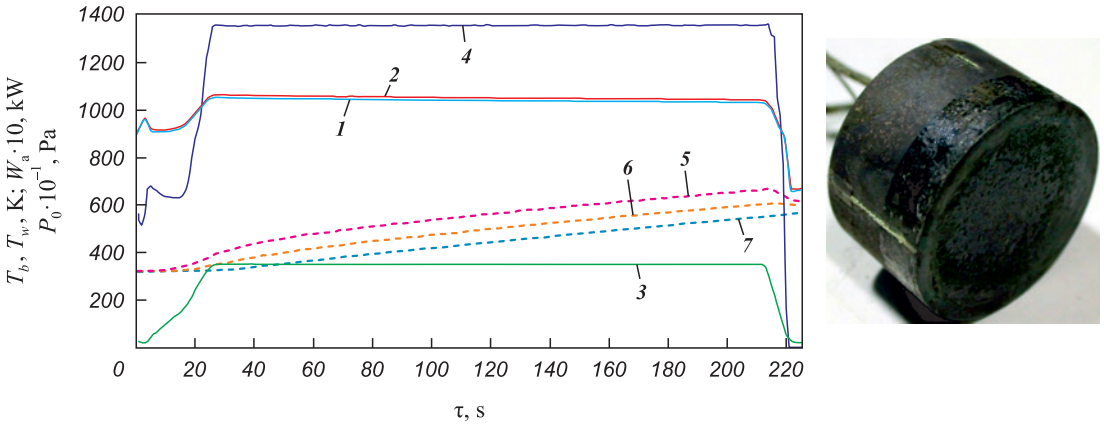

Fig. 5. Results of gas-dynamic tests of calorimeter sample made of 12Cr18Ni10Ti steel with glass-ceramic coating and its appearance after 7 test cycles

1 and ***2*** – brightness (T_b) and thermodynamic (T_w) temperature at the critical point of the coating surface; ***3*** – pressure in the heater prechamber (P_0); ***4*** – anode input power (W_a); ***5***–***7*** – thermocouples readings TC1, TC2 and TC3

Рис. 5. Результаты газодинамических испытаний образца-калориметра из стали 12Х18Н10Т со стеклокерамическим покрытием и его внешний вид после 7 циклов испытаний

1 и ***2*** – яркостная (T_b) и термодинамическая (T_w) температуры в критической точке лицевой поверхности покрытия; ***3*** – давление в форкамере подогревателя (P_0); ***4*** – мощность питания анода (W_a); ***5***–***7*** – показания термопар ТП1, ТП2 и ТП3

vity, a computational simulation was performed (see Section 2.3), with further analysis of the observed effect provided in Section 2.4.

A significant contribution to the heat flux under non-equilibrium exposure to air plasma may be due to the heterogeneous recombination of atoms and ions in the flow. Therefore, catalytic activity is an important property of high-temperature materials and coatings. To assess the catalytic activity of the glass-ceramic coating, a TZMK-25 cylinder with the reference heat-resistant coating EVCh-4M1U was installed alongside the steel calorimeter cylinder in the thermal conductivity measurement setup. Under identical gas-dynamic conditions, the average brightness temperature of the reference coating was 1227 K, while the effective brightness temperature of the tested coating, calculated based on the total heat flux to the steel cylinder, was 1365 K. The heterogeneous recombination rate constant of the glass-ceramic coating, calculated using equation (2), was determined to be $K_w = 14 \pm 3$ m/s. This categorizes the tested coating as moderately catalytic, in contrast to highly catalytic coatings and oxide films in the HfB_2–SiC–HfO_2–ZrO_2–Y_2O_3 system ($K_w = 23$ m/s [20]), ZrO_2–Y_2O_3 ($K_w = 33$ m/s [16]), and HfO_2 ($K_w = 32.5$ m/s [16]). The relatively high K_w value of the tested coating compared to the reference coating ($K_{ws} = 0.1 \div 0.3$ m/s) is attributed to the significant heterogeneity of its structure, characterized by the presence of numerous primary (Cr_2O_3) and secondary ($BaSi_4O_9$) phase particles (see Section 2.1). This structural heterogeneity increases the number of active sites on the coating surface, where recombination of atoms and ions from the plasma flow occurs.

2.3. Numerical simulation of flow around and unsteady heating of the cylinder

To refine the conditions of the fire test, numerical simulation of the flow around and heat transfer of the calorimeter cylinder in the working section of the setup was carried out, taking into account the reaction kinetics of dissociation and exchange processes in an 8-component mixture: O_2, N_2, O, N, NO, O^+, NO^+, e^-. The gas mixture flow was modeled based on the Navier–Stokes equations, which describe the conservation laws of mass, momentum, and energy. It was assumed that the heat flux vector **q** includes three components: the conductive component, governed by Fourier's law, the convective component, caused by shear stress forces, the diffusive component, described as follows:

$$\mathbf{q} = -\lambda \nabla T + \boldsymbol{\tau}\mathbf{V} + \sum_{i=1}^{K} h_i \mathbf{I}_i, \qquad (3)$$

where λ is the thermal conductivity coefficient; **τ** is the viscous stress tensor; **V** is gas velocity vector; h_i is the specific enthalpy of the i-th component, and $\mathbf{I}_i$ is the diffusion flux vector of the i-th component.

The diffusion vector was determined using Fick's law:

$$\mathbf{I}_i = -\rho D_i \nabla g_i, \qquad (4)$$

where D_i is the diffusion coefficient of the i-th component, and g_i is the mass fraction of the i-th component in the mixture.

The continuity equation for the i-th component in the mixture, accounting for mass sources and diffusion, is written as follows:

$$\frac{\partial \rho_i}{\partial t} + \operatorname{div}\left(\rho_i \mathbf{V}\right) = -\operatorname{div}\left(\rho_i \mathbf{I}_i\right) + \omega_i. \qquad (5)$$

Here, ω_i represents the mass formation rate of the component per unit volume due to chemical reactions:

$$\omega_i = M_i \sum_s \left(\nu''_{is} - \nu'_{is}\right)\left[k_{fs}\prod_i \left(\frac{\rho_i}{M_i}\right)^{\nu'_{is}} - k_{rs}\prod_i \left(\frac{\rho_i}{M_i}\right)^{\nu''_{is}}\right], \qquad (6)$$

where ν'_{is}, ν''_{is} are the stoichiometric coefficients of the reactants and products in the s-th chemical reaction.

The reaction rate constants were determined using the Arrhenius equation [21], considering the kinetic scheme presented in Table 3:

$$k_{f(r)} = A_{f(r)} T^{B_{f(r)}} \exp\left(-\frac{C_{f(r)}}{T}\right), \qquad (7)$$

where the subscripts f and r correspond to the forward and reverse reactions, respectively.

The system of equations was closed using the equation of state for the gas mixture:

$$p = \frac{\rho R T}{M}, \; M = \left(\sum_{i=1}^{K} \frac{g_i}{M_i}\right)^{-1}. \qquad (8)$$

The specific static enthalpy of the component is given by:

$$h_1 = \begin{cases} \dfrac{5RT}{2M_i} + h_{0i}, \; i = \mathrm{N}, \mathrm{O}, \mathrm{O}^+, e^-; \\ \dfrac{7RT}{2M_i} + e_{iv} + h_{0i}, \; i = \mathrm{N}_2, \mathrm{O}_2, \mathrm{NO}, \mathrm{NO}^+. \end{cases} \qquad (9)$$

Here, h_{0i} is the specific enthalpy of formation of the i-th component, and e_{iv} is the energy associated with the vibrational degree of freedom:

Table 3. **Kinetic model for an eight-component gas mixture**

Таблица 3. **Кинетическая модель для восьмикомпонентной газовой смеси**

No.	Chemical reaction equation	A_f, $(cm^3/mol)^{n-1}/s$	B_f	C_f, K	A_r, $(cm^3/mol)^{m-1}/s$	B_r	C_r, K
1	$N_2 + N \leftrightarrow N + N + N$	$3.00 \cdot 10^{22}$	–1.60	113 200	$4.351 \cdot 10^{19}$	–1.24	0
2	$N_2 + O \leftrightarrow N + N + O$						
3	$N_2 + N_2 \leftrightarrow N + N + N_2$	$7.00 \cdot 10^{21}$	–1.60	113200	$1.015 \cdot 10^{19}$	–1.24	0
4	$N_2 + O_2 \leftrightarrow N + N + O_2$						
5	$N_2 + NO \leftrightarrow N + N + NO$						
6	$N_2 + e^- \leftrightarrow N + N + e^-$	$1.20 \cdot 10^{25}$	–1.60	113 200	$1.740 \cdot 10^{22}$	–1.24	0
7	$O_2 + N \leftrightarrow O + O + N$	$1.00 \cdot 10^{22}$	–1.50	59 750	$5.856 \cdot 10^{19}$	–1.19	0
8	$O_2 + O \leftrightarrow O + O + O$						
9	$O_2 + N_2 \leftrightarrow O + O + N_2$	$2.00 \cdot 10^{21}$	–1.50	59 750	$1.171 \cdot 10^{19}$	–1.19	0
10	$O_2 + O_2 \leftrightarrow O + O + O_2$						
11	$O_2 + NO \leftrightarrow O + O + NO$						
12	$NO + N \leftrightarrow N + O + N$	$1.10 \cdot 10^{17}$	0	75 500	$2.485 \cdot 10^{15}$	0.27	0
13	$NO + O \leftrightarrow N + O + O$						
14	$NO + NO \leftrightarrow N + O + NO$						
15	$NO + N_2 \leftrightarrow N + O + N_2$	$5.00 \cdot 10^{15}$	0	75 500	$1.129 \cdot 10^{14}$	0.27	0
16	$NO + O_2 \leftrightarrow N + O + O_2$						
17	$NO + O \leftrightarrow N + O_2$	$2.80 \cdot 10^{9}$	1.00	20 000	$1.100 \cdot 10^{10}$	1.00	4000
18	$N_2 + O \leftrightarrow NO + N$	$2.00 \cdot 10^{12}$	0.50	38 000	$4.400 \cdot 10^{11}$	0.50	0
19	$N + O \leftrightarrow NO^+ + e^-$	$2.56 \cdot 10^{12}$	0	32 200	$6.700 \cdot 10^{21}$	–1.50	0
20	$NO^+ + N \leftrightarrow O^+ + N_2$	$3.40 \cdot 10^{13}$	–1.08	12 800	$1.028 \cdot 10^{13}$	–0.88	0
21	$O + e^- \leftrightarrow O^+ + e^- + e^-$	$3.90 \cdot 10^{33}$	–3.78	158 500	$3.686 \cdot 10^{44}$	–5.89	0
22	$NO + e^- \leftrightarrow NO^+ + e^- + e^-$	$6.50 \cdot 10^{23}$	–1.68	107 370	$4.384 \cdot 10^{36}$	–4.11	0
23	$NO^+ + O \leftrightarrow NO + O^+$	$1.82 \cdot 10^{13}$	0	50 130	$1.967 \cdot 10^{12}$	0.12	0

$$e_{iv} = \frac{R\Theta_i}{M_i\left[\exp\left(\frac{\Theta_i}{T}\right)-1\right]}, \quad (10)$$

where Θ_i is the characteristic vibrational temperature of the i-th component molecule.

When calculating the thermodynamic properties of the gas mixture, it was assumed that for each chemical component, thermodynamic equilibrium exists between translational, rotational, and vibrational degrees of freedom of the molecules. The primary temperature dependencies of the gas-dynamic and thermophysical parameters for each component were taken from references [21; 22].

It is worth noting that to reduce computational time and resource consumption, a decoupled approach was used instead of a fully coupled solution for the external flow around and unsteady heating of the solid structure. The effectiveness of this approach has been confirmed in [23].

The study of the external flow around the cylinder with a glass-ceramic coating was carried out using a computational grid of the working section, consisting of approximately 0.3 million cells. Mesh refinement was applied in the near-wall regions and near the outer boundary of the shock layer. A two-dimensional axisymmetric laminar flow of the gas mixture was simulated. At the inlet of the computational domain, the total pressure was set to $P_0 = 4667.7$ Pa. The temperature was selected to match the test conditions, ensuring that the average total temperature in the preheater chamber fell within the range of $T_0 \sim 6000 \div 6500$ K. In the initial approximation, the mass fractions of oxygen and nitrogen were set as follows: $g(O_2) = 0.23$, $g(N_2) = 0.77$. In subsequent calculations, the mass fractions of the components were refined for greater accuracy.

The boundary conditions at the outlet of the computational domain (outlet pressure P_{out}) were set to establish a steady-state flow regime. Radiative heat transfer was applied as a boundary condition on the model surface, with the surface emissivity assumed to be

$\varepsilon = 0.85$, and the external radiation temperature set equal to the wall temperature of the working section, $T_r = 300$ K. The front surface of the model with the glass-ceramic coating was considered catalytic.

The primary calculations were conducted using the ANSYS Fluent software package (TsAGI license No. 501024), in which the described 8-component gas mixture model was implemented. The results of the flow simulation around the cylinder in the working section are shown in Fig. 6. The Mach number ahead of the shock wave reaches M = 4.7, and the plasma speed is 3.54 km/s. A curved shock wave forms at a distance of $\Delta x \sim 17$ mm from the front surface of the cylinder, followed by a transition to subsonic flow, with a specific heat ratio $\gamma = C_p/C_v = 1.29$. The mass fractions of the main components in the incoming flow (at the nozzle exit) are as follows: $g(O_2) = 0.026$; $g(N_2) = 0.727$; $g(O) = 0.135$; $g(N) = 0.023$; $g(NO) = 0.028$; $g(NO^+) = 0.061$; $g(O^+) = 0.325 \cdot 10^{-3}$; $g(e^-) = 1.767 \cdot 10^{-17}$. In front of the model, the gas temperature reaches $T = 5613.2$ K, and the pressure is $P = 214.8$ Pa.

The unsteady heating analysis of the cylinder with a glass-ceramic coating was conducted on a computational grid comprising ~0.9 million cells, with ~0.04 million cells assigned to the coating layer with a thickness of 125 μm.

For the calculation of convective heat transfer to the model surface, a heat transfer coefficient profile was applied:

$$\alpha = \frac{q_w}{T_e - T_{w\max}}, \qquad (11)$$

where q_w and $T_{w\max}$ represent the heat flux density and the surface temperature, respectively, obtained from the external flow simulation. T_e is the temperature at the outer boundary of the boundary layer (considered

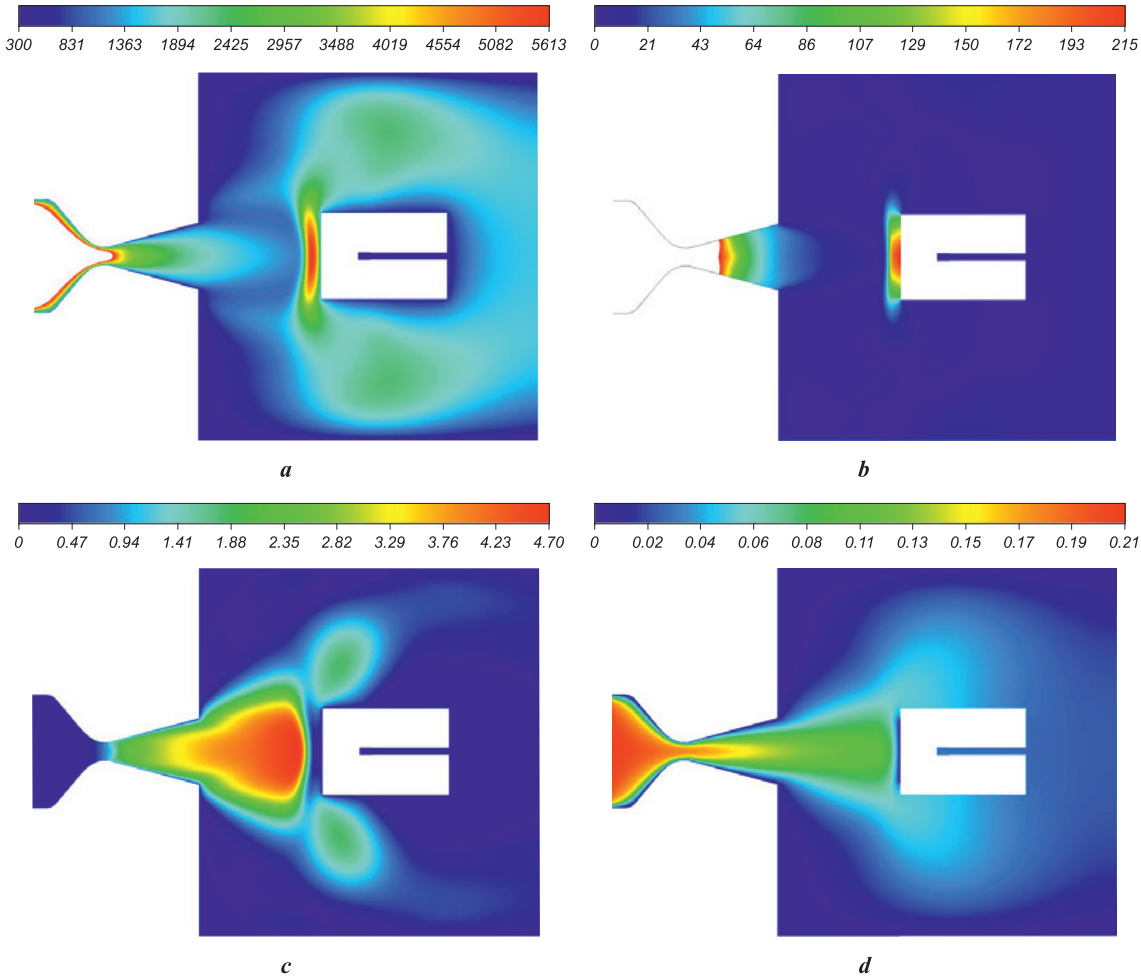

Fig. 6. Main results of the cylinder's external flow calculation

a – static temperature field (T, K); ***b*** – static pressure field (P, Pa);
c – Mach number value field (M); ***d*** – mass fraction value field O

Рис. 6. Основные результаты расчета внешнего обтекания цилиндра

a – поле статической температуры (T, К); ***b*** – поле статического давления (P, Па);
c – поле значений числа Маха (М); ***d*** – поле значений массовой доли О

equal to the adiabatic wall temperature and determined through an additional calculation assuming $q_w = 0$ on the model surface). The radiative heat transfer calculation was performed using the same conditions as in the external flow around simulation. The initial temperature of the entire solid structure (the cylinder with coating and thermal insulation of the lateral surfaces) was set to $T_0 = 291.7$ K.

The thermophysical properties of the cylinder material (12Cr18Ni10Ti steel) were taken from reference data [24]. For the glass-ceramic coating, the experimentally obtained density value $\rho = 3.813$ g/cm^3 and specific heat capacity as a function $C_p = 0.2095T^{0.2006}$ (see Section 2.1) were used. The dependence of the thermal conductivity coefficient on the average temperature across the coating section was adjusted to match the experimentally obtained surface temperature profile and the slope of the temperature curves, which indicate the rate of temperature change at the thermocouple installation points: $\Delta T/\Delta\tau \sim 1.2 \div 1.4$ K/s (see Fig. 5). Additionally, surface temperature calculations were conducted for various values of the thermal conductivity coefficient, including $\lambda = 1.21$ W/(m·K), obtained in Section 2.1 for $T = 293 \div 573$ K at a pressure of $P = 10^5$ Pa.

The key results of the unsteady heating simulation of the coated cylinder are presented in Figs. 7 and 8. During the test (see Fig. 5), it was found that the surface temperature of the cylinder at the front critical point initially rose sharply to $T_w = 1063.5$ K, which is typical for thermal insulation materials, and then gradually decreased to $T_w = 1044.6$ K over $\Delta\tau \sim 185$ s. Based on a series of simulations, the test-obtained surface temperature dependence at the critical point was reproduced (Fig. 7, *a*) by adjusting the thermal conductivity coefficient as a function of the average coating temperature across its thickness. It was shown that during the test, the surface temperature at the critical point slightly decreases, while the average temperature across the coating thickness increases to $T = 840$ K (Fig. 7, *b*). Meanwhile, the thermal conductivity coefficient increases from $\lambda \sim 0.03$ W/(m·K) at $T = 690$ K to $\lambda \sim 0.057$ W/(m·K) at $T = 840$ K (Fig. 7, *c*). The approximation of the computational data allowed for the establishment of the relationship $\lambda = f_1(T)$, presented in Fig. 7, *c*. The increase in thermal conductivity with temperature enables obtaining a monotonically decreasing dependence $T_w = f_2(\tau)$ (Fig. 7, *a*). The calculated temperatures at the thermocouple installation points agree within 5 % with the test results (Fig. 8, *a*). The calculated values of the heat flux density at the front critical point were $q_w = 18.2 \div 18.5$ W/cm^2, which falls within 2 % of the test-measured values.

Fig. 9 presents a comparison of test and calculated results for the evolution of surface temperature at the critical point of the coating for different values of the thermal conductivity coefficient. In each calculation, the thermal conductivity coefficient was assumed to be constant. The simulation results were found to be in good agreement with the test data. It was demonstrated that at $\lambda = 1.21$ W/(m·K), the surface temperature at the front critical point increased only to $T_w \sim 730$ K during the test, which does not align with the test results. Moreover, the rate of temperature change at the thermocouple installation points exceeded the test values by approximately 1.4 times (Fig. 8, *b*).

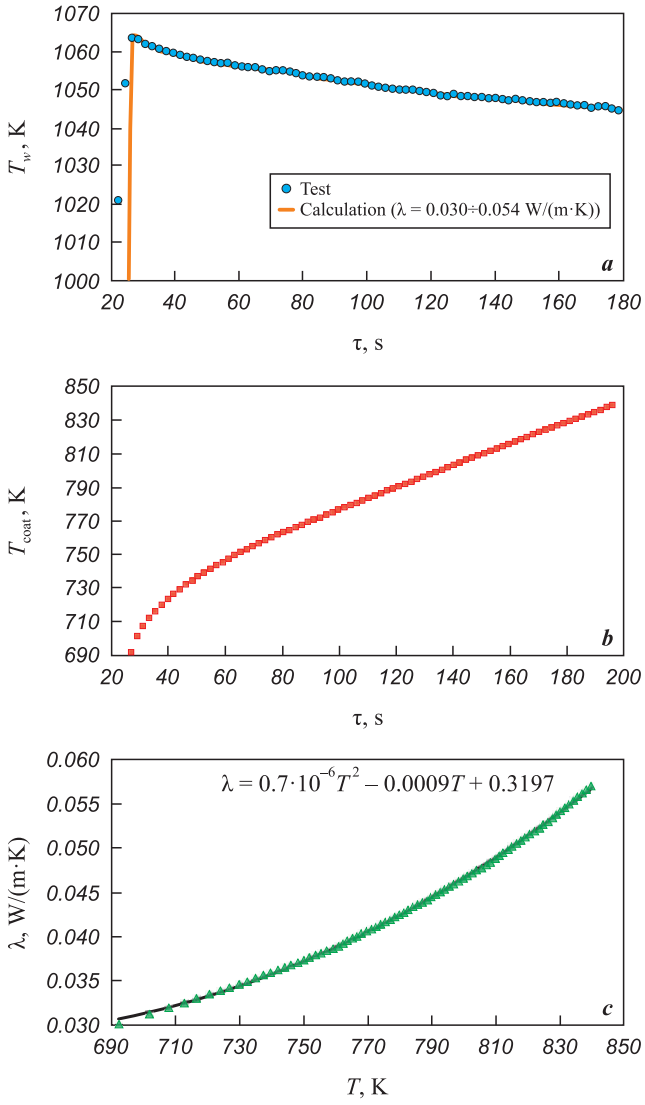

Fig. 7. Results of surface temperature evolution calculation T_w (***a***) and thickness-averaged temperature of the coating T_{coat} (***b***) at the critical point during time; calculated coating's thermal conductivity dependence $\lambda = f_1(T)$ at pressure $P \sim 200$ Pa (***c***)

Рис. 7. Результаты расчета эволюции температуры поверхности T_w (***a***) и средней по толщине температуры покрытия $T_{пок}$ (***b***) в критической точке во времени; расчетная зависимость теплопроводности покрытия $\lambda = f_1(T)$ при давлении $P \sim 200$ Па (***c***)

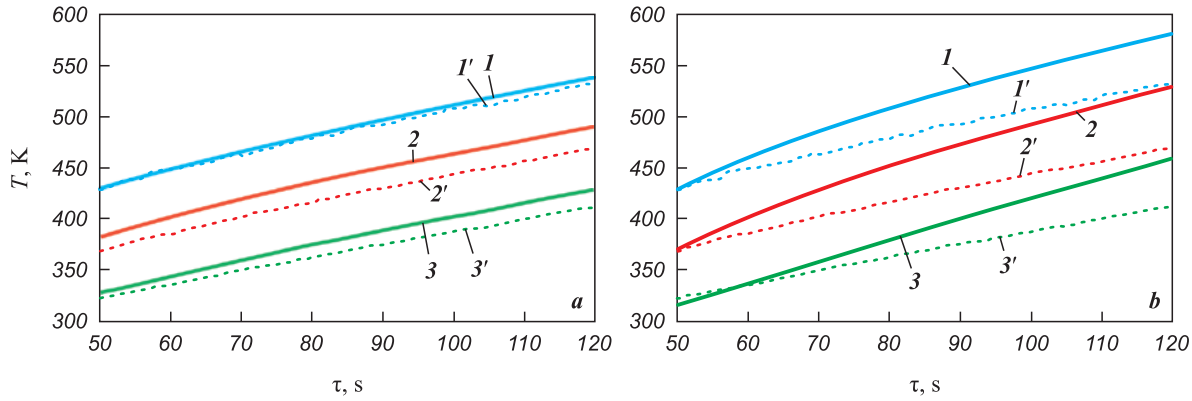

Fig. 8. Comparison of experimental and calculated results of temperature evolution at the thermocouple installation points at different values of the coating's thermal conductivity coefficient: $\lambda = f_1(T)$ (***a***) and λ = 1.21 W/(m·K) (***b***)

1–3 – calculation; ***1′–3′*** – experiment
1, ***1′*** – TC1; ***2***, ***2′*** – TC2; ***3***, ***3′*** – TC3

Рис. 8. Сравнение экспериментальных и расчетных результатов эволюции температуры в точках установки термопар при различных значениях коэффициента теплопроводности покрытия: $\lambda = f_1(T)$ (***a***) и λ = 1,21 Вт/(м·К) (***b***)

1–3 – расчет; ***1′–3′*** – эксперимент
1, ***1′*** – ТП1; ***2***, ***2′*** – ТП2; ***3***, ***3′*** – ТП3

Thus, numerical simulation of the gas-dynamic test confirmed that at low pressures ($P \sim 200$ Pa), a significant reduction in the thermal conductivity of the glass-ceramic coating occurs. The obtained thermal conductivity values of $\lambda = 0.030 \div 0.057$ W/(m·K) were observed within the temperature range $T = 690 \div 840$ K and the average value of thermal conductivity coefficient, determined during the test $\Delta\tau \sim 185$ s, was $\lambda \sim 0.04$ W/(m·K), which is in full agreement with the test-derived value (see Section 2.2).

2.4. Effect of reduced thermal conductivity with decreasing pressure

The thermal conductivity of the glass-ceramic coating is primarily determined by atomic thermal vibrations, known as the phonon transport mechanism. A decrease in thermal conductivity occurs as the phonon mean free path is reduced due to phonon scattering at structural defects, such as impurity atoms,

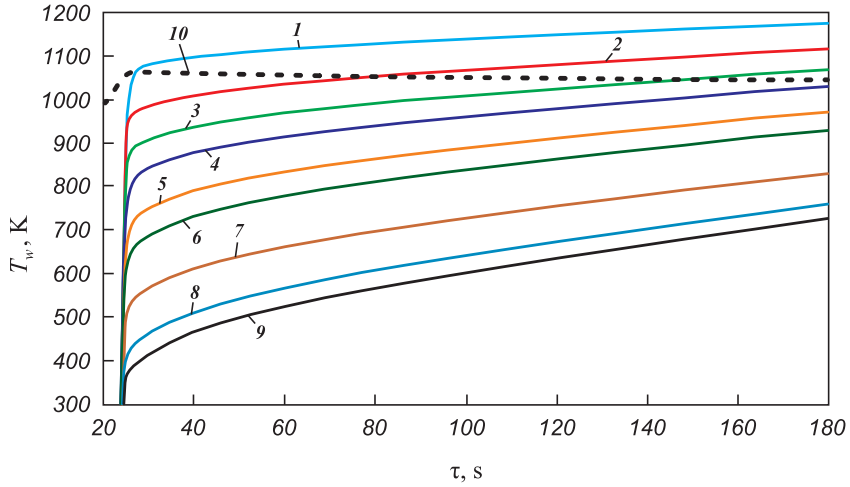

Fig. 9. Calculated and experimental cylinder-calorimeter surface temperatures evolution results comparison at different values of the thermal conductivity coefficient of the glass-ceramic coating

1–9 – calculation; ***10*** – experiment
λ, W/(m·K): 0.03 (***1***); 0.04 (***2***); 0.05 (***3***); 0.06 (***4***); 0.08 (***5***); 0.10 (***6***); 0.20 (***7***); 0.50 (***8***); 1.21 (***9***)

Рис. 9. Сравнение расчетных и экспериментальных результатов эволюции температуры поверхности цилиндра-калориметра при различных значениях коэффициента теплопроводности стеклокерамического покрытия

1–9 – расчет; ***10*** – эксперимент
λ, Вт/(м·К): 0,03 (***1***); 0,04 (***2***); 0,05 (***3***); 0,06 (***4***); 0,08 (***5***); 0,10 (***6***); 0,20 (***7***); 0,50 (***8***); 1,21 (***9***)

grain boundaries, phase interfaces, and voids, as well as interactions with other phonons. As temperature increases, phonon-phonon interactions intensify, and in combination with the highly disordered (amorphous) structure of the glass phase, this results in extremely short phonon mean free paths. When external pressure decreases, the phonon mean free path is further shortened due to the reduced propagation velocity of acoustic waves resulting from the lower density of the medium.

In the presence of structural inhomogeneities, such as pores, voids, and cracks, the thermal conductivity of dielectrics is influenced not only by the phonon mechanism but also by convective gas transport within these discontinuities. The extent of convection is strongly dependent on the distribution and geometry of the discontinuities, as well as the thermal conductivity of the enclosed gas. The convective effect diminishes with decreasing discontinuity size, reduced interconnectivity, and lower surrounding gas pressure.

The investigated coating contains voids with sizes up to ~5–10 μm (see Fig. 1). It is known [25] that at low pressures ($P < 10^3$ Pa), when the mean free path of gas particles l is much greater than the void size L ($l \gg L$), the thermal conductivity of porous materials is proportional to the gas pressure, increases with rising temperature, and approaches zero as pressure decreases. This phenomenon is likely due to the fact that when $l \gg L$, gas particles remain adsorbed on the surface of the voids for a long period before experiencing collisions. As pressure decreases, the number of gas particles in the voids is reduced, and an increasing fraction of them becomes adsorbed on the void surfaces, leading to a decrease in the convective component of heat transfer. At temperatures above 1200 K, radiative heat transfer in discontinuities should also be considered, as its contribution to overall thermal conductivity increases with temperature. It should be noted that in the fire tests conducted to determine the thermal conductivity of the glass-ceramic coating, the pressure at the sample surface was $P \sim 200$ Pa, and the temperature $T_w \sim 1050$ K, satisfying the condition $l \gg L$. This, combined with the reduced phonon mean free path, explains the extremely low thermal conductivity of the coating.

A threefold reduction in thermal conductivity (from 0.05 to 0.0167 W/(m·K) at 293 K) with a decrease in external pressure (from 10^5 to 133.3 Pa) was previously observed during tests of the highly porous quartz thermal protection material TZMK-10 [26]. The explanation of this observed effect is presented here for the first time.

The conducted studies of the glass-ceramic coating have enabled its application in thermal testing of various steel models in the TsAGI aerodynamic wind tunnels [27]. The high and stable emissivity of the coating over time enhances the accuracy of temperature measurements of models using optical methods under illumination conditions. The coating's heat and erosion resistance slow down oxidation processes, reduce mechanical erosion, and prevent the formation of corrosion-erosion pitting and cavities on model surfaces, which further contributes to the improved accuracy of conducted studies and measurements.

Conclusion

A thin-layer heat-resistant glass-ceramic coating was obtained on 12Cr18Ni10Ti steel samples using the slurry-firing deposition method. The coating exhibits a heterogeneous structure, consisting of a barium silicate glass matrix with uniformly distributed Cr_2O_3 particles. In the outer layer of the coating, with a thickness of approximately 3–5 μm, numerous highly dispersed $BaSi_4O_9$ crystals doped with Cr and Mo were identified, indicating surface crystallization of the glass phase. The coating is characterized by a low density of 3.813 g/cm^3 and a highly continuous structure. The heat capacity, thermal diffusivity, and thermal conductivity of the coating within the temperature range of 293–573 K and at a pressure of 10^5 Pa vary within the ranges of 0.68–0.75 J/(g·K), 0.47–0.43 mm^2/s, and 1.198–1.222 W/(m·K), respectively.

Fire tests of the coating were conducted under conditions of aerogas-dynamic flow and non-equilibrium heating by air plasma at a speed of approximately 3.5 km/s and a specific heat flux of 15–30 W/cm^2, achieving temperatures of up to 1593 K on the front surface. The average values of specific mass loss and erosion rate of the coating were 7.2 mg/cm^2 and 25.9 mg/(cm^2·h), respectively. The spectral emissivity of the coating at a wavelength of 890 nm and the heterogeneous recombination rate of atoms and ions on its surface were determined to be 0.85±0.02 and 14±3 m/s, respectively. The glass phase effectively protects the steel from high-temperature oxidation and facilitates self-healing of defects. The presence of refractory Cr_2O_3 particles, along with the surface crystallization of the glass phase, enhances the coating's resistance to erosion in high-speed air plasma flow, its emissivity, and catalytic activity.

A reduction in the coating's thermal conductivity to 0.04±0.01 W/(m·K) at a temperature of 1054±10 K and a pressure of ~200 Pa was experimentally established and confirmed by numerical simulation. An explanation of this effect has been provided.

References / Список литературы

1. Zakalashniy A.V., Denisova V.S., Kulikova O.V., Agarkov A.B. Polyfunctional heat-resistant coating for protecting corrosion-resistant steel parts. *Glass and Ceramics*. 2024;80:404–408. https://doi.org/10.1007/s10717-023-00623-4

   Закалашный А.В., Денисова В.С., Куликова О.В., Агарков А.Б. Жаростойкое полифункциональное покрытие для защиты деталей из коррозионно-стойких сталей. *Стекло и керамика*. 2023;96(10):3–9. https:/doi.org/10.14489/glc.2023.10.pp.003-009
2. Fu G.Y., Wei L.Q., Zhang X.M., Cui Y.B., Lv C.C., Ding J., Yu B., Ye S.F. A high-silicon anti-oxidation coating for carbon steel at high temperature. *Surface and Coatings Technology*. 2017;310:166–172. https://doi.org/10.1016/j.surfcoat.2016.12.084
3. Terentieva V.S., Astapov A.N., Rabinskiy L.N. State in the field of heat-resistant coatings for heat-proof nickel alloys and steels. *Periodico Tche Quimica*. 2019;16(33):561–572. http://dx.doi.org/10.52571/PTQ.v16.n33.2019.576_Periodico33_pgs_561_572.pdf
4. Solntsev S.S. Protective technological coatings and refractory enamels. Moscow: Lenand, 2016. 304 p. (In Russ.).

   Солнцев С.С. Защитные технологические покрытия и тугоплавкие эмали. М.: Ленанд, 2016. 304 с.
5. Aviation materials: Handbook. In 12 vol. Vol. 9. Heat-protective, thermal insulation and composite materials, high-temperature non-metallic coatings. Ed. E.N. Kablov. Moscow: VIAM, 2011. 176 p. (In Russ.).

   Авиационные материалы: Справочник. В 12 т. Т. 9. Теплозащитные, теплоизоляционные и композиционные материалы, высокотемпературные неметаллические покрытия. Под ред. Е.Н. Каблова. М.: ВИАМ, 2011. 176 с.
6. Denisova V.S., Vlasova O.V., Malinina G.A. Effect of the addition of silicon tetraboride on the thermal stability of reaction cured coatings. *Aviation Materials and Technologies*. 2020;59(2):50–55. (In Russ.). https://doi.org/10.18577/2071-9140-2020-0-2-50-55

   Денисова В.С., Власова О.В., Малинина Г.А. Влияние добавки тетраборида кремния на термостойкость реакционноотверждаемых покрытий. *Авиационные материалы и технологии*. 2020;59(2):50–55. https://doi.org/10.18577/2071-9140-2020-0-2-50-55
7. Bettridge D. Metallic article having a protective coating and a method of applying a protective coating to a metallic article: Patent 6444332 (USA). 2002.
8. Solntsev S.S., Isaeva N.V., Shvagireva V.V., Solov'eva G.A. Heat-resistant coating: Patent 2273609 (RF). 2006. (In Russ.).

   Солнцев С.С., Исаева Н.В., Швагирева В.В., Соловьева Г.А. Жаростойкое покрытие: Патент 2273609 (РФ). 2006.
9. Solov'eva G.A., Grashchenkov D.V., Isaeva N.V., Shvagireva V.V. Heat-resistant coating: Patent 2358925 (RF). 2009. (In Russ.).

   Соловьева Г.А., Гращенков Д.В., Исаева Н.В., Швагирева В.В. Жаростойкое покрытие: Патент 2358925 (РФ). 2009.
10. Hazel B.T., Murphy J.A., Skoog A.J., Bojanowski B.T., Weimer M.J. Strain tolerant corrosion protecting coating and spray method of application: Patent 7754342 (USA). 2010.
11. Kablov E.N., Solntsev S.S., Rozenenkova V.A., Denisova V.S. Heat-resistant cover: Patent 2598657 (RF). 2016. (In Russ.).

    Каблов Е.Н., Солнцев С.С., Розененкова В.А., Денисова В.С. Жаростойкое покрытие: Патент 2598657 (РФ). 2016.
12. Miller T.J., Pinera A., Brooks S.M., Appleby Jr. J.W., Leonard T.G. Turbopump with a single piece housing and a smooth enamel glass surface: Patent 2017/0082070 (USA). 2017.
13. Lima R.S., Cojocaru C.V., Moreau C., Wang Y. Method and apparatus for depositing stable crystalline phase coatings of high temperature ceramics: Patent 2014/0329021 (USA). 2014.
14. Russell J.C., White T.L., Shiflett B., Cherinet P., Wadley S., Barnhart C., Khozikov V., Nakamoto K. Nanocoating thermal barrier and method for making the same: Patent 2576864 (EP). 2018.
15. Astapov A.N., Barabanov B.N., Eremina A.I., Lifanov I.P. Method of producing heat-resistant glass-ceramic coating: Patent 2679774 (RF). 2019. (In Russ.).

    Астапов А.Н., Барабанов Б.Н., Еремина А.И., Лифанов И.П. Способ получения жаростойкого стеклокерамического покрытия: Патент 2679774 (РФ). 2019.
16. Astapov A.N., Zhestkov B.E., Senyuev I.V., Shtapov V.V. Methodology of studying high-velocity plasma flow impact on high-temperature materials. *AIP Conference Proceedings*. 2023;2549(1):210009. https://doi.org/10.1063/5.0109458
17. Zhestkov B.E., Shtapov V.V. Methodology of studying materials in hypersonic plasma flow. *Zavodskaya laboratoriya. Diagnostika materialov*. 2016;82(12):58–65. (In Russ.).

    Жестков Б.Е., Штапов В.В. Исследование состояния материалов в гиперзвуковом потоке плазмы. *Заводская лаборатория. Диагностика материалов*. 2016;82(12):58–65.
18. Hazen R.M., Yang H., Finger L.W., Fursenko B.A. Crystal chemistry of high-pressure $BaSi_4O_9$ in the trigonal (P3) barium tetragermanate structure. *American Mineralogist*. 1999;84:987–989. https://doi.org/10.2138/am-1999-5-636
19. Astapov A.N. Heat-resistant non-fired repair coatings for protection of carbon-base materials. *International Journal of Nanomechanics Science and Technology*. 2014;5(4):267–285. https://doi.org/10.1615/NanomechanicsSciTechnolIntJ.v5.i4.20
20. Kablov E.N., Zhestkov B.E., Grashchenkov D.V., Sorokin O.Yu., Lebedeva Yu.E., Vaganova M.L. Investigation of the oxidative resistance of high-temperature coating on a SiC material under exposure to high-enthalpy flow. *High Temperature*. 2017;55(6):873–879. https://doi.org/10.1134/S0018151X17060086
21. Gupta R.N., Yos J.M., Thompson R.A., Lee K.-P. A review of reaction rates and thermodynamic and transport

properties for the 11-species air model for chemical and thermal nonequilibrium calculations to 30 000 K. NASA Reference Publication. 1990;1232. 91 p.

22. McBride B.J., Gordon S., Reno M.A. Coefficients for calculating thermodynamic and transport properties of individual species. NASA Technical Memorandum. 1993;4513. 94 p.

23. Drozdov S.M., Rtishcheva A.S. Analysis of flow-field and heat exchange for a blunted cone at hypersonic speeds. *Journal of Physics: Conference Series*. 2020;1683:022030. http://doi.org/10.1088/1742-6596/1683/2/022030

24. Steel and alloy brand book: Handbook. Ed. V.G. Sorokin. Moscow: Mashinostroenie, 1989. 640 p. (In Russ.).

Марочник сталей и сплавов: Справочник. Под ред. В.Г. Сорокина. М.: Машиностроение, 1989. 640 с.

25. Physical quantities: Handbook. Eds. I.S. Grigor'ev, E.Z. Meilikhov. Moscow: Energoatomizdat, 1991. 1232 p. (In Russ.).

Физические величины: Справочник. Под ред. И.С. Григорьева, Е.З. Мейлихова. М.: Энергоатомиздат, 1991. 1232 с.

26. Shchetanov B.V. Tile material for external high-temperature thermal protective coating of the Buran orbital spacecraft. *Aviation Materials and Technologies*. 2013;S1:41–50. (In Russ.).

Щетанов Б.В. Материал плитки для внешнего высокотемпературного теплозащитного покрытия орбитального корабля «Буран». *Авиационные материалы и технологии*. 2013;S1:41–50.

27. Rtishcheva A.S. Application of numerical modeling to determine heat flux on the surface of bodies in a thermal experiment. In: *Models and methods of aerodynamics*: Proceedings of the XXII International school-seminar (Sochi, 4–9 September 2022). Moscow: TsAGI, 2022. P. 70–72. (In Russ.).

Ртищева А.С. Применение численного моделирования для определения теплового потока на поверхности тел в тепловом эксперименте. В сб.: *Модели и методы аэродинамики*: Материалы XXII международной школы-семинара (г. Сочи, 04–09 сентября 2022 г.). М.: ЦАГИ, 2022. С. 70–72.

Information about the Authors

Alexey N. Astapov – Cand. Sci. (Eng.), Associate Professor of the Department of Advanced Materials and Technologies for Aerospace Application, Researcher, Moscow Aviation Institute (National Research University)
ORCID: 0000-0001-8943-2333
E-mail: lexxa1985@inbox.ru

Boris E. Zhestkov – Cand. Sci. (Eng.), Senior Researcher, Head of Laboratory, Central Aerohydrodynamic Institute named after professor N.E. Zhukovsky (TsAGI)
E-mail: bzhestkov@mail.ru

Alena S. Rtishcheva – Cand. Sci. (Eng.), Associate Professor, Head of Sector, TsAGI
E-mail: al.rtisheva@mail.ru

Сведения об авторах

Алексей Николаевич Астапов – к.т.н., доцент кафедры «Перспективные материалы и технологии аэрокосмического назначения», науч. сотрудник, Московский авиационный институт (национальный исследовательский университет)
ORCID: 0000-0001-8943-2333
E-mail: lexxa1985@inbox.ru

Борис Евгеньевич Жестков – к.т.н., ст. науч. сотрудник, начальник лаборатории, Центральный аэрогидродинамический институт им. профессора Н.Е. Жуковского (ЦАГИ)
E-mail: bzhestkov@mail.ru

Алена Сергеевна Ртищева – к.т.н., доцент, начальник сектора, ЦАГИ
E-mail: al.rtisheva@mail.ru

Contribution of the Authors

A. N. Astapov – formation of the basic concept, setting the goal and objectives of the research, conducting structural studies, determination of thermophysical properties, critical analysis of the results, article text preparation, formulation conclusions.
B. E. Zhestkov – preparing, conducting and analysing the results of gas-dynamic experiments.
A. S. Rtishcheva – formulation of the model, numerical solution construction, analysis of the results of computational experiment, article text preparation.

Вклад авторов

А. Н. Астапов – формирование основной концепции, постановка цели и задач исследования, проведение структурных исследований, определение теплофизических свойств, критический анализ результатов, подготовка текста статьи, формулировка выводов.
Б. Е. Жестков – подготовка, проведение и анализ результатов газодинамических экспериментов.
А. С. Ртищева – формулировка модели, построение численного решения, анализ результатов вычислительного эксперимента, подготовка текста статьи.

Received 06.12.2024
Revised 26.12.2024
Accepted 27.12.2024

Статья поступила 06.12.2024 г.
Доработана 26.12.2024 г.
Принята к публикации 27.12.2024 г.

Application of Powder Materials and Functional Coatings
Применение порошковых материалов и функциональных покрытий

UDC 620.193 : 622.692.4.07
https://doi.org/10.17073/1997-308X-2025-1-58-74

Review article
Обзорная статья

Functional coatings of submersible oilfield equipment for protection against corrosion, asphalt, resin, paraffin and salt deposits: Review

P. E. Yudin[1, 2]

[1] **LLC "SPC "Samara"**
3B Garazhny Proezd, Samara 443022, Russia
[2] **Samara State Technical University**
133 Molodogvardeiskaya Str., Samara 443001, Russia

yudin@npcsamara.ru

Abstract. The oil production process is often accompanied by various failures at oil production facilities, which leads to serious economic losses. Failures in oil production systems not only increase repair and maintenance costs, but also lead to loss of productivity, which has a negative impact on the economic efficiency of projects. A pipeline failure is considered to be its complete or partial shutdown due to a violation of its tightness or tightness of the shut-off valves, or due to blockage of the flow section. The most common causes of complications in oil production are: corrosion of oil and gas equipment, formation of asphalt-resin-paraffin deposits (ARPD) and inorganic salt deposits on the working surface of oil and gas equipment. There are a large number of methods aimed at preventing each of the previously mentioned complicating factors. It is noteworthy that the use of protective coatings can be a measure of prevention of corrosion processes, ARPD, and inorganic salt deposits. This article will review the literature, which will consider what properties, composition and structure protective coatings should have to prevent corrosion, ARPD and salt deposits, as well as what testing methods can be used to evaluate the ability of a protective coating to prevent these complicating factors.

Keywords: protective coatings, types of coatings, corrosion, asphalt-resin-paraffin deposits, salt deposits, coating testing methods

For citation: Yudin P.E. Functional coatings of submersible oilfield equipment for protection against corrosion, asphalt, resin, paraffin and salt deposits: Review. *Powder Metallurgy and Functional Coatings*. 2025;19(1):58–74.
https://doi.org/10.17073/1997-308X-2025-1-58-74

Функциональные покрытия погружного нефтепромыслового оборудования для защиты от коррозии, асфальтосмолопарафиновых и солевых отложений: Обзор

П. Е. Юдин[1, 2]

[1] **ООО «НПЦ «Самара»**
Россия, 443022, г. Самара, Гаражный проезд, 3Б
[2] **Самарский государственный технический университет**
Россия, 443001, г. Самара, ул. Молодогвардейская, 133

yudin@npcsamara.ru

Аннотация. Процесс извлечения нефти часто сопровождается различными отказами на объектах нефтедобычи, что ведет к серьезным экономическим потерям. Отказы в системах нефтедобычи не только увеличивают затраты на ремонт и обслуживание, но также приводят к потере производительности, что негативно сказывается на экономической эффективности

проектов. Отказом трубопровода считается полная или частичная его остановка вследствие нарушения его герметичности или герметичности запорной арматуры, либо по причине закупорки проходного сечения. Наиболее распространенными причинами осложнений в нефтедобыче являются коррозия нефтегазового оборудования и образование асфальтосмолопарафиновых отложений (АСПО) и неорганических солеотложений на рабочей поверхности нефтегазового оборудования. Среди большого количества методов, направленных на предотвращение указанных осложняющих факторов, весьма эффективно применение защитных покрытий, которое может являться мерой профилактики и коррозионных процессов, и АСПО, и неорганических солеотложений. В настоящей статье проведен обзор литературных источников: рассмотрено, какими методами испытаний можно оценить способность защитного покрытия предотвращать возможные осложняющие факторы.

Ключевые слова: защитные покрытия, виды покрытий, коррозия, асфальтосмолопарафиновые отложения, солеотложения, методы испытания покрытий

Для цитирования: Юдин П.Е. Функциональные покрытия погружного нефтепромыслового оборудования для защиты от коррозии, асфальтосмолопарафиновых и солевых отложений: Обзор. *Известия вузов. Порошковая металлургия и функциональные покрытия*. 2025;19(1):58–74. https://doi.org/10.17073/1997-308X-2025-1-58-74

Introduction

Oil and gas fields are gradually entering the late stage of development, which is accompanied by increasing complexity in operational processes [1; 2]. At this stage, the risks of equipment failures rise significantly due to a number of factors specific to this phase of the field's lifecycle. Various complicating factors act jointly and interdependently at oilfields. However, each well typically has one dominant complication type, which serves as the primary cause of most failures. The distribution of so-called complicated wells across different production companies by their main complication type provides valuable insights into the scale and actual prevalence of corrosion-related issues within the industry.

The structure of complicated wells at LLC RN-Purneftegaz includes only 18 % of wells prone to the formation of asphalt-resin-paraffin deposits (ARPD), 13 % of wells where failures are caused by salt deposits, and only 6 % of wells where corrosion is the primary complication. It is important to note that the number of failures related to corrosion significantly decreased only after the implementation of corrosion-resistant pipes; however, it still remains high [3]. At Udmurtneft PJSC, corrosion accounts for 39 % of well failures [4]. A substantial number (26 %) of Udmurtneft's wells are affected by ARPD, while 1 % of the wells experience complications due to inorganic salt deposits [4]. As of early 2022, the complicated well stock of PJSC Lukoil included 14,271 wells, representing 45 % of all operating artificial lift wells [5]. The structure of Lukoil's complicated well stock consists of 74.8 % of wells affected by ARPD, 9.5 % by corrosion, and 3.8 % by inorganic salt deposits [5].

Corrosion is a fundamental issue in any industry dealing with chemically active environments. In oil and gas production, its consequences include the irreversible loss of pipe metal [6], costs associated with equipment replacement, lost profits due to well downtime during repairs, as well as expenses related to mitigating accident consequences and maintenance of corrosion protection systems. All these factors increase production costs and reduce field profitability.

Globally, corrosion results in substantial direct and indirect financial losses [7–9]. In Russia, annual metal losses due to corrosion amount to 12 % of the country's total metal reserves, which is equivalent to the same share of the annual steel production. Approximately 10 million tons out of the 70 million tons produced annually are lost to corrosion, which translates into financial losses of USD 8 billion. Nationwide, 400,000–500,000 tons of steel are used annually to replace various types of pipelines [6].

Complications associated with the formation of ARPD [10–13] and inorganic salt deposits are no less significant, as they lead to partial or complete blockages of the internal pipe cross-section, resulting in reduced production rates or even cessation of oil extraction [14–16].

The most effective solution to combat these types of complications today is the application of various functional coatings – polymeric, ceramic, and metallization – depending on the type of equipment being protected [17].

This article reviews the application of various functional coatings for oil and gas equipment aimed at counteracting complicating factors.

Functional internal coatings for tubing

Tubing (TBG) is one of the key components of submersible oilfield equipment, susceptible to corrosion, asphalt-resin-paraffin deposits (ARPD), and salt deposits on its inner surface, which is in direct contact with the extracted medium. The housings of submersible electric motors (SEM) and electric submersible pumps (ESP) are exposed to the extracted media from their external surface. It should be noted that cases of contact

between the medium and the external surface of tubing are possible; however, on the one hand, such occurrences are rare, and on the other hand, the only available method of protection against corrosion in such cases is the use of alloyed corrosion-resistant steels.

Currently, there is no established classification system for internal tubing corrosion protection methods. Therefore, the author has proposed a classification (Fig. 1) that summarizes various approaches – ranging from traditional steel alloying to the development of duplex coatings [18; 19], which combine sacrificial and barrier properties.

Austenitic stainless steel tubing is not manufactured due to its extremely high cost combined with relatively low strength properties [20]. However, this class of steel has found its application in the production of liners (thin-walled internal metal tubes) used in bimetallic pipes [21]. The installation of liners in production and tubing pipes can be performed using several methods; however, currently, only two methods have been implemented in Russia [22–24]. In both cases, the first step involves inserting a liner with a diameter smaller than the internal diameter of the tubing. The liner is secured by mechanical interference through roller expansion [25] or by a hydraulic method [26]. In both methods, the gap between the liner and the tubing is eliminated, and the resulting interference fit ensures a stable liner position under all permissible operational loads. In large-diameter pipes (used for trunk oil and gas pipelines), a metallurgical method is applied, forming a diffusion transition zone between the metals.

Various austenitic stainless steels with different chemical compositions can be used for this technology. The most commonly used steels are AISI 304, being the most cost-effective in this class; however, their corrosion resistance is often insufficient for highly mineralized environments. In such cases, more highly alloyed steels such as AISI 316, 316L, or 825 are required.

The advantages of this technology include the relatively low cost of tubing with liners compared to pipes made entirely from liner material; the ability to achieve near-absolute corrosion resistance by selecting an appropriate liner material; and the absence of temperature limitations typical for polymer coatings. However, the disadvantages of this technology include higher costs compared to low-alloy steel pipes, low efficiency if the liner material is improperly selected, lack of reliable methods for protecting the annular space of couplings at pipe ends, and an increase in tubing string weight by 8–11 %.

It is also important to highlight the risk of pitting corrosion in austenitic steels when exposed to environments with high chloride ion (Cl^-) content. Fig. 2 shows an example of the operation of a tubular component made from AISI 316 steel as part of a pipeline transporting seawater. The corrosion rate of the component was 12.8 mm/year. This phenomenon is most likely to occur due to β-phase precipitation, such as during cold plastic deformation. Before operating in such environments, it is mandatory to conduct pitting corrosion resistance testing in ferric chloride solution according to GOST 9.912–89.

Bimetallic pipes with an internal liner can be considered a specialized type of coated pipe, with the liner serving as a protective barrier. The mechanism by which the liner provides protection is similar to that

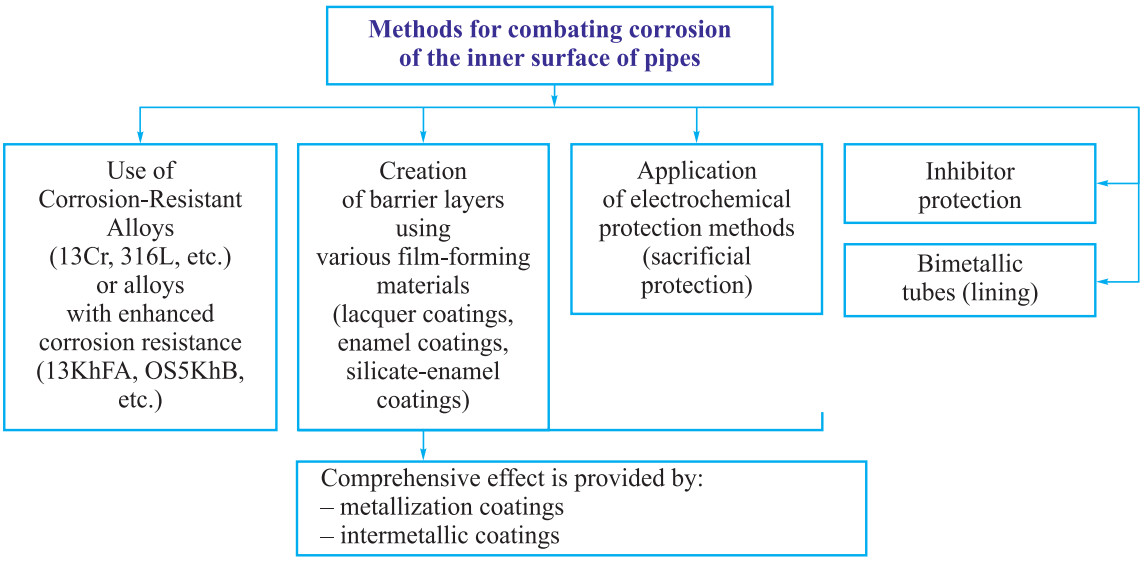

Fig. 1. Classification of methods for combating corrosion on the inner surface of tubing strings

Рис. 1. Классификация методов борьбы с коррозией внутренней поверхности насосно-компрессорных труб

of conventional coatings, resulting in comparable performance requirements for both. Based on an analysis of liner steel corrosion, manufacturing technologies, and operational factors, GOST 70926–2023, "Tubing with Internal Liner. Technical Specifications", was developed under the author's supervision. Pipes produced in accordance with this standard have been in trouble-free operation across Russia for more than three years. Their use commenced even before the official publication of GOST 70926–2023, following the completion of research and development activities that formed the basis for the standard. Condition monitoring has shown no signs of corrosion damage to the liner. The service life of these pipes is primarily constrained by factors such as length reduction due to repeated thread cutting, external surface corrosion, and mechanical damage.

The most commonly used corrosion-resistant steels are alloyed with chromium in concentrations of 13 % or more. According to Schaeffler's rule, their protection mechanism is based on the formation of a passive chromium oxide film on the surface, which is resistant to interaction with corrosive gases dissolved in the produced fluid. Traditionally, Cr13-grade steel pipes are considered the benchmark for corrosion resistance; however, their widespread adoption is limited by their high cost. Certain factors significantly reduce the service life of such pipes and lead to premature failure, all of which are associated with the degradation of the passive layer. Since the produced fluid lacks oxygen, repassivation is not possible. The operational limitations of Cr13-grade pipes include the following: acid treatments, mechanical wear (including erosion), and cable insulation failure. In the presence of hydrogen sulfide in the well and acid treatments, sulfide stress corrosion cracking (SSCC) may occur [27; 28], which is typical for low-alloy steels with a hardness exceeding 22 HRC.

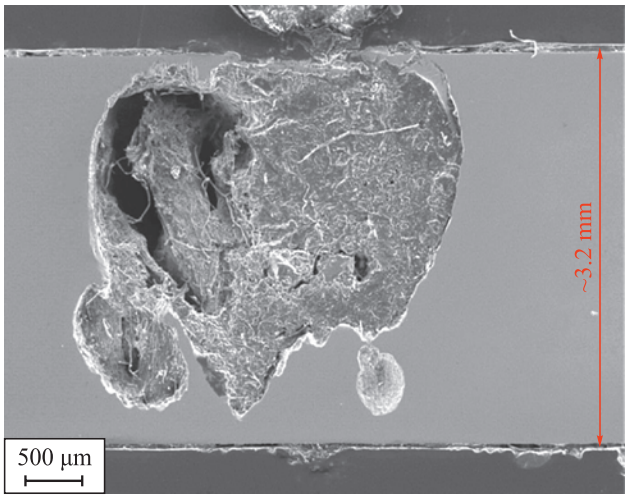

C	Si	Mn	Cr	Ni	S	P	Cu	Mo
0.03	0.51	1.77	16.8	9.19	0.05	0.01	0.43	1.80

Fig. 2. Longitudinal section of the tubular component wall made of AISI 316 steel after 3 months of operation as part of a seawater pipeline

Рис. 2. Продольное сечение стенки трубчатого изделия из стали AISI 316 после 3 месяцев эксплуатации в составе трубопровода морской воды

The term "steel with enhanced corrosion resistance" was introduced in Russia in the mid-2000s. This class includes steels alloyed with 0.5–1.0 % Cr, often with the addition of niobium or vanadium to refine the grain structure, as well as copper. However, according to GOST 5272–50, these steels are classified as low-alloy and are not considered corrosion-resistant (it is worth noting that the later and currently relevant edition, GOST 5272–68, does not include a corrosion resistance scale, nor is the term "steel with enhanced corrosion resistance" mentioned in other regulatory documents). The experience of their implementation has been mixed, and given their relatively high cost, they are not considered an optimal solution [29].

The optimal solution for protecting the inner surface of tubing from complicating factors is the use of various functional coatings [17; 30; 31]. Despite the wide variety of available coatings, in practice, only silicate-enamel (SEC), polymer, and duplex (intermetallic layer + polymer layer) coatings are commonly applied.

Silicate-enamel coatings are formed from a slurry prepared using frits of MK-5 and MK-5U grades with the following composition (wt. %): 0.5–3.5 Al_2O_3; 10.0–16.0 B_2O_3; 8.0–16.0 Na_2O; 0.5–5.0 K_2O; 2.0–5.0 Li_2O; 2.0–8.0 CaO; 0.1–1.0 MgO; 3.0–6.0 TiO_2; 0.5–5.0 MnO_2; 0.3–2.0 NiO; 0.2–2.0 CuO; 0.3–1.5 CoO; 0.1–1.5 Fe_2O_3; and 0.5–4.0 F (in excess of 100 %). The coating can be applied using either a liquid or powder method, followed by firing at temperatures ranging from 850 to 950 °C. During the firing process, gases are released, which, upon cooling, result in the formation of porosity, often characterized by through-pores.

Despite their excellent resistance to ARPD formation, the use of tubing with silicate-enamel coatings (SEC) in the oil and gas industry has been declining, with the total volume not exceeding several thousand tons as of 2024. This reduction is attributed to several significant limitations:

– through-pore porosity in single-layer coatings (Fig. 3), which leads to severe pitting corrosion beneath the pores;

– high brittleness, which imposes restrictions on mechanical impacts and thread tightening torque; exceeding these limits can result in enamel chipping, particularly in the nipple area at the pipe ends;

– heat curing requirements at 850–950 °C, which prevent the use of heat-treated steel pipes, as such temperatures degrade their mechanical properties;

– higher costs compared to polymer coatings, primarily due to the need for high-temperature processing.

Advancements in polymer coatings, particularly the development of multifunctional coatings that combine anti-corrosion properties with resistance to ARPD formation, have largely negated the advantages of tubing with silicate-enamel coatings.

At present, the primary method for protecting the inner surface of tubing from complicating factors is the application of polymer coatings [32–35]. Their widespread adoption began in the early 2000s with the emergence of manufacturers such as MajorPack and Hilong. Although several production lines existed in Russia before this period, their products were not widely used. In the early stages of development, various film-forming coatings were applied, such as the polyurethane-based PolyPlex coating. However, it demonstrated an extremely short service life (typically less than 30 days), leading to its swift abandonment within the industry.

Polymer coatings offer several advantages over other protective methods against complicating factors. They provide extended service life for equipment and pipelines by protecting against corrosion and wear, significantly prolonging operational lifespan and reducing repair and replacement costs. Maintenance costs are also lower, as polymer coatings minimize the need for frequent servicing and repairs. Additionally, they enhance oil production and transportation efficiency by reducing friction, preventing deposits such as ARPD and inorganic salts, and improving thermal insulation,

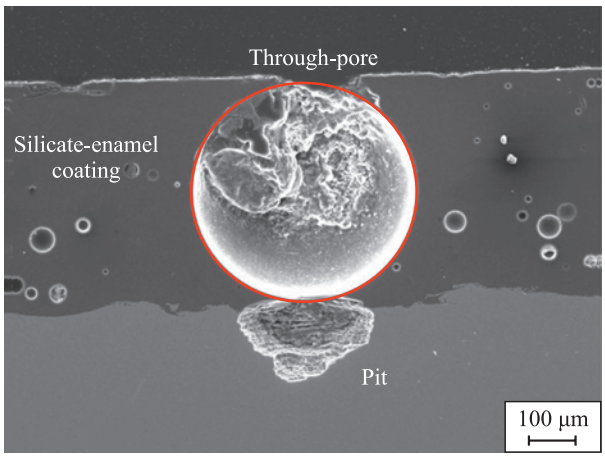

Fig. 3. Formation of pitting corrosion through the mechanism of carbon dioxide corrosion in a silicate-enamel coating

Рис. 3. Образование язвы по механизму углекислотной коррозии в силикатно-эмалевом покрытии

which leads to greater system performance. The risk of failures is reduced, as effective corrosion and wear protection helps prevent breakdowns associated with equipment deterioration. Furthermore, polymer coatings offer significant cost savings by extending service life and decreasing maintenance and repair expenses. Lastly, they provide environmental benefits by reducing emissions and leaks through improved corrosion resistance and enhanced equipment protection [36; 37].

The classification of coatings used to protect the inner surface of tubing is shown in Fig. 4.

There are several methods for applying internal polymer coatings, with the most commonly used being airless spraying and electrostatic application. The airless spraying method applies liquid coatings to the surface without the use of an air stream. Instead, high pressure forces the material through a nozzle, breaking it into fine droplets that uniformly coat the surface. This technique provides higher efficiency and better application quality compared to conventional air spraying and allows for the application of high-viscosity coatings with 100 % solids content. Electrostatic application, on the other hand, involves applying a layer of polymer powder to the product's surface using an electrostatic field. In this process, the polymer particles are electrically charged and attracted to the surface, which has an opposite charge, ensuring a uniform and durable coating [38].

Initially, the effectiveness of internal coatings was questioned, as early applications utilized cold-cured epoxy resins based on Bisphenol A and epoxy novolac resin in an approximate 2:1 ratio (Fig. 5). The fillers and pigments commonly used in these coatings included micronized barite ($BaSO_4$), aerosil (fumed silica, SiO_2), titanium dioxide (TiO_2), and talc ($Mg_3Si_4O_{10}(OH)_2$). Their concentrations varied depending on the formulation, but the total filler content typically did not exceed 50 %. These coatings exhibited relatively low glass transition temperatures (usually below 60 °C), limited chemical resistance, and restricted operating temperature ranges. They were applied using dual-component airless spray systems.

The degradation of pipes with the aforementioned type of coatings (Fig. 6), as evidenced by more than 40 expert studies conducted under the author's supervision, highlights the low barrier properties of these coatings. The service life before the onset of blistering and delamination typically does not exceed 2–3 years for field pipelines. The use of such coatings for tubing protection is viable only at relatively low temperatures (up to 40 °C) and in cases where complications are limited to ARPD. Even under these conditions, their service life rarely exceeds 1 year.

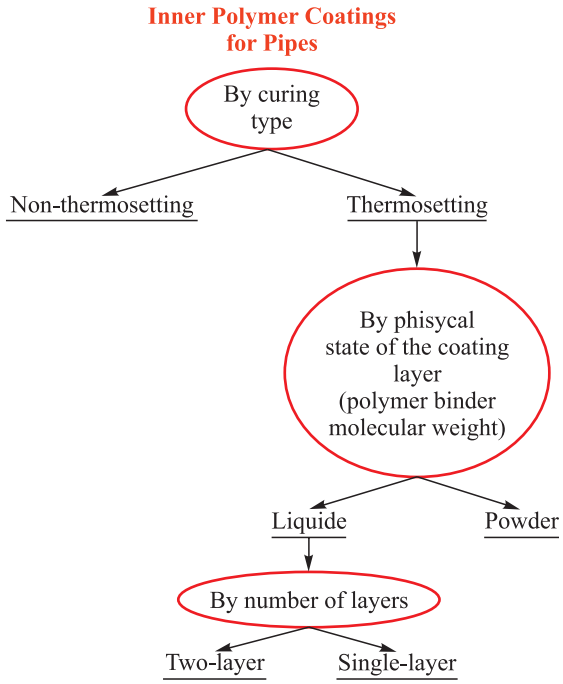

Fig. 4. Classification of polymer coatings used to protect the inner surface of tubing

Рис. 4. Классификация полимерных покрытий, применяющихся для защиты внутренней поверхности НКТ

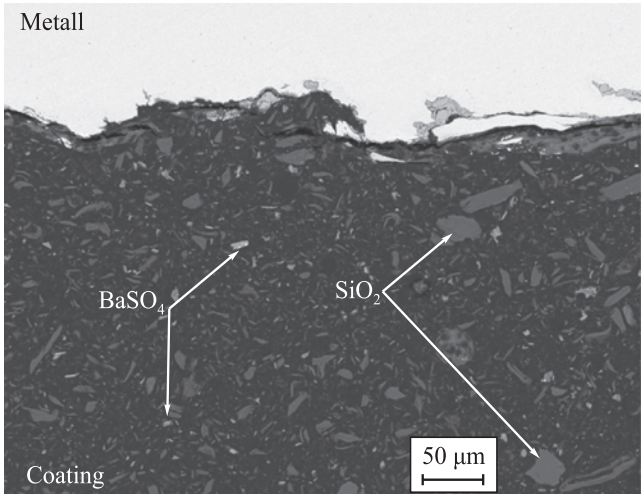

Fig. 5. Structure of a typical liquid non-thermosetting internal epoxy coating for an oil pipeline

Рис. 5. Структура типичного жидкого нетермоотверждаемого внутреннего эпоксидного покрытия нефтепроводной трубы

The liquid thermosetting epoxy novolac coating (its structure shown in Fig. 7) stands apart from other coatings due to its higher concentration of novolac resin, with an epoxy novolac resin to Bisphenol A-based resin

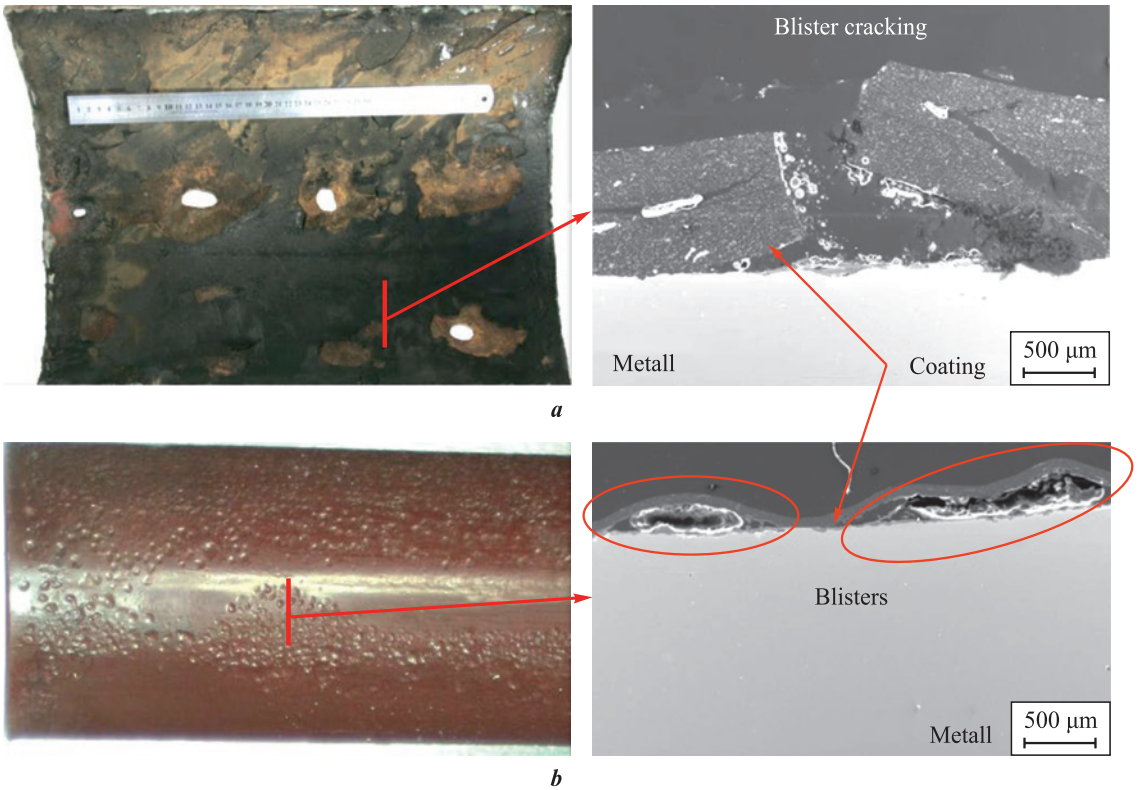

Fig. 6. Degradation of liquid non-thermosetting internal epoxy coatings used in ∅426×8 mm oil collection manifold at the Mamontovskoe field (***a***) and ∅73×5.5 mm production tubing at the Krapivinskoe field (***b***)

Рис. 6. Разрушение жидких нетермоотверждаемых внутренних эпоксидных покрытий, эксплуатировавшихся в составе нефтесборного коллектора ∅426×8 мм Мамонтовского месторождения (***a***) и добывающей скважины НКТ ∅73×5,5 мм Крапивинского месторождения (***b***)

ratio of ≥1:1, and the inclusion of a reactive diluent. This diluent lowers the viscosity of the epoxy composition, facilitating easier processing while also participating in the curing reaction and becoming an integral part of the polymer matrix. The application process is similar to that of non-thermosetting liquid epoxy coatings, with the key difference being the requirement for an isothermal curing hold at 180–200 °C for at least 20 min.

This type of coating is the most commonly used for tubing protection, as it delivers the required performance characteristics at relatively small thicknesses (~150 μm). It also enables the application of two-layer coatings, allowing for formulation optimization at smaller production facilities. The industry-wide use of these coatings is estimated to be 85–90 %.

In the past three years, two-layer powder coatings have been increasingly adopted, consisting of a primer layer with a thickness of 5–40 μm and a top layer of ≥350 μm made from a powder composite material (Fig. 8). The primer is a paint-and-lacquer material composed of a blend of high-molecular-weight epoxy and phenol-formaldehyde resins, butyl cellosolve, toluene, and, in most cases, iron oxide pigment, which actively reacts with hydrogen sulfide during operation or testing. The powder coating is applied electrostatically to a preheated surface at a temperature of 160–200 °C. Its composition includes high-molecular-weight epoxy resin and a significant amount of fillers (up to 70 %), with a composition similar to those described earlier. This technology offers several advantages, including superior barrier properties, lower costs compared to other protective methods, high process efficiency and maintainability, and the ability to apply multifunctional coatings.

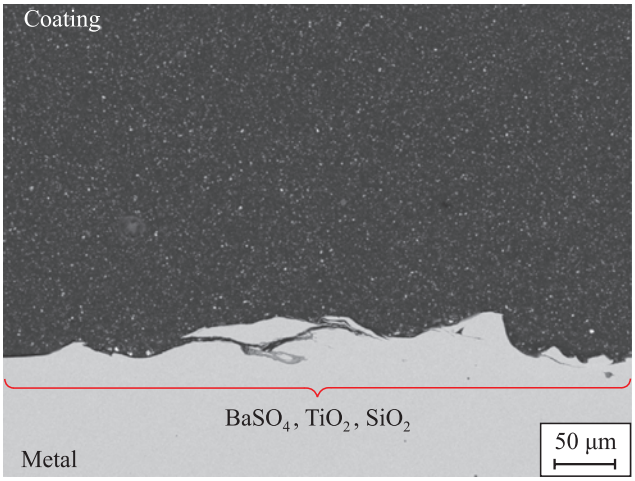

Fig. 7. Structure of a typical liquid thermosetting internal epoxy coating for an oil pipeline

Рис. 7. Структура типичного жидкого термоотверждаемого внутреннего эпоксидного покрытия нефтепроводной трубы

Additionally, the absence of solvent evaporation during application makes this method more environmentally friendly and safer for production workers, which is why it is the only permitted option in most countries. The production volume of tubing with internal functional coatings is expected to exceed 100,000 tons by the end of 2024 (based on the weight of ∅73×5.5 mm tubing) and continues to grow at a rate of 8–12 % per year.

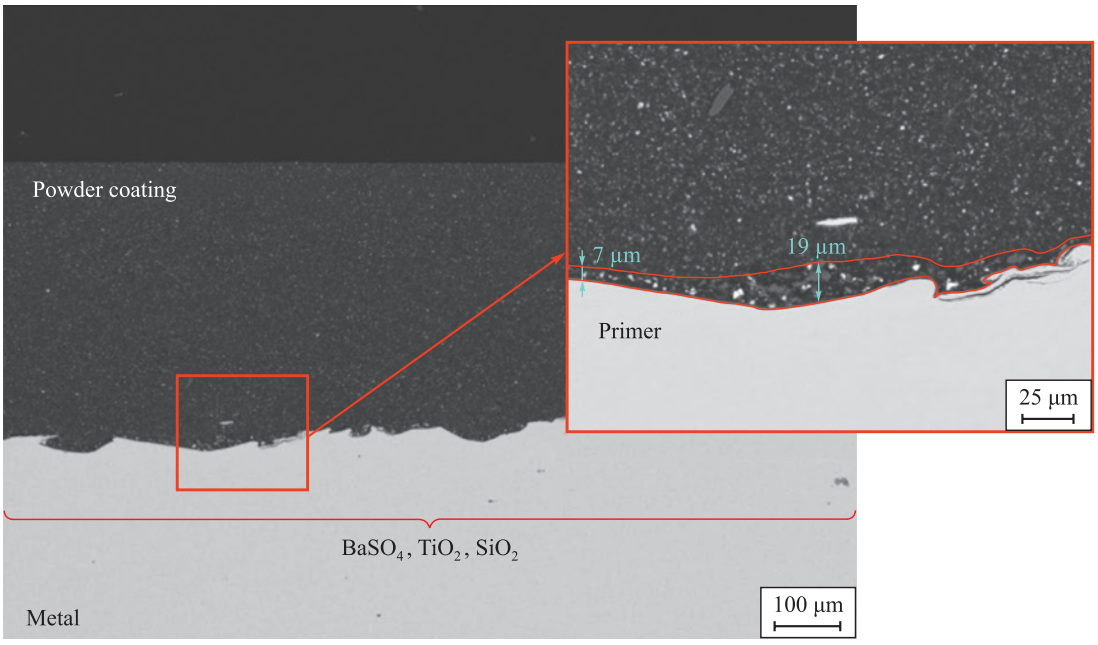

Fig. 8. Structure of a typical two-layer powder coating with an epoxy-phenolic primer

Рис. 8. Структура типичного двухслойного порошкового покрытия с эпоксифенольным праймером

A relatively new technological solution is the use of duplex coatings, where the first layer consists of thermodiffusion zinc (TDZ), forming Fe–Zn intermetallic compounds, followed by one or more polymer layers [39]. These coatings demonstrate higher corrosion resistance in hydrogen sulfide-containing environments, as confirmed by laboratory autoclave exposure tests conducted over 2352 h, compared to the standard test duration of 240 h specified by GOST 58346–2019. The test involved exposing samples with two types of coatings in an autoclave under a partial gas pressure of H_2S – 1 MPa, N_2 – 9 MPa at a temperature of 80 °C. The results showed the presence of iron sulfide at the metal-coating interface in pipes without the TDZ layer, whereas no corrosion products were detected on duplex-coated pipes (Fig. 9). It should be noted that the autoclave testing methods used in this experiment and outlined in GOST 58346–2019 are based on previous research [40; 41]. The widespread adoption of autoclave testing methods has led to a significant increase in the service life of tubing with internal coatings. Although exact statistical data is not publicly available, sources accessible to the author indicate that the average service life has increased from 418 to 786 days. However, the disadvantages of duplex coatings include higher costs compared to conventional polymer-coated pipes and the limited availability of reliable solutions for protecting the external surface from corrosion.

A key trend in the development of tubing with internal coatings is the creation of multifunctional coatings that combine anti-corrosion and anti-abrasion properties while also preventing ARPD and inorganic salt deposition [42–45]. Until recently, advancements in coating formulations and application technologies – such as the introduction of non-thermal microwave treatment [46] – were limited by the lack of standardized laboratory testing methods. The applicability of each coating was primarily determined through field pilot tests (FPT), which typically take about one year to complete.

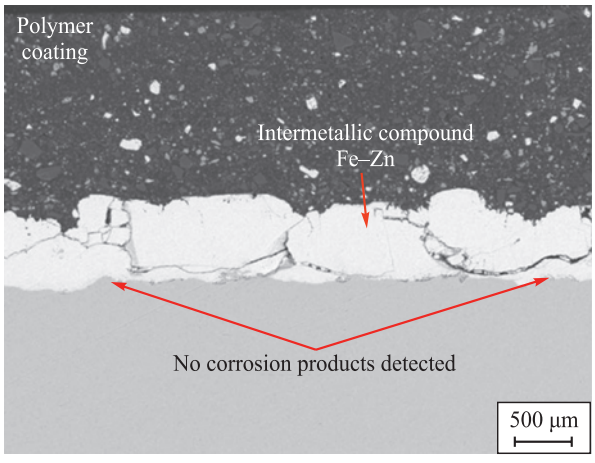

Fig. 9. Surface condition of the metal–intermetallic layer (Fe–Zn) after an autoclave test for 2352 h

Рис. 9. Состояние поверхности «металл–интерметаллидный слой (Fe–Zn)» после автоклавного теста в течение 2352 ч

To address the challenge of simulating ARPD formation under controlled conditions, two circulating test benchs were developed and manufactured under the author's supervision [47; 48]. The test medium used in these test benches is an oil emulsion sampled from wells affected by ARPD, further enriched with deposits obtained during cleaning operations. The design of the test benches allows for adjustments in the composition of the test medium, flow rate, medium temperature, and the external surface temperature of the sample. The temperature difference across the inner surface of tubing samples – used as test specimens – facilitates the formation of deposits. The capabilities of these benches cover a wide range of well conditions, from low- to high-production wells, with varying temperature regimes influencing ARPD formation.

Research findings indicate that parameters such as surface roughness, paraffin adhesion to a dry surface, and the contact angle of distilled water on a dry surface do not provide a reliable assessment of a surface's resistance to ARPD deposition. The laboratory method for determining the contact angle by measuring the spreading of an oil droplet in water on the coating surface has shown the highest correlation with test bench results [49]. The best ARPD resistance results were demonstrated by hydrophilic surfaces; however, they exhibited poor corrosion resistance. Therefore, the use of multifunctional coatings or two-layer systems is required to achieve balanced performance.

Experimental studies have established a correlation between ARPD deposition and flow rate (Reynolds number), allowing for the ranking of coatings based on their resistance to ARPD. Silicate-enamel coatings provide the highest resistance, followed by polymer coatings, while bare steel samples show the lowest performance (Fig. 10). The obtained results align with data from field pilot tests and the operational performance of these coating types across various oilfields.

Another important step in expanding the application of functional polymer coatings was the development of a test bench (Patent No. RU2825169C1) and a methodology to evaluate the effectiveness of coatings in preventing inorganic scale formation [50]. The goal of the test trials was to identify the coating with the highest resistance to scaling under oilfield conditions. The coatings' resistance to scaling was assessed based on the mass of inorganic scale formed

on the outer surfaces of cylindrical samples and the thickness of the resulting scale layer.

The results of the test trials evaluating the resistance of coatings to gypsum-type ($CaSO_4$) scale formation with halite (NaCl) impurities were published in [51]. It was found that none of the tested protective coatings could completely prevent the formation of gypsum scale with halite impurities on their surface. The study [51] also concluded that the adhesion strength of the "scale–coating" interface does not play a decisive role in the anti-scaling properties of protective coatings. The findings showed that scale deposits can form even on surfaces with minimal adhesion strength. These deposits are capable of creating solid structures with little to no interaction with the surface. Further analysis in [52] compared the results of the test trials [51] with the roughness parameters of the tested protective coatings to evaluate the effect of surface roughness on scaling. A certain correlation was observed between the coating's roughness index and the mass of the scale layer formed on it. The steel sample with the highest surface roughness exhibited the most significant increase in the scale layer mass during dynamic tests. However, the relationship between surface roughness and scale formation mass was not strictly linear [52].

Since studies [51] and [53] both found that none of the examined coatings could completely prevent scale formation, further research focused on assessing the combined use of coatings with other preventive methods. In study [54], laboratory-scale dynamic tests were conducted to evaluate the feasibility of integrating internal protective tubing coatings with scale inhibitors. The findings showed that the combined approach can provide the following benefits:

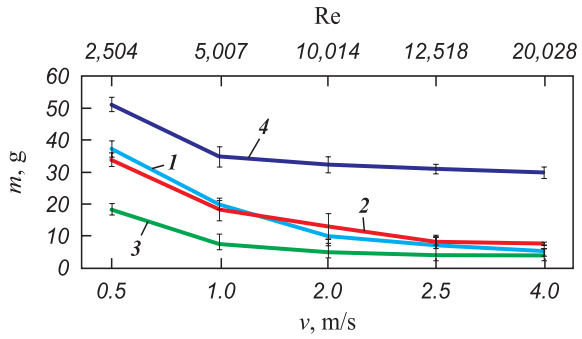

Fig. 10. Dependence of asphaltene-resin-paraffin deposit mass on the flow rate of the oil medium on various surfaces

1 – GIOTEK 110M, ***2*** – MPLAG17,
3 – silicate enamel MK-5, ***4*** – uncoated

Рис. 10. Зависимость массы выпадения АСПО от скорости потока нефтяной среды на различных поверхностях

1 – ГИОТЭК 110М, ***2*** – MPLAG17,
3 – силикатно-эмалевое МК-5, ***4*** – без покрытия

– coated surfaces had fewer crystallization centers for inorganic scale deposits compared to uncoated steel surfaces;

– during testing (with a scale inhibitor dosage of 200 g/m^3), the formed scale deposits detached more readily from the coated samples [54].

Coating of SEM and ESP housings

Various corrosion protection methods are employed to mitigate the corrosive impact and extend the service life of submersible electric motors (SEM) and electric submersible pumps (ESP). (Hereinafter, the discussion will focus solely on SEM housings; however, all conclusions are equally applicable to ESP housings.) One of the simplest and most cost-effective ways to enhance the service life of SEM housings while reducing exposure to aggressive factors under field conditions is the application of metallization coatings. Among the most widely used methods for applying such coatings are electric arc spraying (EAS) and high-velocity oxy-fuel (HVOF) spraying [55–60].

An analysis of the causes of SEM and ESP housing failures was conducted under the author's supervision in four oil-producing regions with various complicating factors. The study revealed that corrosion of the SEM housing is the most common cause of failure [61–63]. The examination of SEM housings with metallization coatings applied using technologies implemented at pipe bases after operation allowed the identification of key causes of failure, including mechanical damage, abrasive wear of the coating, low barrier properties, and imperfections in the coating application technology (Fig. 11). Additionally, cases were identified where multiple negative factors were simultaneously present, making it impossible to determine the dominant failure mechanism. In many cases, these factors create a synergistic effect – for example, the simultaneous presence of a corrosive environment and abrasive particles results in corrosion-erosion wear, which occurs at a significantly higher rate compared to either corrosion or erosion alone [61].

The primary challenge in ensuring the operational reliability of SEM housings was the development of methodologies that simulate the effects of key complicating factors and conducting laboratory tests on various types of metallization coatings. The results, summarized in [61], onfirm the feasibility of accurately modeling the destructive impact of key complicating factors through autoclave tests in H_2S- and CO_2-containing environments [64; 65]. To determine the corrosion resistance of metallization coatings, samples must undergo autoclave exposure for 240 h. Testing typically involves the combined exposure

to aggressive gases (CO_2, H_2S). In order to isolate the corrosion effects of individual system components, tests can also be conducted in environments saturated with only carbon dioxide or hydrogen sulfide. To prevent decompression effects, pressure release must take at least 10 min [64].

Electric arc spraying (EAS) was selected as the primary coating application method due to its high process efficiency and equipment mobility. EAS coatings made of stainless steel materials based on iron and nickel were applied with a target thickness of 350–500 µm. The chemical composition of the metallization coatings included various elements in specific proportions (wt. %):

– Cr ~ 6.6÷14.5; Ni ~ 4.4÷8.4; Mo ~ 2.5; Si ~ 2.0÷3.7; Fe – balance;

– Cr ~ 13.0÷16.0; Ni ~ 7.3÷9.8; Mo ~ 3.5; Si ~ 2.9÷3.7; Al ~ 1.0; Fe – balance;

– Cr ~ 17.7÷18.6; Ni ~ 8.5÷8.9; Ti ~ 0.6; Si ~ 0.5÷0.7; Fe – balance.

The physical and mechanical properties of EAS coatings were found to be low due to significant porosity and oxide layers between particles. Metallization coatings applied using iron-based wires (Fig. 12, *a*) without additional impregnation or an external polymer layer proved to be ineffective against corrosive environments. In contrast, nickel-based wire coatings (Fig. 12, *b*) demonstrated resistance in acidic environments but lacked sufficient protection against CO_2- and H_2S-saturated conditions, indicating their inability to provide long-term protection. To reduce particle oxidation during spraying, an argon protective atmosphere was used (Fig. 12, *c*, *d*), which resulted in a 55 % improvement in physical and mechanical properties compared to coatings applied in open air; however, corrosion resistance remained unsatisfactory [66].

Impregnation materials are commonly used to seal coating pores [67; 68]. The study utilized polymer-based impregnating materials, including epoxy-phenolic, acrylic, and polytetrafluoroethylene compositions with thicknesses of 70–150 µm. The application of impregnation materials improved the corrosion resistance of the metallization layer; however, even minor damage to the impregnated coating on iron-based layers resulted in rapid degradation. Therefore, the use of iron-based coatings with impregnation was deemed impractical.

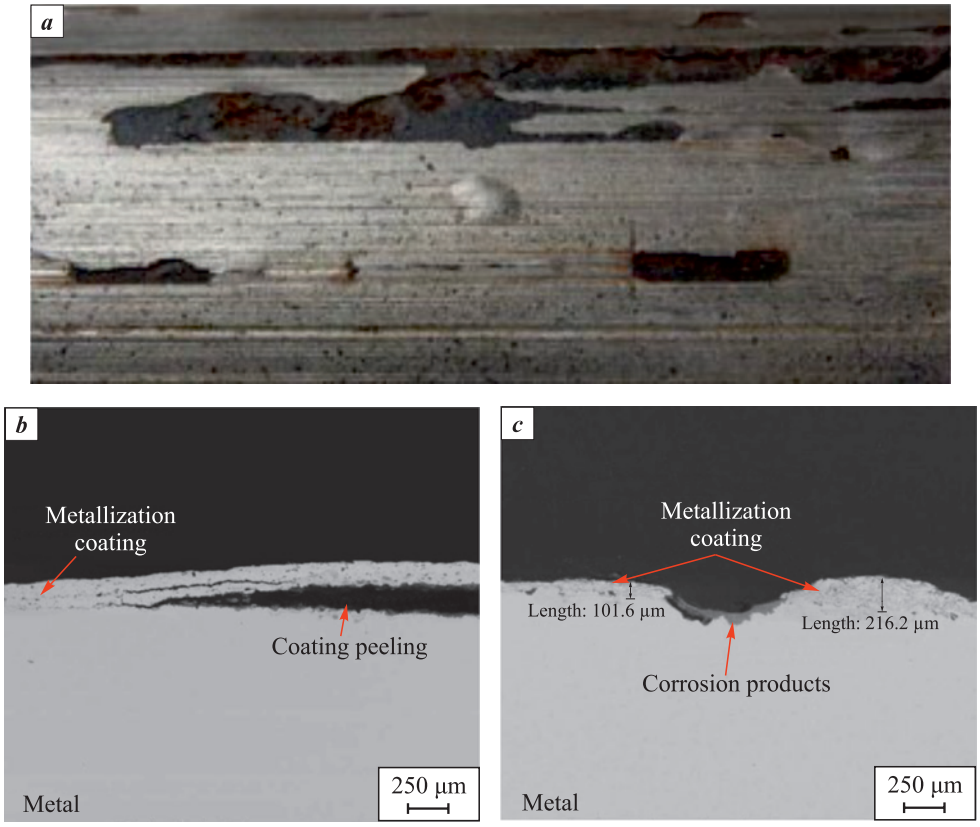

Fig. 11. External view of the SEM housing with peeling and blistering of the metallization coating (***a***); destruction in the form of swelling of the coating (***b***); formation of corrosion products at the site of local damage to the coating (***c***)

Рис. 11. Внешний вид корпуса ПЭД с отслоениями и вздутиями металлизационного покрытия (***a***); разрушение в виде вздутия покрытия (***b***); образование продуктов коррозии в месте локального повреждения покрытия (***c***)

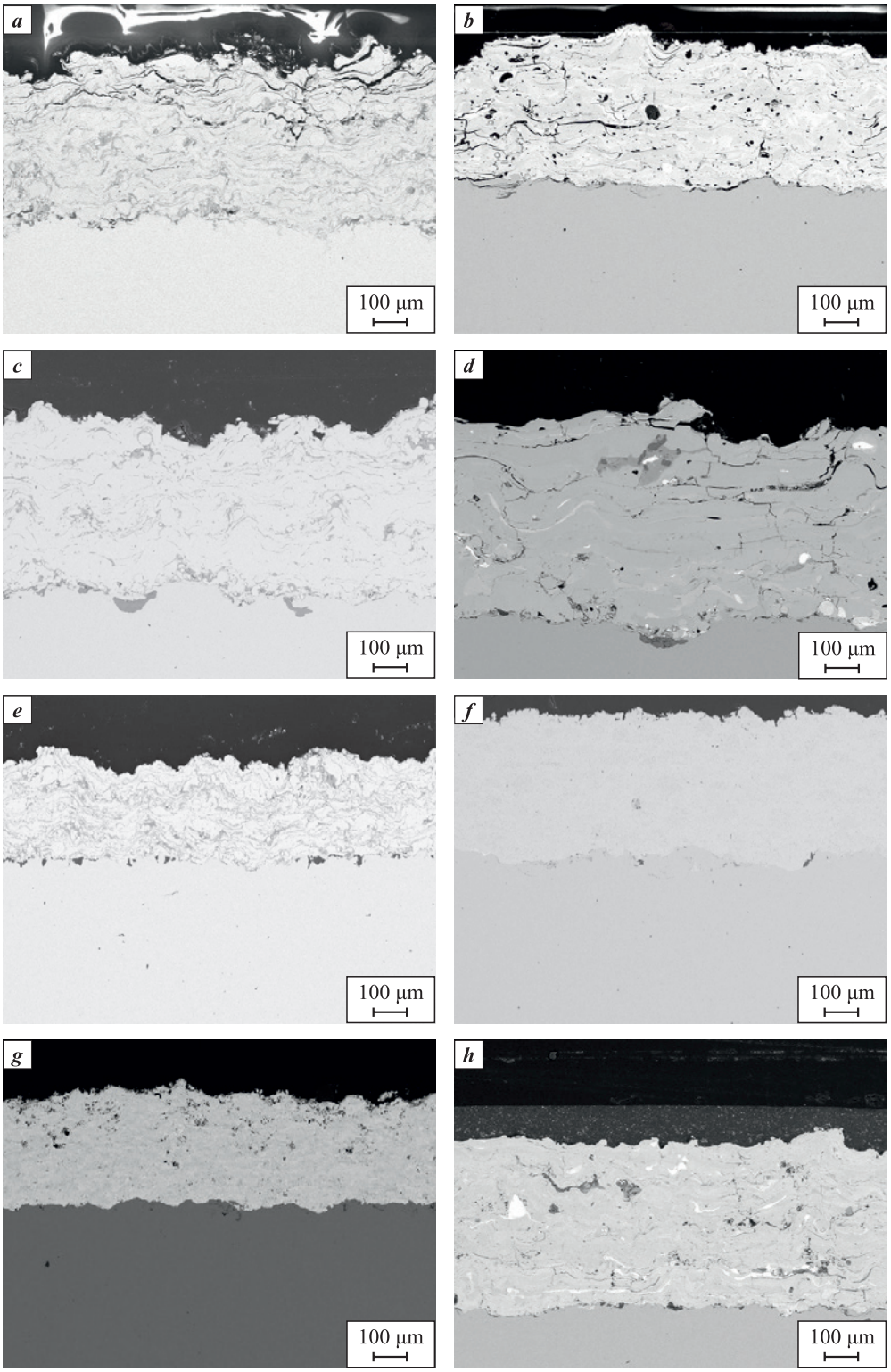

Fig. 12. Microstructure of the coating

a – EDM, iron-based wire; ***b*** – EDM, nickel-based wire; ***c*** – EDM in an argon environment, iron-based wire; ***d*** – EDM in an argon environment, nickel-based wire; ***e*** – ADM, iron-based wire; ***f*** – VSGPN, self-fluxing nickel-based powder; ***g*** – VSGPN, tungsten carbide powder in a cobalt matrix; ***h*** – EDM, nickel-based wire impregnated with epoxy-novolac resin

Рис. 12. Микроструктуры различных покрытий

a – ЭДМ, проволока на основе железа; ***b*** – ЭДМ, проволока на основе никеля; ***c*** – ЭДМ в среде аргона, проволока на основе железа; ***d*** – ЭДМ в среде аргона, проволока на основе никеля; ***e*** – АДМ, проволока на основе железа; ***f*** – ВСГПН, самофлюсующийся порошок на основе никеля; ***g*** – ВСГПН, порошок на основе карбида вольфрама в кобальтовой матрице; ***h*** – ЭДМ, проволока на основе никеля с пропиткой на основе эпоксиновolачной смолы

To increase the spraying flame temperature and achieve greater particle melting, activated arc spraying (AAS) was employed in a propane-air environment [69]. The use of AAS with iron-based wires improved the physical and mechanical properties of the coating (Fig. 12, *e*). However, due to the combustion of the propane-air mixture during application, the metallization layer still contained oxide layers that were not resistant to aggressive environments, making AAS coatings unsuitable in their pure form. The application of an epoxy novolac resin-based impregnation helped to limit the access of corrosive media to the metallization layer, thus preventing its destruction. However, in areas with artificially introduced defects such as "scratches", the metallization layer deteriorated, and corrosion products were observed on the substrate.

Using high-velocity oxy-fuel (HVOF) spraying, self-fluxing powder materials based on nickel (Fig. 12, *f*) and tungsten carbide in a cobalt matrix (Fig. 12, *g*) were applied with a thickness of 300–350 μm. These coatings demonstrated high physical and mechanical properties and sufficient resistance to corrosive environments. The HVOF-applied layer exhibited higher density with fewer oxide films between particles, which was achieved due to the higher particle velocity and shorter exposure time to the gas-oxidizing environment compared to EAS. The use of tungsten carbide-based powder materials provided coatings with excellent hardness and wear resistance; however, high porosity allowed aggressive media to penetrate and lead to substrate degradation.

Based on the results of the conducted studies, the following conditions were found to provide satisfactory outcomes:

– a nickel-based metallization layer containing ~18 % chromium and ~13 % molybdenum, applied using EAS, followed by impregnation with an epoxy novolac resin composition with a thickness of 70–150 μm;

– a nickel-based self-fluxing powder metallization layer containing ~16 % chromium, applied using HVOF spraying.

It is noteworthy that with comparable properties, the cost of the HVOF-applied coating is lower than that of EAS.

Conclusion

The introduction of anti-corrosion coatings for protecting submersible equipment used in oil production, particularly the inner surface of tubing, began in the late 1990s with the adoption of polymer coatings. The extension of service life was accompanied by advancements in coating formulations, transitioning from Bisphenol A-based epoxy resins to epoxy novolac resins, as well as improvements in application methods. These developments led to the introduction of thermal curing at temperatures of 170–200 °C. A significant milestone in this evolution was the development of two-layer systems that combined high barrier properties with resistance to ARPD and inorganic salt deposition. Currently, manufacturers of protective coatings face the challenge of developing multifunctional single-layer coatings that combine these protective capabilities.

At the same time, continuous improvements have been made to the composition and structure of metallization coatings. Traditional coatings applied using EAS with iron-based wires – characterized by overall porosity levels of up to 10 % and the presence of oxide films along particle boundaries – failed to provide adequate barrier protection. This resulted in the formation of corrosion products at the metal–coating interface, leading to rapid deterioration. Two parallel approaches have been pursued to enhance the operational reliability of such coatings: developing high-temperature polymer impregnations to seal porosity in the upper layers, and adopting HVOF spraying technology, which enables the production of non-porous, high-alloy corrosion-resistant coatings. While the scientific basis for these methods has been established, their full-scale implementation at production facilities is still required, along with efforts to replace imported components with domestically produced alternatives.

References / Список литературы

1. Banerjee S. Developments and challenges of mature oil fields. *The Way Ahead*. 2013;9(3):11–13. https://doi.org/10.2118/0313-011-TWA
2. Abdel-Basset M., Al-Mufarej M., Al-Mutawa M., Chetri H., Anthony E., Al-Zaabi H., Bolanos N., Ruiz H., Harami K. Integrated production optimization workflow provides robust platform for significant oil gain to a mature oilfield. In: *Abu Dhabi International Petroleum Exhibition and Conference* (Abu–Dhabi, UAE, 12–15 November 2018). 2018:D022S150R001. https://doi.org/10.2118/193121-MS
3. Stetsyuk I.A. Analysis of the effectiveness of various protection methods for CHO wells of the complicated fund of LLC "RN-Purneftegaz". *Oilfield Engineering*. 2017;(8):40–43. (In Russ.).
   Стецюк И.А. Анализ эффективности применения различных методов защиты ГНО скважин осложненного фонда ООО «РН-Пурнефтегаз». *Инженерная практика*. 2017;(8):40–43.
4. Agafonov A.A., Nasedkin I.G., Novikova N.V., Buldakova N.S. Evaluation of the efficiency of using a magnetic

inductor for combat cutting with ARPD on the production fund of PJSC "Udmurtneft". *Oilfield Engineering*. 2020;(1):20–24. (In Russ.).

Агафонов А.А., Наседкин И.Г., Новикова Н.В., Булдакова Н.С. Оценка эффективности применения магнитного индуктора для борьбы с АСПО на добывающем фонде ОАО «Удмуртнефть». *Инженерная практика*. 2020;(1):20–24.

5. Mitroshin A.V., Dubovtsev A.S., Dulesova L.G. Analysis of complicating factors during mechanized oil production at PJSC "LUKOIL" enterprises. *Geology, geophysics and development of oil and gas fields*. 2019;(6):57–60. (In Russ.). https://doi.org/10.30713/2413-5011-2019-6(330)-57-60

Митрошин А.В., Дубовцев А.С., Дулесова Л.Г. Анализ осложняющих факторов в процессе механизированной добычи нефти на предприятиях ПАО «ЛУКОЙЛ». *Геология, геофизика и разработка нефтяных и газовых месторождений*. 2019;(6):57–60. https://doi.org/10.30713/2413-5011-2019-6(330)-57-60

6. Fajobi M.A., Loto R.T., Oluwole O.O. Corrosion in crude distillation overhead system: A review. *Journal of Bio- and Tribo-Corrosion*. 2019;5:67. https://doi.org/10.1007/s40735-019-0262-4
7. El-Meligi A.A. Corrosion preventive strategies as a crucial need for decreasing environmental pollution and saving economics. *Recent Patents on Corrosion Science*. 2010;2:22–33. https://doi.org/10.2174/1877610801002010022
8. Fayomi O.S.I., Akande I.G., Odigie S. Economic impact of corrosion in oil sectors and prevention: An overview. *Journal of Physics: Conference Series*. 2019;1378(2):022037. https://doi.org/10.1088/1742-6596/1378/2/022037
9. Hou B., Li X., Ma X., Du C., Zhang D., Zheng M., Xu W., Lu D., Ma F. The cost of corrosion in China. *npj Materials Degradation*. 2017;1:4. https://doi.org/10.1038/s41529-017-0005-2
10. Misra S., Baruah S., Singh K. Paraffin problems in crude oil production and transportation: A review. *SPE Production & Operations*. 1995;10(1):50–54. https://doi.org/10.2118/28181-PA
11. Kumar A. Perspectives of flow assurance problems in oil and gas production: A mini-review. *Energy & Fuels*. 2023;37(12):8142–8159. https://doi.org/10.1021/acs.energyfuels.3c00843
12. Sousa A.M., Ribeiro T.P., Pereira M.J., Matos H.A. Review of the economic and environmental impacts of producing waxy crude oils. *Energies*. 2023;16(1):120. https://doi.org/10.3390/en16010120
13. Gorodilova K.E. Silicate-enamel coating – an effective method of protecting pipelines from corrosion and asphalt-resin-paraffin deposits. *Oilfield Engineering*. 2020;(5-6):66–69. (In Russ.).

Городилова К.Е. Силикатно-эмалевое покрытие – эффективный способ защиты трубопроводов от коррозии и асфальто-смоло-парафиновых отложений. *Инженерная практика*. 2020;(5-6):66–69.

14. Markin A.N., Nizamov R.E., Sukhoverkhov S.V. Oilfield chemistry: A practical guide. Vladivostok: Dalnauka, 2011. 288 p. (In Russ.).

Маркин А.Н., Низамов Р.Э., Суховерхов С.В. Нефтепромысловая химия: Практ. рук-во. Владивосток: Дальнаука, 2011. 288 с.

15. Latypov O.R. Operation of oil and gas equipment in aggressive environments. Ufa: Ufa State Petroleum Technological University, 2018. 151 p. (In Russ.).

Латыпов О.Р. Эксплуатация нефтегазового оборудования в агрессивных средах. Уфа: УГНТУ, 2018. 151 с.

16. Sousa A.L., Matos H.A., Guerreiro L.P. Preventing and removing wax deposition inside vertical wells: A review. *Journal of Petroleum Exploration and Production Technology*. 2019;9:2091–2107. https://doi.org/10.1007/s13202-019-0609-x
17. Yudin P.E., Petrov S.S., Maksimuk A.V., Knyazeva Zh.V., Prokudin A.V. Features of operation of pump and compressor pipes in conditions of wells of the corrosion fund. *Korroziya. Territorii Neftegaz*. 2018;40(2):50–54. (In Russ.).

Юдин П.Е., Петров С.С., Максимук А.В., Князева Ж.В., Прокудин А.В. Особенности эксплуатации насосно-компрессорных труб в условиях скважин коррозионного фонда. *Коррозия. Территории Нефтегаз*. 2018;40(2):50–54.

18. Craig B.D. Evaluation and application of highly alloyed materials for corrosive oil production. *Journal of Materials for Energy Systems*. 1983;5(1):53–58.
19. Lasebikan B.A., Akisanya A.R., Deans W.F. The mechanical behavior of a 25Cr Super duplex stainless steel at elevated temperature. *Journal of Materials Engineering and Performance*. 2013;22:598–606.
20. Hahn B., Konrad J., Schneider A., Stallybrass C. Steel alloy for ferritic steel having excellent creep strength and oxidation resistance at elevated usage temperatures: Patent 9080230B2 (US). 2015. https://patents.google.com/patent/US9080230B2/en
21. Urech B.A., Stewart T., Fullerton P. System and method for producing bimetallic line pipe: Patent 2005/0251987A1 (US). 2005. https://patents.google.com/patent/US20050251987
22. Shugol A.A. Test results of austenitic steel liner as a corrosion protection system for tubing and line pipes. *Territoriya Neftegaz*. 2021;(11-12):22–27. https://elibrary.ru/rnwvne

Шуголь А.А. Результаты испытаний лейнера из аустенитной стали как защитной системы от коррозии для насосно-компрессорных и линейных труб. *Территория Нефтегаз*. 2021;(11-12):22–27. https://elibrary.ru/rnwvne

23. Pavlov D.G., Kaunov A.S. Protective system for tubing DCS inoxinside. In: *Actual problems of scientific knowledge. New technologies of the fuel and energy complex 2022*: Materials of the VI International Scientific and Practical Conference (Tyumen, 22 April 2022). Ed. S.N. Nagaeva. Tyumen: Tyumen Industrial University, 2022. P. 134–138. (In Russ.). https://elibrary.ru/dlwikg

Павлов Д.Г., Каунов А.С. Защитная система для НКТ DCS inoxinside. В сб.: *Актуальные проблемы научного знания. Новые технологии ТЭК-2022*: Материалы VI Междунар. науч.-практич. конференции (Тюмень, 22 апреля 2022 г.). Отв. ред. С.Н. Нагаева. Тюмень: ТИОИУ, 2022. С. 134–138. https://elibrary.ru/dlwikg

24. Bogatov N.A., Bogatov A.A., Salikhyanov D.R. Lined corrosion-resistant tubing. *Steel*. 2014;(11):86–88. (In Russ.). https://elibrary.ru/uinruv

Богатов Н.А., Богатов А.А., Салихянов Д.Р. Лейнированные коррозионностойкие насосно-компрессорные трубы. *Сталь*. 2014;(11):86–88. https://elibrary.ru/uinruv

25. McMillan J.S. Method of lining tubular members including rolling and crushing a liner: Patent 4923663 (US). 1990.

26. Krips H., Podhorsky M. Hydraulisches Aufweiten — ein neus Verfahren zur Befestigungen fur Rohren. *VGB Kraftwerkstechnik*. 1976;56(7):456–464. (In Germ.).

27. Vakili M., Koutník P., Kohout J. Addressing hydrogen sulfide corrosion in oil and gas industries: A sustainable perspective. *Sustainability*. 2024;16(4):1661. https://doi.org/10.3390/su16041661

28. Liu Z.Y., Wang X.Z., Liu R.K., Du C.W., Li X.G. Electrochemical and sulfide stress corrosion cracking behaviors of tubing steels in a H_2S/CO_2 annular environment. *Journal of Materials Engineering and Performance*. 2014;23:1279–1287. https://doi.org/10.1007/s11665-013-0855-x

29. Kim S.K. Results of operational tests of oilfield pipelines and tubing made of steels with increased corrosion resistance at the fields of Lukoil-Komi. *Oilfield Engineering*. 2011;(11):44–52. (In Russ.).

Ким С.К. Результаты ОПИ нефтепроводных труб и НКТ из сталей с повышенной коррозионной стойкостью на месторождениях ООО «ЛУКОЙЛ-Коми». *Инженерная практика*. 2011;(11):44–52.

30. Cao J., Ma W., Huang W., Su Z., Zhu Y., Wang J. A novel inner wall coating-insulated oil pipeline for scale and wax prevention. *Processes*. 2023;11(7):1964. https://doi.org/10.3390/pr11071964

31. McKeen L.W., Hofmans J., Nelissen J. Engineered internal downhole coating solutions for corrosion & deposition control in downhole production tubulars. In: *Abu Dhabi International Petroleum Exhibition and Conference* (Abu Dhabi, UAE, 11–14 November 2012). 2012, P. SPE-161204-MS. https://doi.org/10.2118/161204-MS

32. Protasov V.N. Theory and practice of using polymer coatings in equipment and structures of the oil and gas industry. Moscow: Nedra, 2007. 375 p. (In Russ.).

Протасов В.Н. Теория и практика применения полимерных покрытий в оборудовании и сооружениях нефтегазовой отрасли. М.: Недра, 2007. 375 с.

33. Lauer R.S. The use of high performance polymeric coatings to mitigate corrosion and deposit formation in pipeline applications. In: *NACE Corrosion*. 2007. P. NACE-07028.

34. Zeng Q., Kang L., Fan J., Song L., Wan S., Liao B., Guo X. Durable superhydrophobic silica/epoxy resin coating for the enhanced corrosion protection of steel substrates in high salt and H_2S environments. *Colloids and Surfaces A: Physicochemical and Engineering Aspects*. 2022;654:130137. https://doi.org/10.1016/j.colsurfa.2022.130137

35. Sorensen P.A., Kiil S., Dam-Johansen K., Weinell C.E. Anticorrosive coatings: A review. *Journal of Coatings Technology Research*. 2009;6(2):135–176. https://doi.org/10.1007/s11998-008-9144-2

36. Gabdrafikov R.R. Increasing the inter-repair period of production wells using tubing with protective coatings in the fields of the Komi Republic. In: *Lomonosov scientific readings of students, postgraduates, and young scientists-2022* (Arkhangelsk, 1–30 April 2012). Arkhangelsk: Northern (Arctic) Federal University n.a. M.V. Lomonosov, 2022. P. 97–99. (In Russ.). https://elibrary.ru/ekhvbs

Габдрафиков Р.Р. Повышение межремонтного периода работы добывающих скважин при использовании насосно-компрессорных труб с защитным покрытием на месторождениях Республики Коми. В сб.: *Ломоносовские научные чтения студентов, аспирантов и молодых ученых-2022* (Архангельск, 1–30 апреля 2012 г.). Архангельск: Северный (Арктический) федеральный университет им. М.В. Ломоносова, 2022. С. 97–99. https://elibrary.ru/ekhvbs

37. Askari M. Downhole corrosion inhibitors for oil and gas production–a review. *Applied Surface Science Advances*. 2021;6:100128. https://doi.org/10.1016/j.apsadv.2021.100128

38. Eds. I. Inamuddin, R. Boddula, M.I. Ahamed, A.M. Asiri. Polymers coatings: technology and applications. John Wiley & Sons, 2020. 480 p.

39. Proskurkin E.V., Gelovani V.A., Sonk A.N., Petrov I.V., Yarema I.P., Sukhomlin D.A. Zinc coatings as modern systems for pipe corrosion protection. *Steel*. 2018;(6): 32–37. (In Russ.).

Проскуркин Е.В., Геловани В.А., Сонк А.Н., Петров И.В., Ярема И.П., Сухомлин Д.А. Цинковые покрытия – основные современные системы защиты труб от коррозии. *Сталь*. 2018;(6):32–37.

40. Aleksandrov E.V., Yudin P.E., Knyazeva Zh.V. New method of autoclave test for express analysis of anticorrosive coatings. *Pipeline transport: Theory and practice*. 2015;49(3):3–11. (In Russ.).

Александров Е.В., Юдин П.Е., Князева Ж.В. Новая методика автоклавного теста для экспресс-анализа антикоррозионных покрытий. *Трубопроводный транспорт: Теория и практика*. 2015;49(3):3–11.

41. Yudin P.E., Knyazeva Zh.V. Evaluation of the barrier properties of internal anti-corrosive coatings of oil pipelines and pump-compressor pipes using an autoclave test. *Pipeline transport: Theory and practice*. 2016;53(1):3–8. (In Russ.).

Юдин П.Е., Князева Ж.В. Оценка барьерных свойств внутренних антикоррозионных покрытий нефтепроводных и насосно-компрессорных труб с помощью автоклавного теста. *Трубопроводный транспорт: Теория и практика*. 2016;53(1):3–8.

42. Bai J., Jin X., Wu J.T. Multifunctional anti-wax coatings for paraffin control in oil pipelines. *Petroleum Science*.

2019;16(3):619–631.
https://doi.org/10.1007/s12182-019-0309-7

43. Liu S., Wang C., Liu S., Li K., Luo H., Fan W., Wang H. pH-responsive smart composite coating with active anti-corrosion and efficient scale inhibition properties. *Progress in Organic Coatings*. 2022;170:106973.
https://doi.org/10.1016/j.porgcoat.2022.106973

44. Liang B., Sun Y., Bai Z., Li H., Shi Y., Lin D., Wang H. A novel UV-curable amphiphobic coating with dynamic air-layer copolymer brush offering stable dual-functional anti-scaling and anti-corrosion properties. *Progress in Organic Coatings*. 2024;194:108607.
https://doi.org/10.1016/j.porgcoat.2023.107700

45. Guo Y., Wang J., Su X., Tang C., Wang J. Anti-scaling and anti-corrosive study on waterborne composite coatings based on siloxane-g-polybutadiene incorporated with PTFE and nano-SiO_2-EDTA. *Journal of Coatings Technology and Research*. 2024;(November):1–9.
https://doi.org/10.1007/s11998-024-01011-5

46. Baranov N.A., Yudin P.E., Maksimuk A.V., Taratorin A.N., Zheldak M.V., Knyazeva Zh.V., Petrov S.S. Microwave installation for modifying polymer coatings of internal pipe surfaces: Patent 2710776 C1 (RF). 2020. (In Russ.).
https://elibrary.ru/murfbl

Баранов Н.А., Юдин П.Е., Максимук А.В., Таратори́н А.Н., Желдак М.В., Князева Ж.В., Петров С.С. СВЧ-установка для модификации полимерных покрытий внутренних поверхностей труб: Патент 2710776 C1 (РФ). 2020. https://elibrary.ru/murfbl

47. Baranov N.A., Zheldak M.V., Makarov E.A., Yudin P.E., Maksimuk A.V., Petrov S.S., Trofimov I.S., Bogatov M.V. Laboratory research circulation stand for testing methods of counteracting sedimentation and corrosion processes in a tubing column: Patent 202556 (RF). 2021. (In Russ.).

Баранов Н.А., Желдак М.В., Макаров Е.А., Юдин П.Е., Максимук А.В., Петров С.С., Трофимов И.С., Богатов М.В. Лабораторно-исследовательский циркуляционный стенд для испытаний методов противодействия процессам седиментации и коррозии в колонне насосно-компрессорных труб: Патент 202556 (РФ). 2021.

48. Maksimuk A.V., Yudin P.E., Verevkin A.G., Zheldak M.V., Bogatov M.V., Berkov D.V., Krysina D.A., Vyazgin D.S., Ivanov A.V. Laboratory testing stand for simulating operating conditions inside a tubing column submerged in an oil well during testing of various methods of counteracting corrosion and sedimentation: Patent RU2802764C1 (RF). 2023. (In Russ.).

Максимук А.В., Юдин П.Е., Веревкин А.Г., Желдак М.В., Богатов М.В., Берков Д.В., Крысина Д.А., Вязгин Д.С., Иванов А.В. Лабораторный испытательный стенд для воспроизведения эксплуатационных условий внутри погруженной в нефтяную скважину колонны насосно-компрессорных труб при испытаниях различных методов противодействия коррозии и седиментации: Патент RU2802764C1 (РФ). 2023.

49. Bogatov M.V., Yudin P.E., Verevkin A.G., Berkov D.V. Influence of hydrophilicity and oleophobicity on asphalt-resin-paraffin deposits formation. *Petroleum Engineering*. 2022;20(6):114–123. (In Russ.).
https://doi.org/10.17122/ngdelo-2022-6-114-123

Богатов М.В., Юдин П.Е., Веревкин А.Г., Берков Д.В. Влияние гидрофильности, олеофобности на образование асфальтосмолопарафиновых отложений. *Нефтегазовое дело*. 2022;20(6):114–123.
https://doi.org/10.17122/ngdelo-2022-6-114-123

50. Berkov D.V., Kostyuk I.I., Yudin P.E., Verevkin A.G. Development of a stand for evaluating the resistance of internal protective coatings of tubing to inorganic scaling. *Petroleum Engineering*. 2024;22(1):160–172. (In Russ.).
https://doi.org/10.17122/ngdelo-2024-1-160-172

Берков Д.В., Костюк И.И., Юдин П.Е., Веревкин А.Г. Разработка стенда оценки стойкости внутренних защитных покрытий НКТ к неорганическим солеотложениям. *Нефтегазовое дело*. 2024;22(1):160–172.
https://doi.org/10.17122/ngdelo-2024-1-160-172

51. Berkov D.V., Kostyuk I.I., Yudin P.E., Verevkin A.G. Possibility assessment for using protective coatings and polymer materials on tubing to prevent inorganic scaling on the inner surface of pipes. *International Review of Applied Sciences and Engineering*. 2024.
https://doi.org/10.1556/1848.2024.00819

52. Berkov D.V., Yudin P.E., Verevkin A.G. Investigation of the effect of roughness of internal protective coatings of tubing on their ability to prevent gypsum scaling. In: *Modern prospects for the development of science, technology, and technologies*: Collection of scientific articles of the 2nd International scientific and technical conference (Voronezh, 11 October 2024). Kursk: CJSC "University Book", 2024. P. 64–76. (In Russ.).
https://doi.org/10.47581/2024.TM-07/Berkov-Denis-01

Берков Д.В., Юдин П.Е., Веревкин А.Г. Исследование влияния шероховатости внутренних защитных покрытий насосно-компрессорных труб на их способность предотвращать образование гипсовых солеотложений. В сб.: *Современное перспективное развитие науки, техники и технологий*: Сб. науч. статей 2-й Междунар. науч.-технич. конференции (Воронеж, 11 октября 2024 г.). Курск: ЗАО «Университетская книга», 2024. С. 64–76.
https://doi.org/10.47581/2024.TM-07/Berkov-Denis-01

53. Heydrich M., Hammami A., Choudhary S., Mockel M., Ratulowski J. Impact of a novel coating on inorganic scale deposit growth and adhesion. In: *Offshore Technology Conference* (Houston, Texas, May 2019). 2019. P. OTC-29218-MS.
https://doi.org/10.4043/29218-MS

54. Berkov D.V., Kostyuk I.I., Yudin P.E., Verevkin A.G. Application of protective coatings and scale inhibitors for tubing to prevent scaling. *Petroleum Engineering*. 2024;22(5):113–126. (In Russ.).
https://doi.org/10.17122/ngdelo-2024-5-113-126

Берков Д.В., Костюк И.И., Юдин П.Е., Веревкин А.Г. Применение защитных покрытий НКТ и ингибиторов солеотложения для предотвращения образования солеотложений. *Нефтегазовое дело*. 2024;22(5):113–126.
https://doi.org/10.17122/ngdelo-2024-5-113-126

55. Jabbarov Sh.N. Corrosion susceptibility of underground oil and gas production equipment. In: *Exact science*: Collection of articles of the XVIII International scientific con-

ference “Technocongress” (17 December 2017). Kemerovo: Publ. “Pluton”, 2017. P. 3–7. (In Russ.).

Джаббаров Ш.Н. Подверженность коррозии подземного оборудования по добыче нефти и газа. В сб.: *Точная наука*: Статьи XVIII Междунар. науч. конференции «Техноконгресс» (17 декабря 2017 г.). Кемерово: Изд. дом «Плутон», 2017. С. 3–7.

56. Romanov V.S., Goldshtein V.G., Vasilyeva N.S. Statistical analysis of technological violations in the operation of submersible electric motors. *Transactions of the Kola Science Center of the Russian Academy of Sciences*. 2018; 3-16(9):114–121. (In Russ.).

Романов В.С., Гольдштейн В.Г., Васильева Н.С. Статистический анализ технологических нарушений в эксплуатации погружных электродвигателей. *Труды Кольского научного центра РАН*. 2018;3-16(9):114–121.

57. Knyazeva Zh.V., Andriyanov D.I., Yudin P.E., Vasin R.A. Study of the mechanism of carbon dioxide corrosion of thermal spray metallization coatings used to protect submersible electric motors. *Petroleum Engineering*. 2023;21(5);168–181. (In Russ.).
https://doi.org/10.17122/ngdelo-2023-5-168-181

Князева Ж.В., Андриянов Д.И., Юдин П.Е., Васин Р.А. Исследование механизма углекислотной коррозии газотермических металлизационных покрытий, применяемых для защиты ПЭД. *Нефтегазовое дело.* 2023;21(5);168–181.
https://doi.org/10.17122/ngdelo-2023-5-168-181

58. Łatka L., Pawłowski L., Winnicki M., Sokołowski P., Małachowska A., Kozerski S. Review of functionally graded thermal sprayed coatings. *Applied Sciences*. 2020;10(15):5153.
https://doi.org/10.3390/app10155153

59. Kumar P.A., Khurana V. A review – study of thermal spray coatings for corrosive wear. *International Journal of Advance Research, Ideas and Innovations in Technology*. 2016;2(3):1–6.

60. Nguyen V.T., Thu Q.L., Nguyen T.A., Ly Q.C., Thi L.P., Thi H.P., Mai T.D.T. Arc thermal spray NiCr20 alloy coating: fabrication, sealant, heat treatment, wear, and corrosion resistances. *International Journal of Electrochemistry*. 2019;2019(1):8796958.
https://doi.org/10.1155/2019/8796958

61. Knyazeva Zh.V., Yudin P.E., Amosov A.P., Petrov S.S., Maksimuk A.V. Classification of causes of destruction of metallization coating of submersible electric motors during operation. *Science intensive technologies in mechanical engineering*. 2019;9(99):25–32. (In Russ.).
https://doi.org/10.30987/article_5d2df0884cc457.62830322

Князева Ж.В., Юдин П.Е., Амосов А.П., Петров С.С., Максимук А.В. Классификация причин разрушения металлизационного покрытия погружных электродвигателей при эксплуатации. *Наукоемкие технологии в машиностроении*. 2019;9(99):25–32.
https://doi.org/10.30987/article_5d2df0884cc457.62830322

62. Knyazeva Zh.V., Andriyanov D.I., Yudin P.E., Vasin R.A. Studies of wear resistance and mechanism of abrasive wear of thermal spray coatings used to protect submersible electric motors. *Petroleum Engineering*. 2023;21(1): 90–102. (In Russ.).
https://doi.org/10.17122/ngdelo-2023-1-90-102

Князева Ж.В., Андриянов Д.И., Юдин П.Е., Васин Р.А. Исследования износостойкости и механизма абразивного износа газотермических металлизационных покрытий, используемых для защиты ПЭД. *Нефтегазовое дело*. 2023;21(1):90–102.
https://doi.org/10.17122/ngdelo-2023-1-90-102

63. Dorofeeva A.G. Identification of causes of destruction of housings of submersible electric motors. In: *New technologies – for the oil and gas region*: Materials of the International scientific and practical conference (Tyumen, 16–20 May 2016). Tyumen: Tyumen Industrial University, 2016. P. 207–210. (In Russ.).

Дорофеева А.Г. Выявление причин разрушения корпусов погружных электродвигателей. В сб.: *Новые технологии – нефтегазовому региону*: Материалы Междунар. науч.-практич. конференции (Тюмень, 16–20 мая 2016 г.). Тюмень: Тюменский индустриальный университет, 2016. С. 207–210.

64. Knyazeva Zh.V., Yudin P.E. Autoclave tests of metallization coatings. In: *Prospective development of science, engineering and technology*: Collection of scientific articles of the 10th International scientific and practical conference (Kursk, 30 October 2020). Kursk: South-West State University, 2020. P. 74–78. (In Russ.).
https://doi.org/10.47581/2020/30.10.2020/MTO53/1/018

Князева Ж.В., Юдин П.Е. Автоклавные испытания металлизационных покрытий. В сб.: *Перспективное развитие науки, техники и технологий*: Научные статьи 10-й Междунар. науч.-практич. конференции (Курск, 30 октября 2020 г.). Курск: Юго-Западный государственный университет, 2020. С. 74–78.
https://doi.org/10.47581/2020/30.10.2020/MTO53/1/018

65. Yudin P.E., Zheldak M.V., Petrov S.S., Aleksandrov E.V., Manakhov A.M. Laboratory autoclave: Patent 130878 (RF). 2013. (In Russ.).

Юдин П.Е., Желдак М.В., Петров С.С., Александров Е.В., Манахов А.М. Лабораторный автоклав: Патент 130878 (РФ). 2013.

66. Andriyanov D.I., Yudin P.E., Knyazeva Zh.V., Pozdeeva A.Yu., Amosov A.P. Influence of the spraying gas environment on the properties of thermal spray coatings. *Petroleum Engineering*. 2024;22(4):115–125. (In Russ.).
https://doi.org/10.17122/ngdelo-2024-4-115-125

Андриянов Д.И., Юдин П.Е., Князева Ж.В., Поздеева А.Ю., Амосов А.П. Влияние газовой среды напыления на свойства газотермических металлизационных покрытий. *Нефтегазовое дело*. 2024;22(4):115–125.
https://doi.org/10.17122/ngdelo-2024-4-115-125

67. Pozdeeva A.Yu., Amosov A.P., Yudin P.E. Materials for impregnation of porous metallized gas-thermal anticorrosive coatings of submersible oilfield equipment. Part 1. *Petroleum Engineering*. 2024;22(2):156–164. (In Russ.).
https://doi.org/10.17122/ngdelo-2024-2-156-164

Поздеева А.Ю., Амосов А.П., Юдин П.Е. Материалы для пропитки пористых металлизационных газотермических антикоррозионных покрытий погружного нефтепромыслового оборудования. Часть 1. *Нефтегазовое дело*. 2024;22(2):156–164.
https://doi.org/10.17122/ngdelo-2024-2-156-164

68. Pozdeeva A.Yu., Amosov A.P., Yudin P.E. Materials for impregnation of porous metallized gas-thermal anticorrosive coatings of submersible oilfield equipment. Part 2. *Petroleum Engineering*. 2024;22(3):113–122. (In Russ.).
https://doi.org/10.17122/ngdelo-2024-3-113-122

Поздеева А.Ю., Амосов А.П., Юдин П.Е. Материалы для пропитки пористых металлизационных газотермических антикоррозионных покрытий погружного нефтепромыслового оборудования. Часть 2. *Нефтегазовое дело*. 2024;22(3):113–122.
https://doi.org/10.17122/ngdelo-2024-3-113-122

69. Korobov Yu.S. Analysis of the properties of gas-thermal coatings. Ekaterinburg: Publ. Ural University, 2016. 92 p. (In Russ.).

Коробов Ю.С. Анализ свойств газотермических покрытий: Учеб. пос. в 2 ч. Екатеринбург: Изд-во Уральского университета, 2016. 92 с.

Information about the Author

Pavel E. Yudin – Cand. Sci. (Eng.), Associate Professor of the Department of metal science, powder metallurgy, nanomaterials of Samara State Technical University; Director of Science of Samara Scientific and Production Center, LLC
ORCID: 0000-0002-4517-3744
E-mail: yudin@npcsamara.ru

Сведения об авторе

Павел Евгеньевич Юдин – к.т.н., доцент кафедры «Металловедение, порошковая металлургия, наноматериалы» Самарского государственного технического университета; директор по науке ООО «НПЦ «Самара»
ORCID: 0000-0002-4517-3744
E-mail: yudin@npcsamara.ru

Received 25.12.2024
Revised 09.01.2025
Accepted 09.01.2025

Статья поступила 25.12.2024 г.
Доработана 09.01.2025 г.
Принята к публикации 09.01.2025 г.

Зарегистрирован Федеральной службой по надзору
в сфере связи, информационных технологий
и массовых коммуникаций.
Свидетельство о регистрации ПИ № ФС77-79230

Журнал распространяется агентством «Урал-Пресс»
Подписной индекс: 80752 (печатная версия)
05108 (электронная версия)